Ultra-slow dynamics of localised modes in the Discrete Nonlinear Schrödinger Equation

Liviu Florin Chirondojan

Computational Nonlinear and Quantum Optics Group

Department of Physics

University of Strathclyde, Glasgow

A thesis presented for the degree of

Doctor of Philosophy

May 28, 2019

Declaration of Authenticity and Author's Rights

This thesis is the result of the author's original research. It has been composed by the author and has not been previously submitted for examination which has led to the award of a degree.

Signed: Liviu Florin Chirondojan

Date: May 28, 2019

Contents

Declaration of Authenticity and Author's Rights i

Acknowledgements iv

Abstract 1

List of Publications 2

Foreword 3

1 Introduction **6**

1.1 From the Gross-Pitaevskii equation to the DNLSE 9

1.2 Discrete Breathers in the DNLSE 17

1.3 The structure of the thesis 32

2 Numerical Methods and Numerical Simulations of the DNLSE **36**

2.1 Presentation of Numerical Methods 36

2.1.1 State Initialisation 36

2.1.2 Langevin Heat Baths. Grand-Canonical Set-ups 39

2.1.3 Numerical Evaluation of Thermal Parameters 44

2.1.4 Calibration of states with phase diagrams in literature 48

2.1.5 State saving/loading 49

2.2 Numerical Simulations of Breather Dynamics 53

2.2.1 Lack of Breather Tails in Large Backgrounds 53

2.2.2 Breather life-times in large backgrounds 57

2.3 Numerical Low-Pass Filters 62

2.3.1 Building a Low-Pass Filter 62
2.3.2 Behaviour of Slow/Fast Quantities 64

3 Review of Extreme Events in the DNLSE 69

3.1 Analytical Investigation of Dimer Systems 69
3.2 Partial Averaging near Resonance 75
3.3 Numerical Investigation - Phase Scanning in the case of Catastrophic Collisions 80
3.4 Numerical Investigation - Amplitude Scanning in the case of Catastrophic Collisions 84

4 Multiple Time Scale Analysis of Pinned Breathers 87

4.1 Separation of Time Scales - Outline of the general procedure 89
4.1.1 Asymptotic Expansions 89
4.1.2 Decoupling due to the separation of time scales 96
4.2 First Non-Trivial Terms in The Perturbative Calculation 98
4.3 Higher Order Terms in the Perturbative Calculation 102
4.4 Derivative at order $\mathcal{O}(\varepsilon^2)$ 106
4.5 Fluxes for the Hamiltonian and the Norm at order $\mathcal{O}(\varepsilon)$ for a Bose Hubbard Chain 109
4.6 Fluxes for the Hamiltonian and the Norm at order $\mathcal{O}(\varepsilon)$ for a dimer containing a breather 111
4.7 Solvability Conditions 113
4.8 Breather fluctuations and comparison with simulations 115
4.8.1 Size of fluctuations 115
4.8.2 Stability of the trimer configuration 119
4.9 A less fluctuating quantity. Defining a slow norm 122
4.10 Conclusions 123

5 Averaging, Effective Hamiltonians and Adiabatic Invariants 126

5.1 Time averaging of the DNLSE dynamics 126

5.2 The Effective Hamiltonian 135

5.3 Effective Hamiltonian vs. Bose Hubbard Hamiltonian 141

5.4 Diffusion of the breather norm 142

5.5 Adiabatic Invariants and strong interactions with the background 150

6 Heterogeneous Multiple Time Scale Methods - Hybrid Integration Schemes and Multiple Breather Systems 155

6.1 Single Breather systems 155

6.1.1 Building a Hybrid Integration Scheme 155

6.1.2 Results produced by the Hybrid Integration Scheme 159

6.1.3 Conclusions 166

6.2 Multi-Breather Systems 167

6.2.1 Writing a Heterogeneous Multiscale Method Algorithm for Lattices with Multiple Breathers 167

6.2.2 An example of a Strong Interaction with a Large Excitation . . . 170

6.2.3 The Applicability Domain of the Multi-Breather Algorithm . . . 175

6.2.4 Results: Hybrid Integrator for Multi Breather Lattices 176

6.3 Thermodynamics and the DNLSE. Uses of the Hybrid Integration Scheme 178

6.3.1 Thermalisation of the background 178

6.3.2 Thermalisation of the whole system - Breather decay 182

6.3.3 Hybrid Integration for Different Background Temperatures . . . 185

7 Conclusions 190

Bibliography 192

Acknowledgements

I would like to thank my supervisors, Gian-Luca Oppo and Antonio Politi, for making this project possible and for critically reading this thesis.

I would also like to thank my parents and sister for all their help. Last but not least, I would like to thank Suruj and Andrew for all the emotional support.

This project was funded by the Carnegie Trust for the Universities of Scotland.

Abstract

The work presented in this thesis focuses on the ultra-slow dynamics of localised modes (breathers) for the Discrete Nonlinear Schrödinger Equation (DNLSE), and on the mechanisms which trigger their astronomically slow decays.

The thesis starts with a literature review of breathers and the DNLSE, giving information about the theoretical background of the project. It then continues with a description of the numerical methods used throughout the project, and of the general behaviour of the DNLSE under numerical integration.

Discrete breathers in Bose-Einstein Condensates in optical lattices or in arrays of optical wave-guides oscillate with frequencies which are much higher than those present in the spectrum of the background. Hence, the interaction between localized breathers and their surroundings is extremely weak, allowing the development of a multiple-time scale perturbation expansion, which is presented in Chapter 4. This analysis will predict a lower bound of the breather drift times and will explain the topological differences between breathers in dimers, trimers and in spatially extended one-dimensional lattices even in the presence of transport from boundary heat baths. These analytical boundaries hold true for lattices of any length, due to the highly localised nature of breathers.

We later look closer at the exceedingly slow thermalisation occurring in the DNLSE. We provide evidence that the breather norm is an adiabatic invariant, and this freezes the dynamics of a tall breather. Consequently, relaxation proceeds via rare events, where energy is suddenly released towards the background. A more detailed investigation of these events is provided in Chapter 5.

In Chapter 6, a Heterogeneous Multiscale Method is introduced. We take advantage of the fast frequency of the breather oscillation to perform averaging, and to build a numerical integrator which behaves similarly to a predictor-corrector propagator, speeding up the running times by a factor of at least 5.

List of Publications

- "Symmetry Breaking in the discrete nonlinear Schrödinger equation due to localised breathers", L. Chirondojan, A. Politi and G.-L. Oppo, in European Conference on Lasers and Electro-Optics and European Quantum Electronics Conference, Munich, Germany (2017)

- "Long term stability of breathers in arrays of optical wave-guides", L. Chirondojan, A. Politi and G.-L. Oppo, in Photon 18, Conference Organised by the Institute of Physics in Birmingham, UK (2018)

- "Multiple-time-scale analysis for pinned breathers in Bose-Hubbard chains", L. Chirondojan and G.-L. Oppo, Physical Review E **99**, 022212 (2019)

- "Dynamical Freezing of Relaxation to Equilibrium", S. Iubini, L. Chirondojan, G-L Oppo, A. Politi and P. Politi, Physical Review Letters **122**, 084102 (2019)

Foreword

The fascination with the properties and elusive nature of matter originates from the very beginning of human civilisation. An atom is the smallest part of an element that can still keeps the physical properties of that element. Its etymology comes from Ancient Greek: *a-* is a prefix used to negate nouns (now borrowed by multiple modern European languages), and *temnein* comes from the verb 'to cut'. A literal interpretation of this juxtaposition would be 'impossible to break'. The fact that matter was structured this way was the idea of Leucippus and Democritus 2400 years ago. Today we have been able to break the atom and see components of on oddity beyond the imagination of the Greek philosopher. Knowledge has become specialised and modelling of nature has moved from schematic representations to complex theories which are verified with the help of machines.

We no longer think of matter as being constituted of simple building bricks, which have clear boundaries and simple shapes. Atoms now are governed by differential equations which are more complex than those which describe the Solar System. The modern development of quantum physics and the contemporary computational revolution make this era ideal for the study of the atom and of the microscopic world. Today, most of humanity is aware of the enormous energies which govern the atomic world, which unfortunately have made themselves visible through very destructive means.

The canonical states of matter consist of solids, liquids and gases. But modern physics deals with a plethora of other states which do not fall under this classical categorisation: liquid crystals, super-fluids, plasmas, and Bose-Einstein Condensates are some of the states which break the established trichotomy. The work covered in this thesis focuses on Bose-Einstein Condensates and dilute gases, which are exotic states of matter, that must be created under laboratory conditions since they do not

occur spontaneously in our habitats.

With the work of de Broglie, it became apparent that matter and waves are not separate entities in quantum physics, but notions which coexist for both light and atomic matter. De Broglie famously linked the wave-length (λ) of a corpuscule with its momentum (p), through the equation [1]

$$\lambda = h/p, \tag{1}$$

where $h = 6.63 \times 10^{-34}\ \ m^2 \times kg \times s^{-1}$ was used to denote Planck's constant.

When the average distance between atoms becomes smaller than their de Broglie wave-length because of cooling below a very low threshold, they start to condense into a single wave-function, and act as a Bose-Einstein Condensate. This type of behaviour was first hypothesised by Satyendra Bose and Albert Einstein in 1925 [2] and was first realised in an experimental set-up in 1995, in Colorado by Cornell and Wieman [3]. The University of Strathclyde was the first place in Scotland to create an experimental BEC in 2003.

While the early development of quantum mechanics forced the rapid expansion of linear algebra, and gave rise to a rich formalism through the works of Bohr, Pauli, Heisenberg, Schrödinger and many others, modern quantum physics also deals with non-linear problems. Bose-Einstein Condensates are described by a non-linear Schrödinger Equation, with rich dynamics, strongly influenced by chaos. Lorenz discovered chaos in 1963, almost half a decade after Bose's initial hypothesis on the existence of BECs. Due to the recent developments in computational power, and due to the keen contemporary interest in exotic states of mater, this is an ideal time for the computational study of BECs.

The work presented in this PhD thesis focuses on the theoretical and computational analysis of models describing BECs in optical lattices formed by two counter-propagating laser beams. Remarkably, the same dynamical equations can be applied

to describe the propagation of laser light in an array of optical fibres, thus extending greatly the possible applications of the results discussed in this thesis.

Chapter 1

Introduction

In order to study the physics of Bose-Einstein Condensates (BECs) we will use the equation derived by Gross and Pitaevskii in 1961 [4–6]. This equation is also referred to as the Non-Linear Schrödinger Equation (NLSE) and it is a very powerful tool not only in physics, but also in other scientific fields, such as biology, chemistry and multi-disciplinary engineering areas like material science. One can discretise the NLSE using finite difference calculus [7] to arrive to the Discrete Nonlinear Schrödinger equation (i.e. the DNLSE, derived in Section 1.1). As physicists, we are mostly interested in the applications of the DNLSE which focus on the dynamics of BECs [8] and on the propagation of light in arrays of optical wave-guides [9]. The DNLSE is characterised by localised modes known as breathers, localised modes which periodically pulsate in time. The stability of breathers in the presence of noise is a highly complex issue, as it will become apparent throughout extensive parts of this work. Breathers are also characteristic of vibrational modes present in macro-molecules, appearing in DNA and RNA molecules [10, 11], in protein [12] and in polymers [13]; they are also ways through which topological defects propagate in solid state crystals [14, 15]. The study of breathers is also an issue of strong relevance for coupled quantum transport, which is of high interest in the current scientific context [16–18].

The Non-Linear Schrödinger Equation, also known as the Gross-Pitaevskii equation,

developed by Lev Pitaevskii and Eugene Gross [4–6] in 1961 takes the following form

$$i\hbar\frac{\partial}{\partial t}\psi(\underline{r},t) = \left[-\frac{\hbar^2}{2m}\nabla^2 + U(\underline{r},t) + g|\psi(\underline{r},t)|^2 \right]\psi(\underline{r},t), \tag{1.1}$$

where $\psi(\underline{r},t)$ is the wave-function which evolves under the action of the NLSE, in the presence of a periodic external potential $U(\underline{r},t)$, for a scattering amplitude of g, which is defined as

$$g = \frac{4\pi\hbar^2 a_S}{m}, \tag{1.2}$$

where $\hbar$ has its canonical meaning, representing the reduced Planck constant $\hbar \equiv \frac{h}{2\pi}$ and a_S is the scattering length of the bosons, which all have the identical mass m. Moreover, the wave function is normalised, such as

$$\iiint dV|\psi|^2 = N, \tag{1.3}$$

where N is the number of bosons in the condensate.

The NLSE (1.1) is a very general differential equation, which proves to be highly effective to describe the behaviour of bosons in the presence of external potentials. However, the wave-function depends on a three dimensional position vector, through the generic variable $\underline{r}$.

The focus of this work is on one-dimensional lattices, which are generated using two counter propagating lasers. The external potential will therefore take the shape of a standing wave with a period equal to half of the wave-length of the trapping lasers. It is therefore useful to arrive at a discrete one-dimensional approximation of the NLSE, which allows the implementation of elegant numerical investigative techniques.

Our interest on one-dimensional lattices arises from modern experimental realisations on one-dimensional BECs [19, 20], through Feshbach resonance trapping [21]. These condensates can be either doughnut-shaped (as we see depicted in Figure 1.1), or can be cigar-shaped (as we see in Figure 1.2)). BECs are usually created with di-

lute alkali gases, using elements from the first group in the periodic table. This is also the case for the two examples provided in Figures 1.1 and 1.2 where ^{23}Na and ^{7}Li have been used. Alkali metals have simple orbital configurations (and therefore obey simple models for their inner energies), and are bosons, which makes them ideal candidates [22, 23] for the cooling techniques which are currently employed by the cold atoms community [24], such as Doppler cooling and magnetic trapping techniques.

One-dimensional condensates only require one degree of freedom when describing their wave-functions analytically. This axis is suitably chosen, depending on the shape of the condensate; it is either the longitudinal coordinate, which measures the position in the cigar-shaped condensate where we measure the mass density or the polar angle, which measures the amount of matter present under a certain angle. In both cases we concentrate all the mass from a surface element (a cross section of the condensate) into a single point, reducing the dimensionality of the problem from 3 to 1.

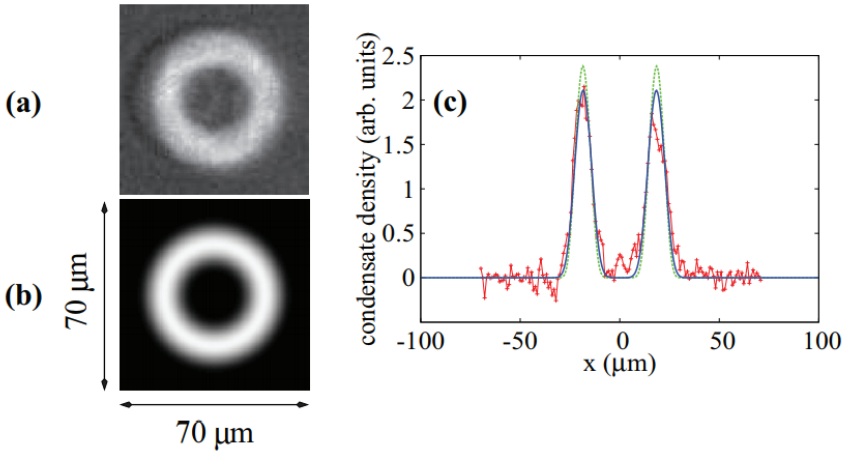

Figure 1.1: Experimental realisation of a doughnut-shaped BEC by N. Murray et al [19] for a cloud of 4×10^5 ^{23}Na atoms. (a) Experimental Realisation; (b) Theoretical Prediction; (c) Diametric Cross Section.

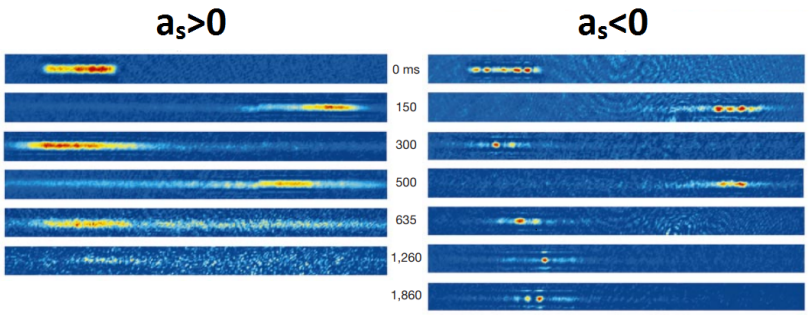

Figure 1.2: Experimental realisation of a cigar-shaped BEC by K. Strecker et al [20] The left panels correspond to profiles of BECs with repulsive interactions, while the right panel corresponds to attractive boson-boson interactions. Here, the condensate consists of 3×10^5 ^{7}Li atoms.
Reprinted figure with permission from Springer Nature. Copyright (2002) by Springer Nature `https://doi.org/10.1038/nature747`

1.1 From the Gross-Pitaevskii equation to the DNLSE

Throughout this work we will refer to one-dimensional lattices, and we automatically imply that we are referring to cigar-shaped condensates, where the spatial dependence is solely limited to the longitudinal axis z.

The differential equation from (1.1) originates from a generic action functional of the type

$$\mathcal{S}_{3D} = \int dt \langle \hat{L} \rangle = \iiiint dx dy dz dt \;\; \psi^* \hat{L} \psi, \tag{1.4}$$

where $\langle \hat{X} \rangle$ denotes the expectation value of a given operator $\hat{X}$. Since we are dealing with complex functions, we have ket vectors of the type $|\psi\rangle \equiv \psi \in \mathbb{C}$, and bra vectors of the type $\langle \psi | \equiv \psi^*$. The scalar product is defined using the canonical definition $\langle \psi | \xi \rangle = \iiint dx dy dz \;\; \psi^* \xi$

The operator $\hat{L}$ is the Lagrangian of the NLSE and is equal to

$$\hat{L} \equiv i\hbar \frac{\partial}{\partial t} + \frac{\hbar^2}{2m} \nabla^2 - U(\underline{r}, t) - \frac{1}{2} g |\psi(\underline{r}, t)|^2, \tag{1.5}$$

which is similar to the cumulative operator acting on $|\psi\rangle$ in the NLSE (1.1) after all the terms have been moved on the same side, with the only difference at the nonlinear term,

which now has a pre-factor of $\frac{1}{2}$. As one might expect, the only component which will not obey the additive laws of linear algebra will be the non-linearity. This apparently minor nuisance will make all analytical studies of the NLSE highly complex and will make the use of numerical investigations almost compulsory.

We can therefore reconstruct the equation using the Euler-Lagrange formalism on the action

$$\mathcal{S}_{3D} = \iiiint dxdydzdt\psi^*\Big(i\hbar\frac{\partial}{\partial t} + \frac{\hbar^2}{2m}\nabla^2 - U(\underline{r},t) - \frac{1}{2}g|\psi|^2\Big)\psi. \tag{1.6}$$

In the case of cigar-shaped condensates, we are dealing with systems with cylindrical symmetries, where the potential on the z axis and in the plane transversal to this are additive [25]. This means that the periodic potential becomes

$$U(\underline{r},t) = \frac{1}{2}m\omega_\perp^2(x^2+y^2) + V(z) \tag{1.7}$$

where $\omega_\perp$ is the transversal trapping frequency, and is much higher than the lattice frequency along z. This induces a strong separation of spatial scales, which allows us to focus on z only. The strong decoupling between the spatial coordinates allows us to write the wave function [25] as a product of the form

$$\psi(\underline{r},t) = \phi(x,y,t;\sigma(z,t)) \times f(z,t). \tag{1.8}$$

The classical assumption made here is that the transversal potential is deep enough that we always find ourselves in the ground state of a quantum harmonic oscillator, given by a Gaussian of the sort

$$\phi(x,y,t;\sigma(z,t)) = \frac{\exp\Big[-\frac{x^2+y^2}{2\sigma^2(z,t)}\Big]}{\sqrt{\pi}\sigma(z,t)}. \tag{1.9}$$

From this Gaussian dependency (1.9), we see that the wave-function decays very

fast in the transversal plane, away from the z axis given by $x = y = 0$. The cigar-shaped condensate will consist of multiple parallel disks of the same radius. This radius is very well approximated by the quantity $\sigma(z,t)$.

The wave-function $\psi(\underline{u},t)$ can be replaced with the product Ansatz from (1.8) in the action functional. One can also take advantage of the fact that the wave-function is strongly confined along the z-axis, to approximate the Laplacian operator with $\nabla^2 \approx \frac{\partial^2}{\partial x^2} + \frac{\partial^2}{\partial y^2}$. After performing all integrations along the x and y axes, we can reduce the action functional to

$$\begin{aligned}\mathcal{S}_{1D} = \iint dzdt f^*\Big(i\hbar\frac{\partial}{\partial t} + \frac{\hbar^2}{2m}\frac{\partial^2}{\partial z^2} - \frac{\hbar^2}{2m\sigma} - \\ -V(z) - \frac{m\omega_\perp^2\sigma^2}{2} - \frac{1}{4\pi\sigma^2}g|f|^2\Big)f.\end{aligned} \tag{1.10}$$

Applying the product Ansatz helped us reduce the Lagrangian density to $\mathcal{L}_{1D} = f^*\Big(i\hbar\frac{\partial}{\partial t} + \frac{\hbar^2}{2m}\frac{\partial^2}{\partial z^2} - \frac{\hbar^2}{2m\sigma} - V(z) - \frac{m\omega_\perp^2\sigma^2}{2} - \frac{1}{4\pi\sigma^2}gff^*\Big)f$. This Lagrangian contains three generalised coordinates $\{q_1 = f, q_2 = \sigma, q_3 = f^*\}$, which must obey the Euler-Lagrange equations

$$\frac{\partial\mathcal{L}_{1D}}{\partial q_i} - \frac{\partial}{\partial t}\Big(\frac{\partial\mathcal{L}_{1D}}{\partial\dot{q}_i}\Big) = 0 \quad \forall i. \tag{1.11}$$

Applying these on the one-dimensional Lagrangian density leads to two independent equations (the equations for f and $f*$ lead to identical equations, since they are simply complex conjugates of each other)

$$\begin{aligned}&\Big(i\hbar\tfrac{\partial}{\partial t} + \tfrac{\hbar^2}{2m}\tfrac{\partial^2}{\partial z^2} - \tfrac{\hbar^2}{2m\sigma} - V(z) - \tfrac{m\omega_\perp^2\sigma^2}{2} - \tfrac{1}{2\pi\sigma^2}g|f|^2\Big)f = 0 \\ &\tfrac{\hbar^2}{2m\sigma^3} - \tfrac{m\omega_\perp^2\sigma}{2} + \tfrac{1}{4\pi\sigma^2}|f|^2 = 0.\end{aligned} \tag{1.12}$$

If we introduce the notation $a_\perp^2 \equiv \frac{\hbar}{2m}$, we can express the value of the standard deviation of the Gaussian modes from the second Euler-Lagrange equation

$$\sigma^2 = a_\perp^2\sqrt{1 + 2a_s|f|^2}, \tag{1.13}$$

where a_S is the scattering length of the bosons.

At this stage, one can introduce σ into the first Euler-Lagrange Equation to arrive at the one-dimensional Gross-Pitaevskii Equation

$$i\hbar\frac{\partial f}{\partial t} = \Bigg[-\frac{\hbar^2}{2m}\frac{\partial^2}{\partial z^2} + V(z) + \frac{g|f|^2}{2\pi a_\perp^2\sqrt{1+2a_s|f|^2}} + \frac{\hbar\omega_\perp}{2}\Big(\frac{1}{\sqrt{1+2a_s|f|^2}} + \sqrt{1+2a_s|f|^2}\Big)\Bigg] f \tag{1.14}$$

which is now fully confined to the z-axis.

In the dilute gas regime, the scattering length is very small, such that $2a_s|f|^2 \ll 1$, therefore one can make the approximation $\sigma^2 = a_\perp^2\sqrt{1+2a_s|f|^2} \approx a_\perp^2$, which dramatically simplifies the one-dimensional Gross-Pitaevskii equation (i.e. the NLSE) to

$$i\hbar\frac{\partial f}{\partial t} = \Bigg[-\frac{\hbar^2}{2m}\frac{\partial^2}{\partial z^2} + V(z) + \frac{g|f|^2}{2\pi a_\perp^2}\Bigg] f, \tag{1.15}$$

the term $\hbar\omega_\perp$ has been left out, since it only induces a rotation with a constant frequency, which does not pose any interesting physics to our problem.

Using the full analytical expression of the non-linearity coefficient g (1.2), and the fact that the periodical potential is usually modelled as the square of a sinusoidal function, i.e. $V(z) = E_0\sin^2\left(\frac{\pi z}{L}\right)$, where E_0 is a parameter which tunes the depth of the potential and $\frac{2\pi}{L}$ is the lattice spatial frequency, we arrive at

$$i\hbar\frac{\partial f}{\partial t} = \Bigg[-\frac{\hbar^2}{2m}\frac{\partial^2}{\partial z^2} + E_0\sin^2\left(\frac{\pi z}{L}\right) + 2\hbar a_S\omega_\perp|f|^2\Bigg] f. \tag{1.16}$$

We now see that the lattice potential, given by $E_0\sin^2\left(\frac{\pi z}{L}\right)$ can also be written as

$$E_0\sin^2\left(\frac{\pi z}{L}\right) = \frac{E_0}{2}\exp\left(0\times\frac{2\pi z}{L}\right) - \frac{E_0}{4}\exp\left(i\times\frac{2\pi z}{L}\right) - \frac{E_0}{4}\exp\left(-i\times\frac{2\pi z}{L}\right) \tag{1.17}$$

where $\frac{2\pi}{L}$ will be the reciprocal lattice vector (a periodicity of L corresponds, unsur-

prisingly to a periodicity of $\frac{2\pi}{L}$ in reciprocal space).

At this stage, it is convenient to rescale the variables, as done by Efremidis et al. in Ref. [7] and define

$$\begin{aligned} T_0 &= \tfrac{mL^2}{4\hbar} \\ T &= \tfrac{t}{T_0} \\ Z &= \tfrac{2z}{L} \\ L_1 &= \omega_\perp |a_S| \tfrac{mL^2}{2\hbar} \\ u &= f\sqrt{L_1} \\ E_r &= \tfrac{4\hbar^2}{mL^2} \\ V_0 &= \tfrac{E_0}{E_r}, \end{aligned} \tag{1.18}$$

which change the differential equation to

$$i\frac{\partial u}{\partial T} = \left[-\frac{1}{2}\frac{\partial^2}{\partial Z^2} + V_0 \sin^2\left(\frac{\pi Z}{2}\right) + \text{sign}\,(a_S)|u|^2 \right] u. \tag{1.19}$$

The lattice spacing L has typical values of the order of magnitude $1\mu m$ (half of the wave-length of the trapping laser), while the lattice depth V_0 usually takes values of the order $10E_r$ but can reach to values up to $1000E_r$ for very deep potentials. E_r is the recoil energy defined at (1.18) and represents the kinetic energy of an atom after emitting a single photon if it was initially at rest.

At this stage, the differential equation is reduced to one dimension, translated into dimensionless units, and as compact as it can possibly get. In the case when the periodic potential is deep enough to allow the existence of the first Wannier-Bloch mode, we can build the discrete version of this equation. We begin this process by isolating the linear part of (1.19), and looking at its band structure. This implies solving the eigenvalue equation

$$Ev = -\frac{1}{2}\frac{\partial^2 v}{\partial Z^2} + V_0 \sin^2\left(\frac{\pi Z}{2}\right) v. \tag{1.20}$$

that will dictate the shape of this band structure. The Ansatz for the potential is periodic (the square of a sinusoidal), therefore we expect the eigenfunctions to be pe-

riodic as well. Under the Floquet-Bloch theory [7] the eigenfunctions take the shape $v_k(Z) = V_k(Z)\exp(ikZ)$ (an Ansatz similar to the Fourier Series presented at (1.17)), where k is a wave vector which characterises the momentum within the lattice, and $V_k(z)$ is a periodic function with a periodicity identical to that of the optical lattice. Within the first Brillouin zone, defined as the smallest possible region confined by the Bragg hyper-planes of the reciprocal lattice [26], V_k is unique. Here we are making use of the fact that if we know how a periodic function behaves for a single period, we know everything about its general shape. The first Floquet-Bloch mode both for the centre and the end of the band is a Gaussian centred around $Z = 0$. In between bands, the modes will decay exponentially with a coefficient $k_i = -2E - \frac{\pi^2}{4} + V_0 + \pi\sqrt{2E - V_0 + \left(\frac{V_0}{\pi}\right)^2}$ [7]. This exponential decay also represents the origin of the exponentially decaying tails of the soliton, which we will describe in more detail later on. The DNLSE is derived in the tight-binding approximation, under the assumption that atoms are strongly bound by the potential well, which is deep enough to allow discretisation. The depth should not be too large though, so that only the ground state of the Floquet-Bloch modes (the Gaussian) is accessible.

At this stage, we can return to the equation from (1.19) and use the Wannier Ansatz [7], which is very popular in the literature

$$u(Z,T) \equiv \sum_n C_n(T)\exp(-iET)\,|\phi_n(Z)\rangle\,, \tag{1.21}$$

where E denotes the eigen-energies of the linear part of the Schrödinger equation, and the eigenfunctions $|\phi_n(Z)\rangle$ have been normalised. The exponentially decaying rate for the modes, together with the normalisation condition implies that

$$1 = \langle\phi_n|\phi_n\rangle \gg \langle\phi_n|\phi_{n+1}\rangle \gg \langle\phi_n|\phi_{n+2}\rangle\,. \tag{1.22}$$

At the base of the bands $k = 0$, and all eigenstates $|\phi_n(Z)\rangle$ are real. We can now use this information, together with the Wannier Ansatz from (1.21), to turn the NLSE

from (1.19) into

$$\sum_n (i\dot{C}_n |\phi_n\rangle + EC_n |\phi_n\rangle) = \sum_n \Big(-\frac{1}{2} C_n \Big| \frac{\partial^2}{\partial Z^2} \phi_n \Big\rangle + \\ + C_n \Big| V_0 \sin^2 \Big(\frac{\pi Z}{2} \Big) \phi_n \Big\rangle + \mathrm{sign}(a_S) |C_n|^2 C_n |\phi_n^3\rangle \Big). \tag{1.23}$$

The eigenvalue equation (1.20) can be applied at all locations with $Z = mD$, where D is the spatial periodicity of the lattice, and $m \in \mathbb{Z}$. The underlying assumption is that at $Z = 0$ we start with the bottom of a well and this follows from the initial Ansatz $V(Z) = V_0 \sin^2 \left(\frac{\pi Z}{2} \right)$. The eigenvalue equation at the bottom of the wells becomes

$$EC_m |\phi_m\rangle = -\frac{1}{2} C_m \Big| \frac{\partial^2}{\partial Z^2} \phi_n \Big\rangle + C_m \Big| V_0 \sin^2 \Big(\frac{\pi m D}{2} \Big) \phi_n \Big\rangle. \tag{1.24}$$

The eigenvalue equation at (1.24) can be subtracted from the full expression of the NLSE at (1.23). Once this process is completed, one can apply the tight-binding approximation to arrive at the more compact expression

$$i\dot{C}_n = \eta C_n - \kappa (C_{n-1} + C_{n+1}) + \gamma |C_n|^2 C_n \tag{1.25}$$

where η, κ and γ are the dominant terms in what is left from the sums at (1.23) after the subtraction of the eigenvalue equations. All other terms are neglected, since they are assumed to decay exponentially fast. One can now use the transformation $D_n \equiv C_n \exp(-i\eta T)$ to reduce the parameter space and arrive to the more friendly equation

$$i\dot{D}_n = -\kappa (D_{n-1} + D_{n+1}) + \gamma |D_n|^2 D_n, \tag{1.26}$$

which is almost identical to (1.25), but it is in a rotational frame where the frequency η has disappeared. Ultimately, we arrive to the Discrete Nonlinear Schrödinger Equation

(DNLSE) which will be used throughout this work, given by

$$i\dot{z}_n = -2|z_n|^2 z_n - z_{n-1} - z_{n+1}. \tag{1.27}$$

This will be the central topic of the thesis. The parameters γ and κ can be scaled out. Here, the choice was to set them at $\gamma = -2$ and $\kappa = 1$. These parameters will be kept constant throughout the work. Occasionally, the DNLSE will be modified to allow dissipation, and will take the shape [27]

$$i\dot{z}_n = -2|z_n|^2 z_n - z_{n-1} - z_{n+1} - i\Gamma z_n \delta_{n,1} - i\Gamma z_n \delta_{n,M}, \tag{1.28}$$

where M is the length of the chain, δ_{jk} is the Kronecker delta, and Γ is a dissipation coefficient, which is usually set equal to 1, when the condensate is allowed to dissipate.

In some cases, the condensate will be set to interact with thermostats, which will be modelled as Langevin heat baths. This kind of approach, however, is discussed in deeper detail in the main body of the thesis, where we will touch the analytical considerations, the numerical algorithms and the calibration checks associated with stochastic heat baths.

The DNLSE is a complex differential equation, which can be split into real and imaginary components. Most of the simulations will be ran in `Matlab`, which has pre-existent libraries that can integrate complex differential equations. These functions however perform very poorly, so that a split into real and imaginary parts is essential to ensure a good accuracy of the results. Moreover, the fourth-order Runge-Kutta integrator already available in the library was deemed as unreliable, and most integrator functions have been re-written entirely. Most of the problems studied in this thesis deal with open systems, where the use of symplectic integrators, such as those developed by Yoshida [28] is impossible.

1.2 Discrete Breathers in the DNLSE

As for most non-linear equations, one of the most fundamental investigations that one can do is to look for stationary points. The stationary points of the DNLSE (1.28) are localised modes which are referred to as breathers. The breathers described at the beginning of this chapter are therefore nothing else than solutions of the non-linear equation which rotate in time with a constant frequency ω, which characterises the 'breathing' dynamics and explains the etymology of their name. In the ideal scenario (for which one can build complete analytical solutions of the DNLSE), the Bose-Hubbard chain has infinite length, and all sites are phase locked (or perfectly synchronised). This implies that all the lattice sites will rotate with the same exact frequency Ω. The phase space therefore will be given only by amplitudes, since all the relative phases in the chain are constant in time, and absolute phase bears no physical meaning. For an ideal breather, therefore, the state is given only by the real amplitudes of the sites it occupies.

One can now substitute all wave-functions z_n with the Ansatz $z_n \equiv A_n \exp(i\phi_n)$, and express the DNLSE as

$$\dot{A}_n = A_{n-1}\sin(\phi_n - \phi_{n-1}) + A_{n+1}\sin(\phi_n - \phi_{n-1}) \tag{1.29}$$

$$A_n\dot{\phi}_n = 2A_n^3 + A_{n-1}\cos(\phi_n - \phi_{n-1}) + A_{n+1}\cos(\phi_n - \phi_{n-1})\ . \tag{1.30}$$

by splitting (1.27) into its real and imaginary components. Ultimately, one can use the fact that for a breather all sites rotate in phase, i.e. $\phi_n = \Omega t\ \forall\ n$ to simplify the phase equation to

$$\Omega A_n = 2A_n^3 + A_{n-1} + A_{n+1}, \tag{1.31}$$

where the term proportional to $\dot{A}_n$ has been omitted, since this equation must be valid for stationary states, where all derivatives are exactly equal to zero.

We now have been able to reduce the dimension for the phase space of the stationary

state by a factor of two, by eliminating all phases. In literature, the phase locking occurs in one of two ways [29]

- the phase differences between adjacent sites are all 0, i.e. $\delta\phi \equiv \phi_i - \phi_{i+1} = 0$, and the breather rotates with a positive frequency Ω. This means that the phase at all sites increases monotonously and linearly with time. This is the solution we will focus on throughout this work, which bears the name of 'unstaggered breather'

- phase differences between adjacent sites are all π, i.e. $\delta\phi \equiv \phi_i - \phi_{i+1} = \pi$, and one must replace A_n with $(-1)^n A_n$ (the staggering transformation [29]) in equation 1.31. In this case $\Omega < 0$, and the phases will decrease linearly with time.

Changing the sign of the variables with an odd (or even) index allows the transition from one regime to the other. In practice, the two regimes are formally equivalent. For most values of the non-linearity (depicted by γ in equation (1.26)), we can encounter two types of stationary points

1. Sievers-Takeno (ST) breathers [30], where most of the mass is concentrated into one site only, and all neighbouring sites have exponentially decaying occupancy numbers.

$$A_n^{ST} = A_0 \exp(-a_1|n|). \tag{1.32}$$

2. Page (P) breathers [31], where two sites have the same value of the mass, and from this central dimer, all other sites have exponentially decaying amplitudes.

$$A_n^{P} = A_P \exp(-a_2|n + 1/2|). \tag{1.33}$$

These types of breathers are also depicted in Figure 1.3.

The breathers which are of interest to us are the Sievers-Takeno breathers, which are highly localised to one site only. This is mostly because of the fact that they have much higher stability than Page breathers, which will be associated more with bound

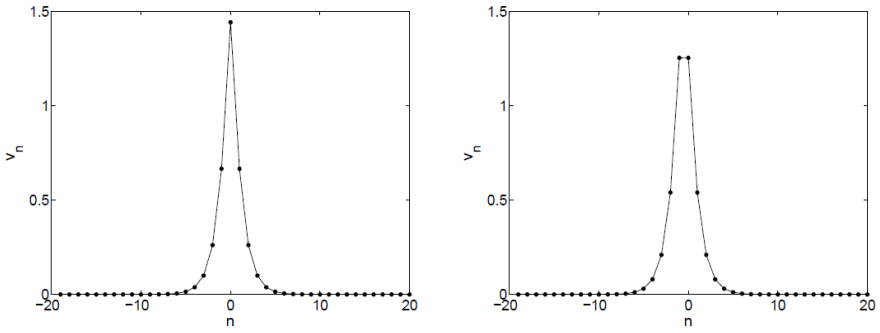

Figure 1.3: Amplitude profile of a stationary point of the DNLSE, for an infinitely extended one-dimensional lattice. The left plot shows the shape of a Sievers-Takeno breather, while the right plot displays the Page solution. These diagrams have been obtained by Cuevas et al. [29], for a frequency $\Omega = 1$ and for $\gamma = \kappa = 1$ in 1.26 (Equal values for the tunnelling coefficient and of the non-linearity).

states than with actual stationary states in the work that will follow. For the ST breathers, one also has the additional relation $\exp(-a_1) \propto \Omega$ [29], which can be used to approximate the frequency of the breather.

It is possible to link the frequencies of these breathers with the overall norm of the system, which is obtained by evaluating the infinite sum

$$\mathcal{N} = \sum_{n=-\infty}^{\infty} A_n^2, \tag{1.34}$$

which must converge to the mass of the condensate.

The stationary state equation for Sievers-Takeno breathers can be obtained by replacing all amplitudes with Ansatz (1.32) (i.e. $A_n = A_0 \exp(-a_1|n|)$) in equation (1.31) to arrive at

$$\Omega = 2A_0^2 + 2\exp(-a_1) \approx 2A_0^2, \tag{1.35}$$

which gives the approximate frequency of the breather.

It is important to note, however, that physical systems cannot have infinite lengths and therefore both ST and P breathers are highly theoretical. Not only that, but

systems cannot be perfectly closed, since they must interact with thermostats and are subject to dissipation. In Ref. [27], a much more realistic model is presented, where the lattice length is finite, and the system encounters dissipation at the ends of the chain, which alters the shape of the breather in time. What is remarkable there is that, even if the breather is no longer in the ideal set-up, most of the mass nevertheless remains concentrated into a single site, which will rotate at a frequency which under a first approximation is still

$$\Omega \approx 2A_0^2. \tag{1.36}$$

Therefore, when small dissipative terms are introduced in the system, through equation (1.28), the breather still keeps its very localised shape, concentrating up to 99.5% of the atoms into just three sites [27]. This strong localisation will be observed throughout this work, even in the presence of much larger backgrounds.

Eckmann [32] shows how, in the presence of small backgrounds, even when the lattice length is finite, breathers evolve towards a state where one of the sites concentrates most of the energy, and all the nearest neighbours have exponentially decaying amplitudes. Therefore, even if the lattice is finite and the system is open, one will still observe the same exponentially decaying tails as in (1.32).

Later in the work, we will see that in the presence of large backgrounds (of order of magnitude $\mathcal{O}(1)$), the frequency of the breather is still given by $\omega \approx A_0^2$ (see also [33]). This will imply that the rotation of the breather will purely be a function of its intensity. It almost seems as if the breather decouples from its surroundings, rotating independently of the dynamics of the background. In addition to this, wave-functions in the background are no longer phase locked, being described by rotational spectra which are completely separated from the frequency of the breather (as one can see in the work of Rumpf [34]). The theory of staggered and unstaggered breathers loses validity, since the neighbouring sites start to become uncorrelated from the rotation of the breather.

This type of computational modelling is more in line with the experimental findings presented in Figure 1.2, where the lattice size is finite (as one naturally expects for a physical system), and most locations in the one-dimensional system have relatively large occupancy numbers.

It follows from here that there is a need of new theoretical approaches, where the background does not simply consist of negligibly small noise (like in [35–37]), and the size of the lattice is affected by limited size effects. All the analytical apparatus and the computational methods which will be developed will work under the more broad assumption that breathers are allowed to interact with large backgrounds, with sizes of $A_j \approx \mathcal{O}(1)$. Rumpf describes in Ref. [34] the background amplitudes as having probability densities with exponentially decaying tails. This implies, that for all backgrounds, there are very rare situations in which a strong phonon excitation can occur, which can ultimately strongly perturb the breather. As a matter of fact, he studies this problem in further detail in [38], where he shows that during the collision of a breather with a large excitation, the breather might migrate towards the incoming excitation and absorb its energy. It is not clear however, why this migration happens - in his work, Rumpf was more concerned with identifying thresholds for this type of migration [39], than in trying to characterise and quantify them.

Attempts at building a theoretical framework for the migration of breathers have been done on trimers in Ref. [40], through the use of Peierls-Nabarro potentials. Their theory suggests that there exists a threshold for the trimer configuration which can destabilise the breather and can make it migrate to a neighbouring site. This theory does not, however have a very clear extension to lattices of generic length. For example, in [41] the authors try to extend the analytical predictions for a known trimer solution (single depleted well) to hexamers - their attempt produces very specific solutions which separate very fast from their analytical prediction. This happens due to the presence of chaos. Flach et. al [42] have shown that a trimer already exhibits chaotic dynamics, with a broad range of complexity. This means that even if we start in the vicinity

of a single depleted well solution, we will soon diverge from the known analytical model. We therefore expect as we move to lattices of generic length to see highly chaotic trajectories. Molina et al. [43] have shown almost three decades ago that large excitations in spatially extended lattices can still become pinned to a single site (and act as breather), with trapping statistics which do not differ significantly from those of the trimer. We therefore expect to see no fundamental topological differences between trimers and spatially extended lattices when performing analytics on the DNLSE, even if all of the calculations will be strongly affected by chaos.

During all numerical tests, one can observe that breathers which are localised in a single lattice site (of type ST) are far more stable than breathers with peaks over two neighbouring sites (P solitons). As a matter of fact, one can argue that P breathers are nothing else than bound states in contact with extended lattices. Their stability is poor, since large backgrounds rapidly destroy any pre-existing synchronisation between the background and the breather. The P soliton therefore will almost immediately turn into a bound state with a random phase difference between the two sites in the dimer. In isolated dimers, any small difference between the intensity of the two neighbouring sites will lead to a periodic motion [44] which

1. Either consists of a periodic fluctuation in the breather height, during which the overall mass of the dimer is still conserved.

2. Or consists of a periodic zigzag migration of the breather from one site to the other.

When put in contact with spatially extended lattices, all P solitons will break their symmetry instantaneously (the two central amplitudes will become different very rapidly), and this will lead to a fast transition towards a bound state. The bound state itself is very unstable when put into contact with the rest of the lattice, as we will later see. It can survive for long enough however (times of the order $\mathcal{O}(10^3)$) to trigger the migration of the breather to a neighbouring location.

It therefore follows that it would be highly desirable to be able to quantify and classify the interactions between breathers and large backgrounds. Most of the models in this work do not deal with infinitesimal backgrounds (which have already been covered extensively in the literature [32, 35–37], but take their smallness parameter from the frequency of the breather, through the inverse proportionality law

$$\varepsilon \equiv \frac{1}{\omega} \tag{1.37}$$

where ω is the frequency of the fast rotation of the breather.

Even in the presence of large backgrounds, breathers are highly stable structures. Instead of synchronising with their surroundings (like in the case of the ideal, infinitely extended model), breathers tend to decouple, due to the emergence of more than one time scale. A natural question which arises in this situation is up to which order of the smallness parameter ε is a pinned breather still a stationary point of the DNLSE. We can find this out by identifying the first power of ε for which the perturbed DNLSE induces a slow drift on the breather mass. This will be done by making use of asymptotic expansions, multiple time-scale analysis and averaging techniques.

We are also interested to find out whether it is only the creation of bound states that destabilises breathers, or whether there are more types of events which contribute to sudden changes of the breather shape. A thorough classification and analysis of these events is highly desirable for understanding how the dynamics of breathers depends on the size and thermal properties of the background. Identifying these events is also a way to distinguish:

- **Laminar Dynamics** – during which breathers are frozen for very long period of time; their positions do not change and their intensities drift very slowly from their initial values, while their phases increase linearly, like for any canonical harmonic oscillator.

- **Turbulent Dynamics** – during which breathers suddenly change location and

size, or in rare circumstances they can disappear altogether, by abruptly dissipating all their energy and mass into the lattice.

When a laminar regime can be defined, we are interested in constructing a predictor-corrector type of integration, where the very small time step imposed by the frequency of the breather can be replaced with a large time step, which is still small enough to allow for an accurate integration of the background dynamics. In order to do this, one must be able to identify clear domains where the system is laminar, and domains where the system is turbulent, and change time steps when transitioning from one regime to another. This type of transition is described in Ref. [45] and is characteristic of a Heterogeneous Multiscale Method (HMM), where a macro-integrator is used for the laminar regime and a micro-integrator is used for the turbulent events. Not all HMM methods are constructed like this; some of them consist of consecutive transitions from one integrator to the other [46] - however, this type of integration assumes a universal applicability of averaging. As we will later see in this work, the DNLSE is not averageable at all points.

At this stage, it is useful to express the DNLSE in the language of Hamiltonian mechanics. In order to do that, one must split the equation from (1.27) into its real and imaginary parts to arrive to

$$\dot{x}_n = -2y_n(x_n^2 + y_n^2) - y_{n-1} - y_{n+1} \tag{1.38}$$

$$\dot{y}_n = +2x_n(x_n^2 + y_n^2) + x_{n-1} + x_{n+1} \, . \tag{1.39}$$

where one has used the canonical Ansatz $z_n \equiv x_n + iy_n$.

Working with the coordinates $p_j = x_j\sqrt{2}$ and $q_j = y_j\sqrt{2}$ rescales the differential equations above into

$$\dot{p}_n = -q_n(p_n^2 + q_n^2) - q_{n-1} - q_{n+1} \tag{1.40}$$

$$\dot{q}_n = +p_n(p_n^2 + q_n^2) + p_{n-1} + p_{n+1} \, . \tag{1.41}$$

The same differential equations are generated by the Bose-Hubbard Hamiltonian

$$H_{BH} \equiv \frac{1}{4}\sum_{j=1}^{N}\left(p_j^2+q_j^2\right)^2+\sum_{j=1}^{N-1}\left(p_jp_{j+1}+q_jq_{j+1}\right) \tag{1.42}$$

using Hamilton's formalism, i.e.

$$\dot{p}_n = -\partial_{q_j}H_{BH} \tag{1.43}$$

$$\dot{q}_n = +\partial_{p_j}H_{BH}\ . \tag{1.44}$$

It therefore follows that the DNLSE can also be expressed in terms of Generalised Canonical Coordinates, from the Bose-Hubbard Hamiltonian introduced at (1.42).

While the breather dynamics are split into turbulent and laminar domains, the background evolution is characterised by thermodynamics parameters. The state of the background 'lives' in a two dimensional space; a macro-state can be specified using either temperature and chemical potential $\{T,\mu\}$ or by specifying

1. the amplitude (mass) density which is given by $a=\frac{\mathcal{N}}{N}$, where $\mathcal{N}$ is the total mass of the background and N is the number of sites in the background;

2. and the Hamiltonian (energy) density, which is given by $h=\frac{H_{BH}}{N}$, where H_{BH} is the Bose-Hubbard Hamiltonian from (1.42) which generates the DNLSE.

The work of Franzosi [47] focuses specifically on systems governed by time independent Hamiltonians with an additional conserved quantity. Using this work, it is possible to define a temperature (T) and a chemical potential (μ) for the Bose-Hubbard chain in a micro-canonical configuration (i.e. in the absence of dissipations or thermostats). In Chapter 2, the exact expressions of these quantities are given, together with a description of the numerical methods used to evaluate them.

This implies that a macro-state of a BEC can be pinned down exactly using only two quantities, just as in the case of an ideal gas. Rasmussen et al. [48] were able

to identify two isotherms (for $T = 0$ and $T \to \infty$) in the phase diagram $h(a)$, which separate the states of the condensate into three domains:

1. a forbidden one, where no physical states exist (region R_f of Figure 1.4);

2. a domain of positive temperature, which characterises most of the backgrounds which interact with large breathers (region R_p of Figure 1.4);

3. and a domain of negative absolute temperature. The domain of negative absolute temperatures is also the place where breathers form spontaneously [34] (region R_n of Figure 1.4). A domain of negative absolute temperatures implies a region within which the entropy does not increase monotonously with internal energy [49]. States at negative absolute temperatures evolve astronomically slow towards a state where several pinned breathers sit on top of a background at infinite temperature [34]. Like most dynamics involving breathers, this process is astronomically slow, similar to the coarsening process described in cosmology.

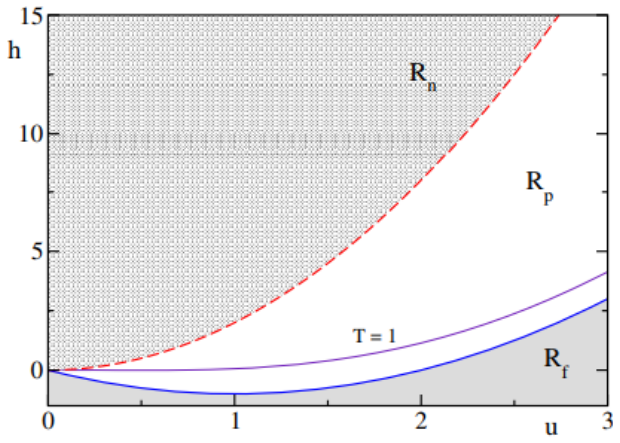

Figure 1.4: The three different domains for a Bose-Hubbard chain [49] - negative temperature states in the domain R_n, positive temperature states in the domain R_p. The diagram also depicts the infinite temperature isotherm (red dotted curve) and the ground state isotherm (solid blue curve). Everything below the ground state isotherm represents states which are not physical.

The fact that breathers are localised to a single site and have frequencies which are

so clearly distinct from those of the background can be used to build fast numerical algorithms, through the use of HMM. In addition to this, one can speed up the algorithm even further through the use of short lattices, where spatially extended backgrounds have been replaced with a Langevin heat bath [50]. These heat baths can either be characterised by either positive or infinite temperatures.

Breathers affect the dynamics of a BEC in peculiar ways, acting as either inhibitors of quantum transport (for pinned breathers) or as transport enhancers (for mobile breathers). In the paper by Iubini et al. [51], we see that if we put the two ends of a Bose-Hubbard chain at different temperatures, we will obtain a non-equilibrium stationary state. In this chain, the two thermostats are different, and the system will continuously transport heat and mass, from one end of the chain to the other. The system will never thermalise, and the temperature and chemical potential across the one-dimensional system will vary monotonously and continuously [52]. Only the ends of the chain will thermalise to the parameters of the bath, and every site in between will be involved in the coupled quantum transport. When a breather appears in the system, however, this whole dynamics changes dramatically [53]. When looking at the temperature throughout the system, we will see a large discontinuity where the breather sits. The left and the right sides will thermalise independently of the one bath they are in direct contact with. This suggests the fact that a pinned breather seems to break quantum transport across the lattice. The life-time of the breather is much larger than the thermalisation times for the two sides of the background (by orders of magnitude of 10^4 and beyond), therefore this insulator effect is very long-lived.

In a recent work of Mithun et al. [54], it is shown that pinned breathers weakly break the ergodicity of the system. The background phonon bath is essentially interrupted by the breathers, which act as insulators, and break the lattice into several puddles that thermalise independently of each other. The breathers seem to create one eigenvalue that is dominantly negative, effectively reducing the dimensionality of the phase space by one. If the breather sits at the end of a chain, the only direct result is a trajectory

that is confined within a subspace of dimension $D-1$, where D is the dimension of the original phase space, in the absence of breathers. If the breather sits anywhere else in the chain, however, this produces the partition of the phase space into a couple of weakly connected subspaces. These results are strongly compatible with other findings in this work which suggest that a breather acts as a local insulator, breaking the isometry of the lattice.

For quantum transport phenomena in Hamiltonian systems, there exists a rich literature which deals with the use of Discrete Truncated Wigner Approximations (DTWA) [55], which is a semi-classical analytical algorithm, and is supposed to outperform any mean-field theory approach, since it is a semi-classical theory which can describe quantum effects more accurately. The very essence of this algorithm, however is that in order for the system to be studied it has to either be ideally ergodic, or so strongly non-ergodic that it is basically split into several small subspaces which are to an extent, all independent from each other and locally ergodic. Unfortunately, the domain we work in is weakly non-ergodic, and is the only clear frame where the DTWA approach fails. This, once again, points us towards analytical descriptions which use the mean-field theory, without making the a priori assumption that the system will behave ergodically.

We can therefore deduce, that, within the laminar regime of the evolution, breathers are strongly disconnected from their surroundings. But, just as mentioned before, there are events during which excitations spontaneously formed by the background dramatically destabilise the breather and change the evolution abruptly. This is very similar to what was observed in [40] for trimers, using Peierls-Nabarro potentials. The breather seems to be stuck at the bottom of such a very deep valley, but once it interacts with an excitation which is tuned conveniently enough, it suddenly leaves the valley, and the shape of the Peierls-Nabarro hyper-surface suddenly changes altogether. A more thorough numerical study between breathers and large excitations will be developed in this thesis (see Chapter 3). A study of the resonances between breathers and phonon back-

grounds exists for Klein-Gordon chains [56], but no equivalent analysis was performed on Bose-Hubbard chains.

A different way to categorise breathers is to separate them according to their mobility

1. **Pinned breathers** have a fixed position, which does not change, unless they are strongly perturbed by their surroundings;

2. **Mobile breathers** propagate with an approximately constant velocity, and depending on their properties (height and width of the Gaussian wave-packet) can have different life times. They are generally smaller and shorter lived than pinned breathers.

Using this type of characterisation, we separate breathers into singularities which either block the transport of matter through the Bose-Hubbard chain, or enhance it dramatically, by propagating it through a solitonic wave, tsunami-like property of the DNLSE system. As we mentioned previously, our main focus is on pinned breathers, and most of the analytical and numerical tools presented in this work will revolve around them. What is interesting, however, is to study the interaction between these two types of breathers. One interaction picture which was taken from [57] -Figure 1.5- shows that when a mobile breather reaches a pinned breather, a very clean reflection occurs. This seems to suggest that pinned breathers can have the property of a perfectly reflective boundary. In the work of Rumpf, however [38], we see that large excitations are not always reflected, and sometimes very dramatic collisions occur. Here, we considered a large excitation in the background to be similar to a mobile breather. The question is, once again, when does the pinned soliton reflect large excitations and when does it interact with it. Or, to express this in terms of classical mechanics, when does the collision behave as elastic (where the excitation is assumed to hit a wall of very large mass and get reflected), and when does it behave as plastic (the excitation becomes absorbed in the 'wall' in the process). As we will later see in the work, phase differences

play a crucial role when settling this issue, because the energies of this system always contain terms which depend on the phase difference between nearest neighbours.

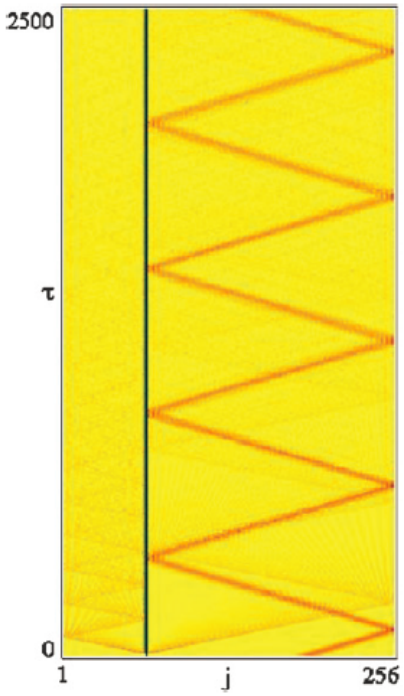

Figure 1.5: Amplitude profile of a Bose-Hubbard chain with two prominent breathers [57] - a pinned one depicted by dark blue, and a mobile breather on the right of the pinned one. The pinned breather seems to act as a reflective boundary. In the work done by Franzosi et al. [57], they show that the mobile breather suffers dissipations at site $j = 256$, where there is a loss, but no dissipations at all when it meets the pinned breather.

The highly stable nature of pinned breathers, together with the fast dynamics they are characterised by, makes the numerical study of DNLSE lattices highly challenging. During the lifetime of a breather, we must use time steps which are small enough to accommodate its large frequency. Given the fact that these life times are astronomical [8], and that the time step is very small, one can immediately guess the highly problematic nature of these systems. Coarsening phenomena are described by very slow relaxation towards a meta-stable state. In this sense, the evolution of a BEC is similar to that used in numerical simulations of cosmological phenomena, where the background starts as relatively homogeneous, and as time passes, any small fluctuation grows until very

stable structures form, and the overall appearance of the system changes dramatically, most of the matter being concentrated into several distinct points. At this stage, the dynamics slows down dramatically, and only very rare collisions between these structures that formed spontaneously from the initial fluctuations [49]. For a BEC, this final state is the state that Rumpf described, and consists of pinned breathers on top of an infinite temperature background [34].

The DNLSE lattice consists of N coupled oscillators, with different frequencies. In this sense, one can look at studies of the solar system [58], to see how the fast frequencies can be eliminated, to create fast numerical techniques. In this astronomy case, one starts with the assumption that the orbits of all planets are perfectly elliptical and obey Kepler's law in the first approximation. One also takes the Sun as the centre of this system of coordinates. The smallness parameter will be defined by the fastest frequency in the system, i.e. that of Mercury. As higher order corrections are introduced in the system, one must also take into account that the location of the Sun is also changing with time. However, if we assume that initially the Sun is situated in the origin, we must trace its trajectory using Cartesian coordinates, since talking about the phase of a point mass next to the origin is problematic, since there are discontinuities when the point mass crosses the origin. In any perturbative calculation, we must first make sure that all coordinates are continuous and differentiable. Therefore, we must avoid using the phase as a coordinate when a certain body will find itself in the vicinity of the origin.

The case of pinned breathers is very similar to that of which was described in the previous paragraph, with the exception that there is only one oscillator, and several other bodies with very small frequencies. In a sense, if we plot all the wave-functions of all N sites in the lattice, we will obtain that most of them will be concentrated next to the origin, and only one wave-function orbits in an almost circular trajectory far away from the origin (here we made the assumption that there is a single pinned breather in the system). In this sense, the study is complementary to that of the Solar

System. Here only one 'body' is described by polar coordinates, while all the others are described by Cartesian coordinates, due to their proximity to the origin. This system is also more complex than the Solar System, since the masses of all N bodies are not time independent. The difficulties, advantages and disadvantages of applying perturbative techniques on the evolution of BECs will be detailed later throughout this thesis.

1.3 The structure of the thesis

Extensive descriptions of all the established numerical techniques used throughout the project are provided in Chapter 2, together with a description of known properties of breathers in computational simulations. Thereafter, a review of extreme events (astronomically rare situations during which pinned breathers abruptly change size or location) is provided in Chapter 3.

In the case of systems with multiple scales, it is sometimes useful to separate an axis into two or more independent variables [59] - this can be done for both lengths and times. Any derivative will be transformed into a superposition of partial differential operators of the sort

$$d_t = \partial_{t_1} + \varepsilon \partial_{t_2} \tag{1.45}$$

where now t_1 and t_2 are orthogonal axes. In this sense, the dimension of the phase space is artificially increased by 1. However, this can simplify the calculations drastically, allowing partial averaging over one of the time-scales. Naturally, the identity (1.45) will transform any system of coupled differential equations into a system of partial coupled differential equations. In the case of systems with pinned breathers, we are dealing with three time scales

1. That introduced by the fast rotation of the breather
2. That associated with the slow evolution of the background

3. That associated with the astronomically slow decay of breathers

It follows from here that one might be able to describe the analytics of the DNLSE using multiple scale techniques, together with asymptotic expansion strategies. In systems with multiple time scales, using one single differential operator for time (i.e. d_t instead of ∂_{t_1} and ∂_{t_2}) results in approximations which are valid only locally, and lose their validity very rapidly when t increases beyond values of order $\mathcal{O}(\varepsilon)$. Substitution (1.45) allows the construction of a system of partial differential equations, which can be closed by imposing solvability conditions. These conditions ensure that for an isolated system, the total energy and mass of the chain are conserved, and that there are no divergences.

It is worth mentioning that the method of multiple time scales is usually applied analytically to functions with one single variable. Here we are dealing with N coupled oscillators, and therefore we expect the technique to become more challenging. In addition to this, our system must conserve mass simultaneously as it conserves Hamiltonian.

Because one of the time scales originates from fast oscillations, one can immediately think of averaging. Averaging operations are more elegant when multiple scales are used, since the slower time scale can be treated as a constant (slow times are orthogonal to fast ones) for the fast time operators (both for integration and derivation). The multiple time scale perturbation expansion for pinned breathers is presented in Chapter 4.

We will show, however that averaging techniques can also be performed without introducing multiple time scales. Once the averaging procedure is completed, one has eliminated all the fast frequencies of the system, and a large time step can be used to perform rapidly converging numerical integrations.

During the laminar flow of the condensate, the breather norm is almost unchanged. This type of behaviour for Hamiltonian systems is characteristic of that of an adiabatic invariant [60]. An adiabatic invariant is a quantity which changes very little during the evolution of a system, and is effectively frozen, unless when moving through phase

space it encounters a resonant hyper-surface. We will later see that, in our system, this translates into a collision between the breather and a resonating excitation (i.e. with a frequency of ω/n, where ω is the frequency of the breather, and $n \in \mathbb{N}$). Using asymptotic expansions, one can eliminate some of the fast fluctuating terms in the breather norm, arriving at a more accurate expression of the adiabatic invariant.

In the laminar regime, averaging is possible through perturbative techniques. Once the Average Nonlinear Schrödinger Equation (AvNLSE) is built, it can then be used to construct an Effective Hamiltonian, which will approximate the trajectories generated by the DNLSE. This Effective Hamiltonian is built in a way which guarantees the conservation of the condensate mass, just as in the case of the initial Bose Hubbard model. The Effective Hamiltonian alone does not suffice to generate realistic trajectories for the breathers, since it does not allow them to decay. In addition, this Hamiltonian artificially enhances the stability of the breather, keeping it pinned, even in the presence of very large perturbations.

This work also investigates how sudden changes in the breather shape are either caused by the spontaneous appearance of a bound state, which originates from the crossing of a well known separatrix in the dynamics of dimers [44], or from resonances between breathers and their backgrounds. These resonances will be the leading cause for the breakdown of the applicability of averaging.

The breather norm acts as an adiabatic invariant, and according to [61], can change dramatically when the state encounters a hyper-resonant surface. The validity of this affirmation is confirmed both numerically and analytically later in this work. The averaging techniques and the existence of an adiabatic invariant are presented in Chapter 5.

Ultimately, we build a Hybrid Integration Scheme, which can approximate the trajectories of breathers up to their complete decay. This algorithm speeds up numerical simulations by making use of much larger time steps than a classical Runge-Kutta approach. Hybrid integration schemes abound in literature under the name of Heteroge-

neous Multiscale Methods [62–64]. They mostly consist of building a macro-integrator (in this case an averaged differential equation) which is very fast to integrate in comparison to the existing micro-integrator (which here is the full DNLSE). Additionally, one identifies domains in which the macro-integrator fails, due to either singularities or topological aberrations and then builds a transition mechanism from one integrator to the another which allows fast approximations of non-linear systems. In the case of fast-slow Hamiltonian systems, macro-integrators fails due to the inapplicability of averaging in the presence of resonances [61].

In the last part of this work (see Chapter 6), we probe that the Hybrid Integration Scheme works remarkably well, producing results which are very similar to what the full DNLSE has to offer, but over much shorter times. For both algorithms, the lifetimes of the breathers increase exponentially as their initial mass is increased, and, more remarkably, the two regression lines obey very similar equations.

The Hybrid Integration scheme is ultimately extended to systems with multiple breathers and to lattices of generic temperature and chemical potential as a strong investigative tool which can generate fast numerical solution for a broad family of nonlinear problems.

Chapter 2

Numerical Methods and Numerical Simulations of the DNLSE

2.1 Presentation of Numerical Methods

2.1.1 State Initialisation

One-dimensional Bose-Hubbard lattices are characterised by phase diagrams with two control parameters. It is therefore convenient to define states with the help of two intensive variables: amplitude density, defined as the average number of atoms per site, and denoted by the symbol a, and Hamiltonian density, defined as the linear energy density, and denoted by h. The initial state of any simulation will be described by a dot on the phase diagram $h(a)$. Like in any thermodynamic system at equilibrium, these parameters only denote a macroscopic state without capturing all the information of the instantaneous wave function.

The amplitude density is formally defined as:

$$a \equiv \frac{1}{2N} \sum_{j=1}^{N} \left(p_j^2 + q_j^2 \right) \tag{2.1}$$

Meanwhile, the density of the Bose-Hubbard Hamiltonian is:

$$h \equiv \frac{1}{4N} \sum_{j=1}^{N} \left(p_j^2 + q_j^2 \right)^2 + \frac{1}{N} \sum_{j=1}^{N-1} \left(p_j p_{j+1} + q_j q_{j+1} \right) \tag{2.2}$$

Let us assume that one is interested in a initial state which is described by the pair $\{a_0, h_0\}$ on the phase diagram. One can now generate $2N$ random numbers which constitute a 'guess state' by creating:

- N randomly generated amplitudes in the interval $[0, 2a_0]$. As long as the probability density of the random variables is constant (i.e. $\frac{1}{2a_0}$), the average amplitude will automatically fall in the vicinity of a_0, in perfect agreement with what was required.

- N randomly generated phases in the interval $[0, 2\pi]$, which will constitute the phases of the initial wave-function. Since the values here are random, the 'guess state' will most likely have an energy density significantly different from what one initially wanted.

At this moment, it is useful to calculate the two densities defined in 2.1 and 2.2 for the guess state, and determine how far the initialisation point $\{a_{guess}, h_{guess}\}$ sits from the desired state $\{a_0, h_0\}$.

One can now design a Monte Carlo algorithm which iteratively approaches the desired state until a threshold precision is reached (the required precision is specified by the user through the introduction of a smallness parameter η). For example, for most numerics, being within the vicinity of $\{a_0, h_0\}$ with tolerance of $\eta = 10^{-8}$ was considered satisfactory.

The Monte Carlo algorithm is implemented in the following way:

- Start with a guess state $\psi = \{q_{j=\overline{1,N}}, p_{j=\overline{1,N}}\}$, which has known parameters a and h.

- Go to a random site of the lattice $j \in \{1, 2, 3, ..., N\}$.

- Change the wave-function at the chosen site from z_j to $\tilde{z}_j = z_j + \rho \exp(i\theta)$, where θ is a random phase and ρ is a randomly generated variable in the interval $[0, \frac{|z_j|}{\kappa}]$. The parameter κ is initially chosen to be 10 but is increased as the state approaches the desired coordinates $\{a_0, h_0\}$.

- Instead of evaluating the new norm and Hamiltonian of the modified state using the full expressions from 2.1 and 2.2, it is far more efficient to only look at the changes of these two variables, which will be given by

$$\Delta a = \frac{\left(\tilde{p}_j^2 + \tilde{q}_j^2\right) - \left(p_j^2 + q_j^2\right)}{2N} \tag{2.3}$$

$$\begin{aligned} \Delta h = & \frac{\left(\tilde{p}_j^2 + \tilde{q}_j^2\right)^2 - \left(p_j^2 + q_j^2\right)^2}{4N} + \\ & + \frac{\left(\tilde{p}_j - p_j\right)\left(p_{j-1} + p_{j+1}\right)}{N} \\ & + \frac{\left(\tilde{q}_j - q_j\right)\left(q_{j-1} + q_{j+1}\right)}{N}. \end{aligned} \tag{2.4}$$

- Check whether the new state is closer to the desired coordinates, by verifying if it satisfies:

$$\left[a_0 - (a + \Delta a)\right]^2 + \left[h_0 - (h + \Delta h)\right]^2 < (a_0 - a)^2 + (h_0 - h)^2. \tag{2.5}$$

  If this is satisfied, then accept the trial state as the new ψ and update a to $a + \Delta a$ and h to $h + \Delta h$. Otherwise, reject the trial state and keep ψ unchanged.

- Repeat the algorithm until arriving to final values of a and h which are within the threshold distance η (which is usually set to 10^{-8} in the numerics) from the desired state $\{a_0, h_0\}$.

Once the initialisation algorithm is completed, it is useful to let the system evolve in a micro-canonical set-up, to allow thermalisation. This can be done using either a symplectic integrator, like that developed by H. Yoshida [28], or through the use of a fourth-order Runge-Kutta integrator (the standard integrator employed throughout most of the work presented in this project). The thermalisation times are of the order 10^3 time units; therefore evolving the system for $\approx 2,000$ units should suffice.

Note: For lattices with Periodic Boundary Conditions (PBC) the state initialisation algorithm is very similar, but the Hamiltonian density has a different definition from 2.2, containing an additional hopping (tunnelling) between sites $j = 1$ and $j = N$. Once the initial Hamiltonian is defined to include this extra hopping term, no additional changes are required in the algorithm.

2.1.2 Langevin Heat Baths. Grand-Canonical Set-ups

One-dimensional Bose-Hubbard lattices can be put into contact with thermostats through the use of stochastic Langevin Equations. The environment can be modelled with the help of two families of complex harmonic oscillators of frequencies ω_ν^a and ω_ν^b and amplitudes $|a_\nu|^2$ and $|b_\nu|^2$. The condensate of wave-function z is coupled to the environment through the transfer coefficients K_ν. The Hamiltonian and norm under which the coupling evolves are given by [50]

$$H_C = \sum_\nu \{\omega_\nu^a |a_\nu|^2 + \omega_\nu^b |b_\nu|^2 + \left[K_\nu^* z(a_\nu^* + b_\nu) + \text{c.c.}\right]\}, \tag{2.6}$$

$$A_C = \sum_\nu \{|a_\nu|^2 - |b_\nu|^2\}. \tag{2.7}$$

Under this construction, ia_ν^* and a_ν are conjugate canonical (Darboux) coordinates, and so are ib_ν^* and b_ν. After imposing norm conservation, i.e. $A_C(t) + |z(t)|^2 = A_C(0) + |z(0)|^2$, one can use the Hamiltonian equations of motion. Writing the equations

of motion will lead to

$$i\dot{z} = f(z) - \int_0^t G(t-s)z(s)ds + F(t), \tag{2.8}$$

where $f(z)$ is the deterministic part of the evolution, which is not included into the expression of H_C. G characterises the dissipation and is defined as

$$G(t) = \sum_\nu |K_\nu|^2[\exp(i\omega_\nu^a t) - \exp(i\omega_\nu^b t)]. \tag{2.9}$$

F describes the noise and is given by the expression

$$F(t) = -\sum_\nu K_\nu[a_\nu(0)\exp(i\omega_\nu^a t) + b_\nu^*(0)\exp(i\omega_\nu^b t)]. \tag{2.10}$$

In the thermodynamic limit, the sums from (2.9) can be replaced with integrals, changing the expression of the dissipation to

$$G(t) = \int_\mu^\infty d\omega G^a(\omega)\exp(i\omega t) - \int_{-\mu}^\infty d\omega G^b(\omega)\exp(-i\omega t). \tag{2.11}$$

Iubini et al. [50] have chosen $G^a(\omega) = \frac{\gamma}{2\pi}(\omega - \mu)$ and $G^b(\omega) = \frac{\gamma}{2\pi}(\omega + \mu)$. According to Ref. [50], this is the simplest example which produced a non-singular spectral density $F(t)$.

Assuming grand-canonical distributions for the heat bath oscillators, i.e. a Boltzmann distribution of the sort $P \sim \exp\big[-\beta(H_B - \mu A_B)\big]$, one arrives to the following fluctuation-dissipation relations

$$\langle F(t)F(t')\rangle = \langle F^*(t)F^*(t')\rangle = 0, \tag{2.12}$$

$$\langle F(t)F^*(t')\rangle = \frac{\gamma}{\beta}\delta(t-t'). \tag{2.13}$$

Ultimately, the differential equation can be written as

$$i\dot{z} = (1 + i\gamma)f(z) + i\gamma\mu z + F(t). \tag{2.14}$$

Positive Temperature Heat Baths

For reservoirs with positive temperature, the differential equation from (2.14) becomes:

$$i\dot{z}_n = (1 + i\gamma)\big[-2|z_n|^2 z_n - z_{n-1} - z_{n+1}\big] + i\gamma\mu z_n + \sqrt{\gamma T}\xi_n(t) \tag{2.15}$$

where $\xi_n(t) = \xi_n^R(t) + i\xi_n^I(t)$ is complex white Gaussian noise and γ is the coupling strength (set equal to 1 during most simulations).

The numerical integrator of this system is written in the following way:

1. For a time step of Δt, evolve the system using a 4^{th} order Runge-Kutta integrator with the following derivatives:

   - For the wave-function at site 1:

     $$\dot{x}_1 = -2(x_1^2 + y_1^2)y_1 - y_2 - 2\gamma_L(x_1^2 + y_1^2)x_1 - \gamma_L x_2 + \gamma_L\mu_L x_1$$
     $$\dot{y}_1 = 2(x_1^2 + y_1^2)x_1 + x_2 - 2\gamma_L(x_1^2 + y_1^2)y_1 - \gamma_L y_2 + \gamma_L\mu_L y_1$$

     where γ_L is the loss rate at the left end and μ_L is the chemical potential of the heat bath on the left.

   - For the wave-function at site j:

     $$\dot{x}_j = -2(x_j^2 + y_j^2)y_j - y_{j-1} - y_{j+1}$$
     $$\dot{y}_j = 2(x_j^2 + y_j^2)x_j + x_{j-1} + x_{j+1}$$

- For the wave-function at site N:

$$\begin{aligned}\dot{x}_N &= -2(x_N^2+y_N^2)y_N - y_{N-1} - \\ &\quad -2\gamma_R(x_N^2+y_N^2)x_N - \gamma_R x_{N-1} + \gamma_R\mu_R x_N \\ \dot{y}_N &= 2(x_N^2+y_N^2)x_N + x_{N-1} - \\ &\quad -2\gamma_R(x_N^2+y_N^2)y_N - \gamma_R y_{N-1} + \gamma_R\mu_R y_N\end{aligned}$$

  where γ_R is the loss rate at the right end and μ_R is the chemical potential of the heat bath on the right.

2. Generate complex white Gaussian noise with variance equal to one for both ends of the lattice. After letting the system evolve from $\psi_i \equiv \psi(t_0)$ to $\psi_f \equiv \psi(t_0+\Delta t)$ under the equations of motion written above, add the stochastic terms as:

   - For the left end the incrementation is:

$$\begin{aligned}x_1 &\mapsto x_1 + \xi_L^I\sqrt{\gamma_L T_L \Delta t} \\ y_1 &\mapsto y_1 - \xi_L^R\sqrt{\gamma_L T_L \Delta t}\end{aligned}$$

     where T_L is the temperature of the left heat bath.

   - For the right end the incrementation is:

$$\begin{aligned}x_N &\mapsto x_N + \xi_R^I\sqrt{\gamma_R T_R \Delta t} \\ y_N &\mapsto y_N - \xi_R^R\sqrt{\gamma_R T_R \Delta t}\end{aligned}$$

     where T_R is the temperature of the right heat bath.

Note: The system can be decoupled from any (or both) of the heat baths simply by setting the loss rates to zero (i.e. $\gamma_L = 0 \vee \gamma_R = 0$).

Infinite Temperature Heat Baths

In the case of infinite-temperature heat baths, for finite amplitude and Hamiltonian densities, one must also impose $\gamma \to 0$ and $\mu \to -\infty$. The quantities $\Gamma \equiv -\gamma\mu$ and $a \equiv -\frac{T}{\mu}$ are finite, transforming the Langevin Equation from 2.14 into:

$$i\dot{z}_n = -2|z_n|^2 z_n - z_{n-1} - z_{n+1} - i\Gamma z_n + \sqrt{a\Gamma}\xi_n(t) \tag{2.16}$$

where $\xi_n(t) = \xi_n^R(t) + i\xi_n^I(t)$ is complex white Gaussian noise and γ is the coupling strength (set equal to 1 during most simulations).

The numerical integrator from above is modified to:

1. For a time step of Δt, evolve the system using a 4^{th} order Runge-Kutta integrator with the following derivatives:

   - For the wave-function at site 1:

     $$\dot{x}_1 = -2(x_1^2 + y_1^2)y_1 - y_2 - \Gamma_L x_1$$
     $$\dot{y}_1 = 2(x_1^2 + y_1^2)x_1 + x_2 - \Gamma_L y_1$$

     where Γ_L acts as the new loss rate at the left end of the one-dimensional lattice.

   - For the wave-function at site j:

     $$\dot{x}_j = -2(x_j^2 + y_j^2)y_j - y_{j-1} - y_{j+1}$$
     $$\dot{y}_j = 2(x_j^2 + y_j^2)x_j + x_{j-1} + x_{j+1}$$

   - For the wave-function at site N:

     $$\dot{x}_N = -2(x_N^2 + y_N^2)y_N - y_{N-1} - \Gamma_R x_N$$
     $$\dot{y}_N = 2(x_N^2 + y_N^2)x_N + x_{N-1} - \Gamma_R y_N$$

     where Γ_R is the loss rate at the right end.

2. Generate complex white Gaussian noise with variance equal to one for both ends of the lattice. After letting the system evolve from $\psi_i \equiv \psi(t_0)$ to $\psi_f \equiv \psi(t_0 + \Delta t)$ under the equations of motion written above, add the stochastic terms as:

   - For the left end the incrementation is:

$$x_1 \mapsto x_1 + \xi_L^I \sqrt{\Gamma_L a_L \Delta t}$$
$$y_1 \mapsto y_1 - \xi_L^R \sqrt{\Gamma_L a_L \Delta t}$$

     where a_L is the amplitude density induced by the left heat bath.

   - For the right end the incrementation is:

$$x_N \mapsto x_N + \xi_R^I \sqrt{\Gamma_R a_R \Delta t}$$
$$y_N \mapsto y_N - \xi_R^R \sqrt{\Gamma_R a_R \Delta t}$$

     where a_R is the amplitude density induced by the right heat bath.

2.1.3 Numerical Evaluation of Thermal Parameters

The thermodynamic entropy can be employed to evaluate the temperature and the chemical potential of the system. For the Bose-Hubbard chain, in the case of a micro-canonical set-up, the entropy is proportional to the logarithm of the volume of a hyper-surface characterised by a given mass and energy (the sub-set of the phase space which consists of all possible configurations of a given energy H and fixed mass A). One can now use the analytical dependency of the entropy of the two conserved quantities of the system: mass (A) and Hamiltonian (H), to write the expressions

$$\frac{1}{T} = \frac{\partial S}{\partial H} \qquad \frac{\mu}{T} = -\frac{\partial S}{\partial A}. \tag{2.17}$$

The work done by Franzosi in [47] addresses time-independent Hamiltonian systems with one additional conserved quantity. He proves that the temperature and the higher order derivatives of the entropy are micro-canonical observables, which un-

der the assumption of ergodicity can be calculated as time averages. Therefore, the partial derivatives on the right hand side of equation (2.17) can be evaluated using expressions [51]

$$\frac{\partial S}{\partial C_j} = \left\langle \frac{W||\vec{\xi}_j||}{\vec{\nabla}C_j \cdot \vec{\xi}_j} \ \vec{\nabla} \cdot \left(\frac{\vec{\xi}_j}{W||\vec{\xi}_j||} \right) \right\rangle, \tag{2.18}$$

where $C_1 = A$ and $C_2 = H$ are the conserved quantities of the system and W, ξ_j are defined as:

$$\vec{\xi}_j \equiv \frac{\vec{\nabla}C_j}{||\vec{\nabla}C_j||} - \frac{(\vec{\nabla}C_j \cdot \vec{\nabla}C_{k\neq j})\vec{\nabla}C_{k\neq j}}{||\vec{\nabla}C_j|| \ ||\vec{\nabla}C_{k\neq j}||^2} \tag{2.19}$$

$$W^2 \equiv \sum_{\substack{j,k=1 \\ j<k}}^{2N} \left[\frac{\partial C_1}{\partial x_j}\frac{\partial C_2}{\partial x_k} - \frac{\partial C_1}{\partial x_k}\frac{\partial C_2}{\partial x_j} \right]^2 \tag{2.20}$$

where x_j are coordinates in the phase space related to those in the Bose-Hubbard Hamiltonian from (2.2) through:

$$\begin{aligned} x_{2j} &= q_j \\ x_{2j+1} &= p_j. \end{aligned} \tag{2.21}$$

The numerical algorithm for evaluating the expressions from (2.17) using the averages defined at (2.18) is presented below.

Function for the Numerical Evaluation of Divergences and of W^2

One starts by writing a function which takes as an input the state of the system given by the array $\{x_j\}$:

1. Evaluate the directions of the divergence of the mass ($\vec{\nabla}A/||\vec{\nabla}A||$) and of the Hamiltonian ($\vec{\nabla}H/||\vec{\nabla}H||$) for a given state $\{x_j\}$:
   - Evaluate the numerical values of $\partial_{x_j}A$ and $\partial_{x_j}H$ for all $j \in \{1, ..., 2D\}$ and during this process build the arrays $\vec{\nabla}A$ and $\vec{\nabla}H$.
   - During the same process increment the sums $||\vec{\nabla}A|| \equiv \sum(\partial_{x_j}A)^2$ and $||\vec{\nabla}H|| \equiv \sum(\partial_{x_j}H)^2$.

- Normalise the divergences by dividing them by the norms evaluated above.

2. Increment the quantity defined at (2.20) using the divergences calculated at the previous step using two nested `for` loops.

3. Once, again use the previously calculated divergences to evaluate $\vec{\nabla}A \cdot \vec{\nabla}H$.

4. Use one single `for` loop to evaluate in one go $\vec{\xi_1}$, $\vec{\xi_2}$, $||\vec{\xi_1}||$ and $||\vec{\xi_2}||$. From this, immediately evaluate the directions $\hat{\xi} \equiv \vec{\xi}/||\vec{\xi}||$

5. Use one single `for` loop to evaluate in one go $\vec{\nabla}C_1 \cdot \vec{\xi_1}$ and $\vec{\nabla}C_2 \cdot \vec{\xi_2}$.

The function takes the state of a Bose-Hubbard Chain $\psi = \{q_{j=\overline{1,N}}, p_{j=\overline{1,N}}\}$ and returns five outputs: $\hat{\xi}_1$, $\vec{\nabla}C_1 \cdot \vec{\xi_1}$, $\hat{\xi}_2$, $\vec{\nabla}C_2 \cdot \vec{\xi_2}$ and the quantity W.

Employing the function to evaluate the Temperature and the Chemical Potential

The temperature and the chemical potential can now be evaluated employing formula (2.18) on the outputs of the function described in the previous subsection (i.e. on $\hat{\xi}_1$, $\vec{\nabla}C_1 \cdot \vec{\xi_1}$, $\hat{\xi}_2$, $\vec{\nabla}C_2 \cdot \vec{\xi_2}$ and W) to obtain the numerical values of $\partial S/\partial A$ and $\partial S/\partial H$. Since these two numbers correspond to $1/T$ and $-\mu/T$, one can ultimately calculate the temperature and the chemical potential of the chain.

If the chain contains Langevin heat baths or dissipative terms, it is advised to omit at least the last two sites at the chain end when sending the input state ψ. This is done not to take into account any statistical aberrations induced by the open ends of the chain. Similarly, if a large breather is present in the chain, and one wants to evaluate the thermodynamic parameters of its surroundings (i.e. of the background) one should also omit the nearest neighbours of the breather. This is done in order not to take into account the influence of the fast harmonics introduced by the breather.

It is now convenient to introduce the notation $\hat{\xi} \equiv \vec{\xi}/||\vec{\xi}||$ and re-write (2.18) as:

$$\frac{\partial S}{\partial C_j} = \left\langle \frac{W}{\vec{\nabla} C_j \cdot \hat{\xi}_j} \ \vec{\nabla} \cdot \left(\frac{\hat{\xi}_j}{W} \right) \right\rangle \tag{2.22}$$

Using the definition of divergence, one can evaluate:

$$\vec{\nabla} \cdot \left(\frac{\hat{\xi}_j}{W} \right) = \sum_{k=1}^{2N} \frac{\partial}{\partial x_k} \left(\frac{\xi_{j,k}}{W} \right) \tag{2.23}$$

$$\vec{\nabla} \cdot \left(\frac{\hat{\xi}_j}{W} \right) = \sum_{k=1}^{2N} \frac{\partial_{x_k} \xi_{j,k} W - \xi_{j,k} \partial_{x_k} W}{W^2}. \tag{2.24}$$

Introducing this formulation into (2.22), one immediately arrives to:

$$\frac{\partial S}{\partial C_j} = \left\langle \frac{W}{\vec{\nabla} C_j \cdot \hat{\xi}_j} \ \sum_{k=1}^{2N} \frac{\partial_{x_k} \xi_{j,k} W - \xi_{j,k} \partial_{x_k} W}{W^2} \right\rangle. \tag{2.25}$$

And this can be further simplified to:

$$\frac{\partial S}{\partial C_j} = \left\langle \frac{1}{\vec{\nabla} C_j \cdot \hat{\xi}_j} \ \sum_{k=1}^{2N} \left(\partial_{x_k} \xi_{j,k} - \frac{\xi_{j,k} \partial_{x_k} W}{W} \right) \right\rangle. \tag{2.26}$$

This implies that, in order to evaluate the temperature and the chemical potential, one must also know the numerical values of two sums: $\sum_{k=1}^{2N} \left(\partial_{x_k} \xi_{1,k} - \frac{\xi_{1,k} \partial_{x_k} W}{W} \right)$ and $\sum_{k=1}^{2N} \left(\partial_{x_k} \xi_{2,k} - \frac{\xi_{2,k} \partial_{x_k} W}{W} \right)$. In order to do this, one must:

1. Evaluate $\hat{\xi}_1$, $\vec{\nabla} C_1 \cdot \vec{\xi}_1$, $\hat{\xi}_2$, $\vec{\nabla} C_2 \cdot \vec{\xi}_2$ and W for the state of interest $\psi = \{q_{j=\overline{s,e}}, p_{j=\overline{s,e}}\}$. Where $j = s$ is the location of the first site and $j = e$ is the location of the last site taken for this portion of the chain. It is recommended to take chains with lengths of at least five sites when evaluating the thermal parameters.

2. Write a `for` loop where each coordinate of the state is changed by a small increment η, i.e. $x_j \to x_j + \eta$. This loop will have $2 \times (e - s + 1)$ iterations.

    - After each one of these incremental modifications of the state of interest

re-evaluate $\hat{\xi}_1$, $\hat{\xi}_2$ and W.

- While going through the loop evaluate the partial derivatives in (2.26) through the following approximations

$$\begin{aligned} \partial_{x_k}\xi_{1,k} &\approx \Delta\xi_{1,k}/\eta \\ \partial_{x_k}\xi_{2,k} &\approx \Delta\xi_{2,k}/\eta \\ \xi_{1,k}\partial_{x_k}W &\approx \xi_{1,k}\Delta W/\eta \\ \xi_{2,k}\partial_{x_k}W &\approx \xi_{2,k}\Delta W/\eta. \end{aligned} \tag{2.27}$$

- At each step of the `for` loop increment $S_1 \equiv \sum\left(\partial_{x_k}\xi_{1,k} - \frac{\xi_{1,k}\partial_{x_k}W}{W}\right)$ and $S_2 \equiv \sum\left(\partial_{x_k}\xi_{2,k} - \frac{\xi_{2,k}\partial_{x_k}W}{W}\right)$ using the approximations above.

3. After exiting the `for` loop evaluate

$$T = \frac{\vec{\nabla}C_1\cdot\vec{\xi}_1}{S_1} \qquad \mu = -T \times \frac{S_2}{\vec{\nabla}C_2\cdot\vec{\xi}_2}, \tag{2.28}$$

which are the thermal parameters that were required.

The temperature and the chemical potential of the chain are global quantities, and calculating them involves all the variables in the state vector $\psi = \{q_{j=\overline{1,N}}, p_{j=\overline{1,N}}\}$. However, it was shown numerically in [51] that these definitions also work when restricted to sub-chains. The definitions provided by Eq. (2.28) have been developed for micro-canonical ensembles, but will ultimately be generalised to open Bose-Hubbard chains.

2.1.4 Calibration of states with phase diagrams in literature

At this stage, it is appropriate to explain how to test whether the written codes are properly calibrated, by comparing numerical findings with the literature. One such work is the paper [50] which simulates one-dimensional Bose-Hubbard chains in the presence of heat baths at positive temperature. Like in the paper, the initial condition

was given by a clear macroscopic state specified by one point on the phase diagram given by $a = 4$ and $h = 15$. This point lies beneath the infinite temperature isotherm ($h_\infty(a) = 2a^2$) and therefore is characterised by a positive temperature. The two Langevin heat baths are set just as in the paper at $T = 1$ and $\mu = 2$. The initial state is set through the method presented in Section 2.1.1 and the Langevin heat baths are build using the algorithm presented in Section 2.1.2.

The numerical test was performed using a lattice with $N = 127$ sites. This number is of the form $2^m - 1$, allowing fast implementations of Yoshida symplectic integrators (these integrators are only used for the initial thermalisation, since they are restricted to micro-canonical regimes). These integrators are used to thermalise a state, once it has been initialised through the method described in Section 2.1.1. After the state was thermalised, it was allowed to evolve for $t = 5000$ time units, similarly to what was done in [50]. During this time, the temperature and the chemical potential have been evaluated numerically using the techniques introduced in Section 2.1.3, by using Eqs. (2.28). Figures 2.1, 2.2 and 2.3 monitor how the mass distribution and the thermal parameters vary with time.

These findings are perfectly consistent with those presented in Ref. [50]. The thermalisation time here is slightly longer, but this is to be expected, since this lattice is almost double the length of that in Ref. [50]. One can therefore conclude that the state initialisation, the calibration of the heat baths and the numerical evaluation of the thermal parameters have been properly defined and proceed towards the characterisation of breathers using these numerical tools.

2.1.5 State saving/loading

When studying the dynamics of breathers, one can easily run simulations which cover time-spans of 10^7 time units and beyond. When starting a simulation, it is impossible to know beforehand the exact times at which remarkable events will occur. It is entirely possible that even during a simulation with a large pre-settled integration

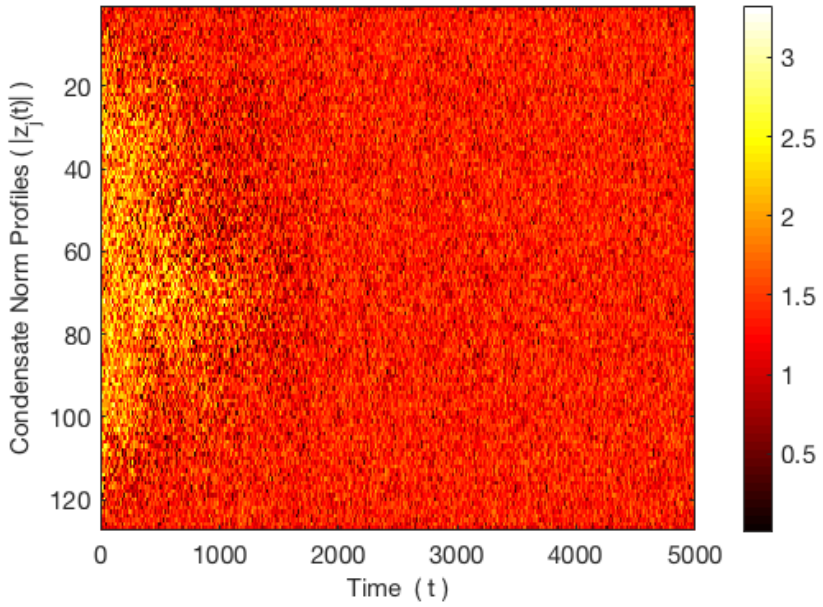

Figure 2.1: Vertical axis: $|z_n|$ for each of the 127 sites; Horizontal axis: Time. After a certain thermalisation time of order $\mathcal{O}(1000)$, all sites obey the same statistics. This happens due to the action of the heat baths.

time (i.e. 5×10^6), nothing remarkable happens to the breather. In this case, the user might be interested in continuing the simulation, even beyond the initial integration time which was specified at the beginning of the code.

It is therefore useful to have a block of code with the function of saving the final state. This state can later be used as the initial state of a future simulation and the starting time will no longer be set to zero, but to whatever point the previous simulation was interrupted.

A similar block of code can be called routinely during the simulation, re-writing the wave-function at every 10^4 time units or so. This data will be only used in the unlikely event of a hardware failure, allowing one to continue simulations which have been interrupted abruptly by events which are not controlled by the user.

There are several deeper conceptual issues here, which are not obvious at first sight:

- When saving the wave-function to a `.txt` file, one truncates all real numbers to a

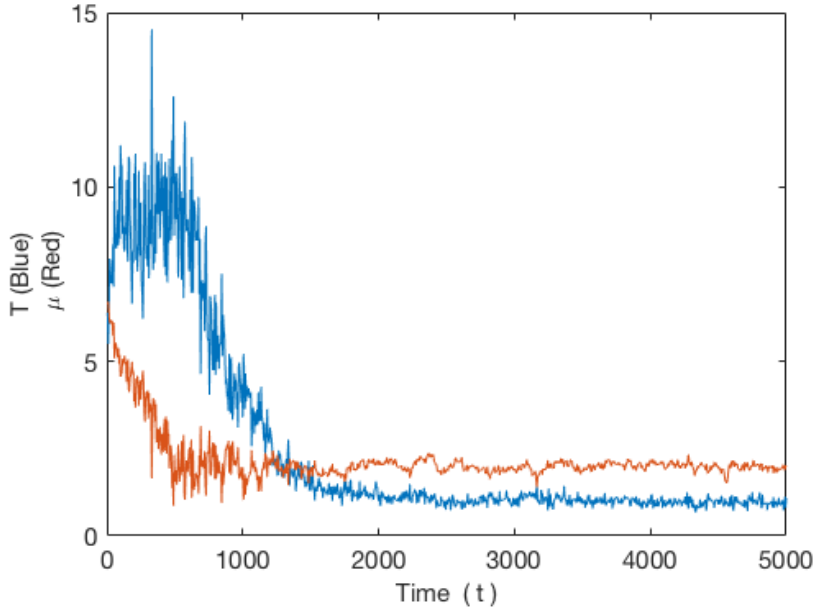

Figure 2.2: Thermodynamic parameters as a function of time. After the thermalisation is complete, the system stabilises at $T = 1$ and $\mu = 2$, which are exactly the parameters of the heat baths. The shape of the transition curves have the same general behaviour as the ones obtained in `Figure 2` of Ref. [50]. The transition is slightly slower here, since we have used a chain of 127 sites, while the authors used a smaller site, of 100 sites, which will thermalise faster.

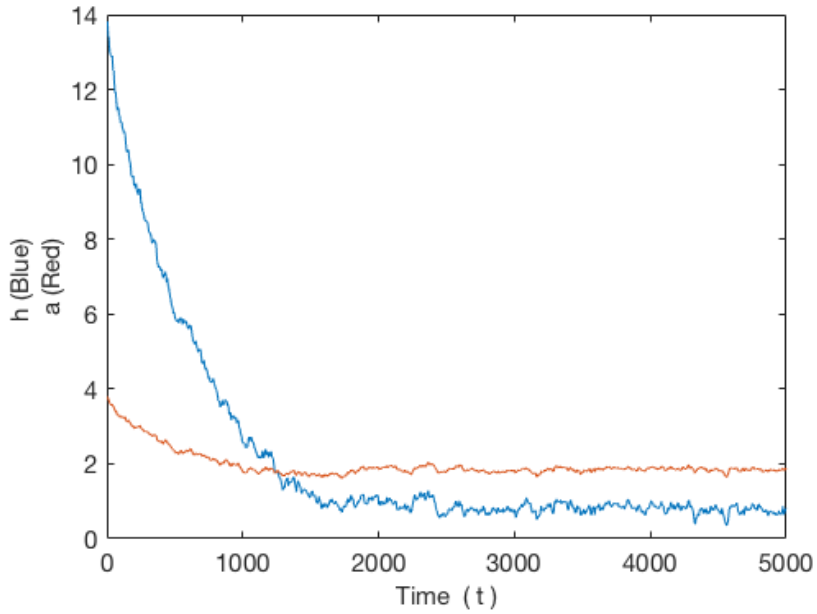

Figure 2.3: Energy and norm densities as functions of time. After the transient time observed in Figure **??**, the system thermalises at $h \approx 1$ and $a \approx 2$.

number of relevant decimal places. Due to the chaotic nature of the dynamics, it is relevant where the truncation occurs. In order to make sure that the separation is minimal (if any), one must save all floats with a precision of 16 decimal places, which is the same precision as that pre-set by `MATLAB` for `float` variables. Of course, this would have to be adjusted accordingly to the programming language used and the precision of the defined variables in the preferred language.

Note: When applying the modulo function from the `MATLAB` library, the truncation seems to occur much faster than before the 16^{th} decimal place, so it is advised to avoid using `mod()` when saving phases. Most wave-functions are therefore saved using Cartesian coordinates.

- When studying grand-canonical ensembles one must employ the Langevin heat baths defined in Section **2.1.2**. These baths require the numerical creation of white Gaussian noise. In order to be able to reproduce data, one must have a

clearly defined seed for the white Gaussian noise. Interrupting the simulation at a random time step would create difficulties when re-creating the noise. In order to avoid such problems, the backup state should be done after pre-settled time spans (i.e. 10 units), together with the seed which was used to generate the noise during that interval. Usually, these seeds are integers which are incremented by 1 after each integration interval. During certain simulations, we can observe the spontaneous migration of the breather, or a sudden change in height (most of the simulations fall in a laminar regime where the breather norm is frozen for astronomically long amounts of time). The simulations which show intriguing events can be repeated, and more data can be saved during the unusual evolution of the breather. This will be later used to understand the nature of the rare events.

- In the case when one wants to save only the slow components of a given state, one must average over exactly one rotational period (in the case when a single breather is present), using a very small integration time step. This will average out the components oscillating with the fast rotational frequency of the breather and most higher harmonics. It will not, however average out slow terms of high orders. This impediment, together with the chaotic dynamics of the equations, will lead to separations over long time scales between the 'slow zero-order component' and the full wave-function of the condensate.

2.2 Numerical Simulations of Breather Dynamics

2.2.1 Lack of Breather Tails in Large Backgrounds

A breather is a localised solution of the DNLSE [65], which is a stationary point of said equation. In order to satisfy the stationary state requirement, the frequencies at all lattice locations must be identical. In addition to that, the peak is localised at one lattice site [29] and all neighbouring locations will have occupancy numbers which

decay exponentially with the distance from the central peak.

In reality, these ideal solutions, which can be infinitely long-lived, are not what we see in real physical systems due to two constraints

1. Limited size effects - Lattices cannot be made to be infinitely long, at some point the tails of the breather have to encounter either a reflective boundary, a dissipative boundary or a thermostat.

2. The presence of noise - The noise can be either very small (infinitesimal), and in this case the trajectories of the breathers under the action of the DNLSE follow very closely the ideal case, where the breather has tails which decay exponentially fast in space and the soliton is astronomically long-lived [37]. Alternatively, the noise can be large, of order $\mathcal{O}(1)$, and can dominate the background completely, submerging the breather tails entirely [66]. When the noise is given by Langevin heat baths, its amplitude determines the temperature of the background [50]. The work presented in this thesis focuses on breathers in the presence of large backgrounds, where the pinned breather is very well localised, to a single site of the lattice.

At this stage, it is useful to compare the ideal solution [29, 33] which is derived for breathers in infinitely extended lattices, isolated from the environment, to that obtained by integrating the DNLSE in a finite lattice in contact with Langevin heat baths.

Looking for the breather tails in the frequencies of the background

The frequencies of the background are the first place to look for any reminiscent breather tails. In Figure 2.4, one tracks the frequency of each site in the lattice. This is done by tracking the phase at each site, and taking the numerical derivative of this quantity, by dividing its change in magnitude by the elapsed time. This rudimentary definition of frequency proves very powerful when looking at long time-scale statistics. First of all, one can see that the breather has a very large frequency, which is

approximately equal to $2 \times |z_{breather}|^2$, just as expected. In addition, one can notice that all background sites, except the first neighbour rotate in very similar ways. The background is characterised by the same frequency at all sites, given by $2a$, and this is to be expected, since all sites are thermalised with the heat baths. What is surprising is the anomalous behaviour of the first neighbour, which has a much larger variance in the frequency distribution than every other background site. This implies the existence of a small residual tail at site $j = 1$, which is in agreement to the findings of Figure 2.6. Later in this Chapter, the frequency will be defined as the dominant component of the Fourier spectrum, which will be calculating using Fast Fourier Transforms (as it will later follow, that quantity is also approximately equal to $2 \times |z_{breather}|^2$).

It therefore follows that the breather tails are completely buried by the large backgrounds generated by Langevin heat baths. One might also expect to have analogous dynamics for all background sites (i.e. all background sites will have identical histograms for their amplitudes and phases - in Grand Canonical Ensembles, these histograms will be purely dictated by the white Gaussian noise), except the very first neighbour of the breather. The differences in the dynamics of these sites are not at this stage clear yet. One must go beyond numerical tests to classify and quantify these differences.

Looking for breather tails in the amplitudes of the background

The next test one can do is to look at how the amplitudes behave in a set-up where the background is large - i.e. of order $\mathcal{O}(1)$. Figure 2.5 shows the amplitude distribution for the same set-up as the one used to scan frequencies in Figure 2.4. Just as before, the background thermalises with the heat bath, and all sites are statistically identical. Here, the average amplitude thermalises at the value $a = 0.7$, which is exactly what one expects from the infinite temperature heat baths of density $a_L = a_R = 0.7$. Moreover, the variance of the mass density for all background sites is approximately 0.7, which suggests a Poissonian distribution. This is in perfect agreement with an

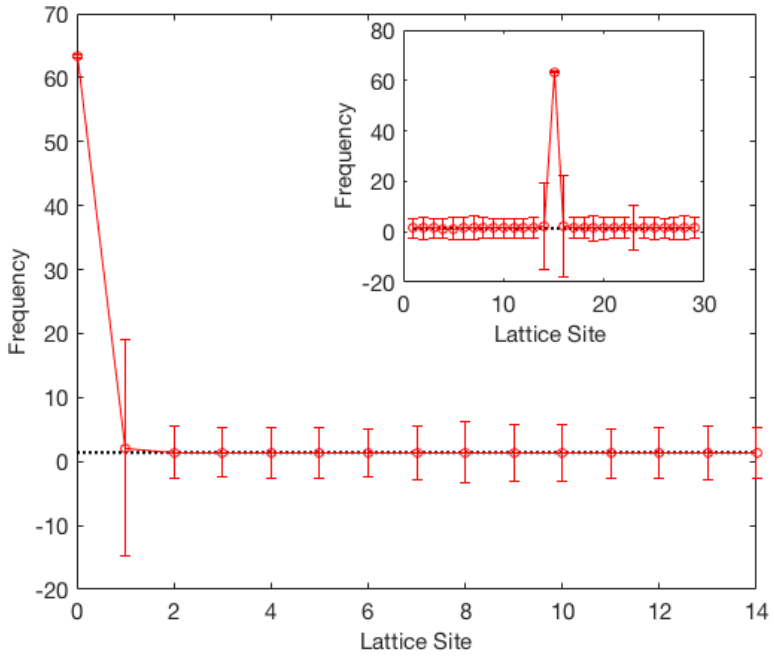

Figure 2.4: The frequencies of a breather and its surrounding sites in contact with two infinite temperature heat baths ($a_L = a_R = 0.7$). The breather is situated at the middle of a lattice of length $N = 31$. The background on both sides of the breather thermalise at the frequency $2a_L = 2a_R$. The first neighbours of the breather display a broad variance in their rotational frequencies, implying some interaction with the breather.

infinite temperature background.

Figures 2.4 and 2.5 focus on the thermodynamics of the background, and show that all background sites are indistinguishable from each other when it comes to the evolution of their amplitudes and phases. We will now focus on the intermediate time scale (i.e. slower than the breather rotation, but not as long as the thermalisation times), where we can see the evolution of the background. On this scale, if we look at the evolution of the background, we notice that all background sites fluctuate (see the black curve in Figure 2.6), while the breather norm stays effectively unchanged (see the blue curve in Figure 2.6). One site of the background displays some anomalies, namely the first neighbour of the breather, which shows some fast fluctuations (red curve in Figure 2.6). This is in perfect agreement with the frequency scan from Figure 2.4.

2.2.2 Breather life-times in large backgrounds

Breathers are stationary states of the DNLSE, and therefore in the ideal case where no noise is present and no limited size effects occur, they would be infinitely long-lived. However, in the system studied throughout this work, breathers are immersed in large backgrounds, which, as seen in the previous chapter, completely bury their tails and localise these excitations to one single site only. Not only that, but the background frequencies are clearly of a different order of magnitude from those of the pinned breathers.

When integrating the DNLSE in a micro-canonical set-up (energy and norm are kept constant), one can either use Yoshida symplectic integrators [28], or one can employ the Langevin heat baths described in the previous parts of this work with the help of fourth-order Runge Kutta integrators. When using Runge Kutta integrators, one must be careful to tune the time step in such a way that any diffusions of the Hamiltonian are minute. After observing multiple simulations in a micro-canonical set-up, an appropriate time step is 1/500 of the smallest rotational period of the lattice has been identified.

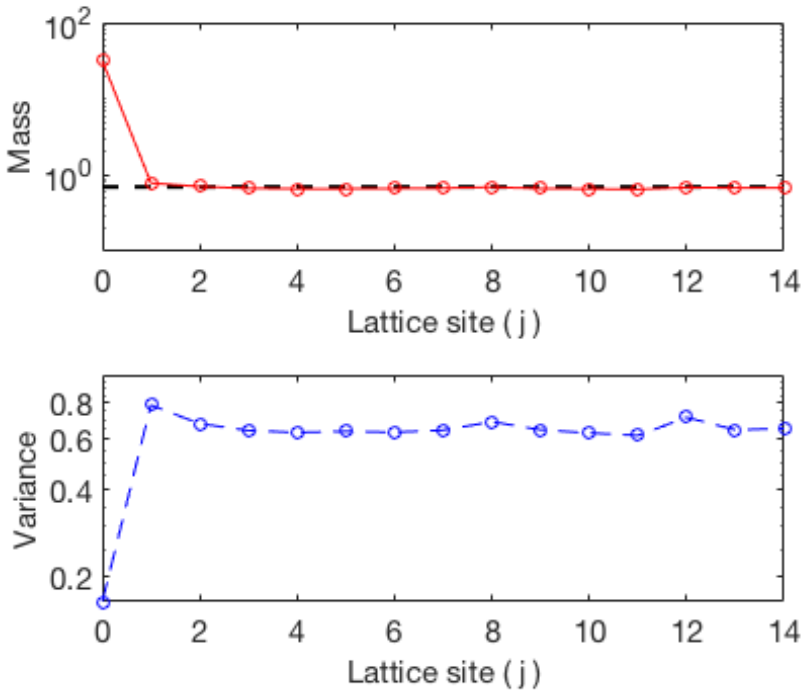

Figure 2.5: The mass distribution for a background of 14 sites in contact with a breather at site $j = 0$ ($|z_0|^2 = 25$) and an infinite temperature heat bath at site $j = 15$ ($a = 0.7$). The background thermalises at the amplitudes given by the heat baths ($a = 0.7$, depicted by the black dotted line). Moreover, the variance also stabilises around the value 0.7, suggesting a Poissonian distribution, therefore an infinite temperature background.

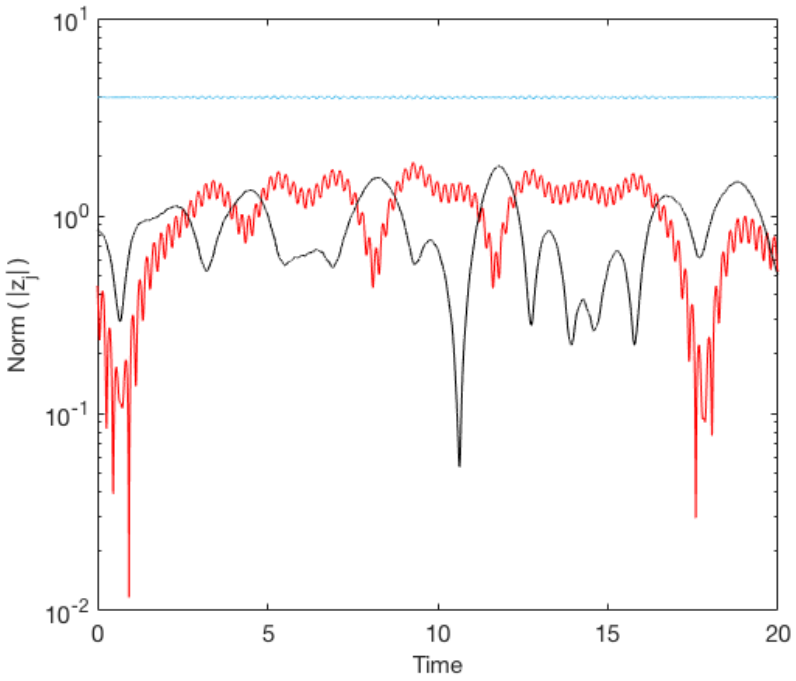

Figure 2.6: The amplitude of a breather (blue), and the amplitudes of the nearest (red) and second nearest (black) neighbours. The breather sits at site $j = 0$ in a lattice of 7 sites which is in contact with Langevin heat baths at $T = 3$ and $\mu = -3.4$. While the breather amplitude is remarkably constant, one can see that the neighbouring two sites have amplitudes which change drastically throughout the evolution. In addition, there is no exponential decay in the norms, since the two quantities have very similar orders of magnitude. All sites beyond $j = 2$ will also display trajectories very similar to this one.

The frequency of a breather of mass $|z_b|^2$ is $\omega \equiv 2 \times |z_b|^2$ and therefore the rotational period associated with its oscillation is $2\pi/\omega = \pi/|z_b|^2$. It follows that the adaptive time step used for the simulation (according to the criterion specified above) will be $\pi/(500|z_{MAX}|^2)$.

The maximum frequency could also be identified through the use of Fast Fourier Transforms, just as in the case of the low pass filters. That would slow down the simulation considerably, though, and the rough approximation for the maximum frequency contained by the expression $\omega \equiv 2 \times |z_b|^2$ is more than sufficient to define an accurate adaptive integration time step, without slowing down the simulation with futile numerical Fourier analysis.

Breathers in the presence of large backgrounds are still very stable structures, even though they are not perfect stationary points of the DNLSE. To investigate their behaviour, one can look at the simulations presented in Figure 2.7, where seven breathers of different initial sizes are allowed to evolve under the DNLSE until the time of their decay. One can observe that the Hamiltonian of the breather (i.e. the kinetic term, given by $|z_b|^4$) is approximately constant throughout the breather's existence until a very sharp decay is observed. In addition, larger breathers have exponentially longer lifetimes. This exponentially fast decoupling between breathers and their surroundings creates difficulties when wanting to study the dynamics of large breathers, because, in addition to the exponentially longer life time, one has to employ a time step that goes down as a power law (i.e. $|z_b|^{-2}$) of the breather norm. This means that the numerical algorithms will slow down more than exponentially as the breather mass is increased, which is very inconvenient.

The breather Hamiltonian contains fast terms which originate from the rotational frequency and high order harmonics. These can be filtered out simply by averaging the data depicted in Figure 2.7 over intervals of 250 units. After this process, one obtains the neater plot from Figure 2.8. In this new figure, one can see that a very slow diffusion process is present. In addition, very rarely throughout the simulations there

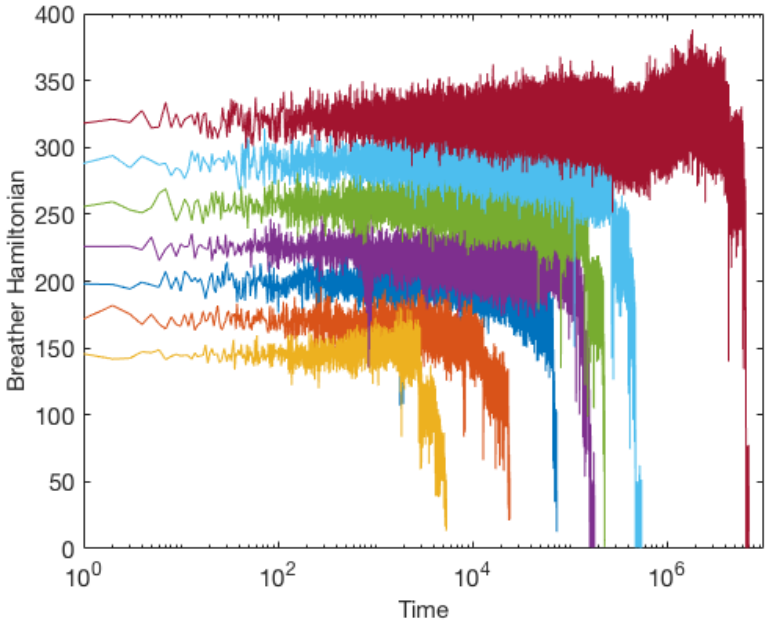

Figure 2.7: The time evolutions for the energy of seven breathers of different initial sizes. One can immediately observe that larger breathers live exponentially longer.

are large jumps in the breather norm, similar to what was initially observed in Figure 2.13. These rare events occur exponentially rarely as the breather size is increased. The similar scaling might suggest at this stage a correlation between the rare events and the overall life times of breathers.

The questions that arise from these findings are:

- What causes the extreme events, and why are they exponentially rarer for taller breather?
- Are these events related to the death of breathers?
- Can one explain the exponential decoupling between breathers and large backgrounds through the prism of rare events?
- What role does diffusion play in the life time of breathers?
- Can one accelerate the integration of the DNLSE through an integration mechanism which works under the predictor corrector paradigm?

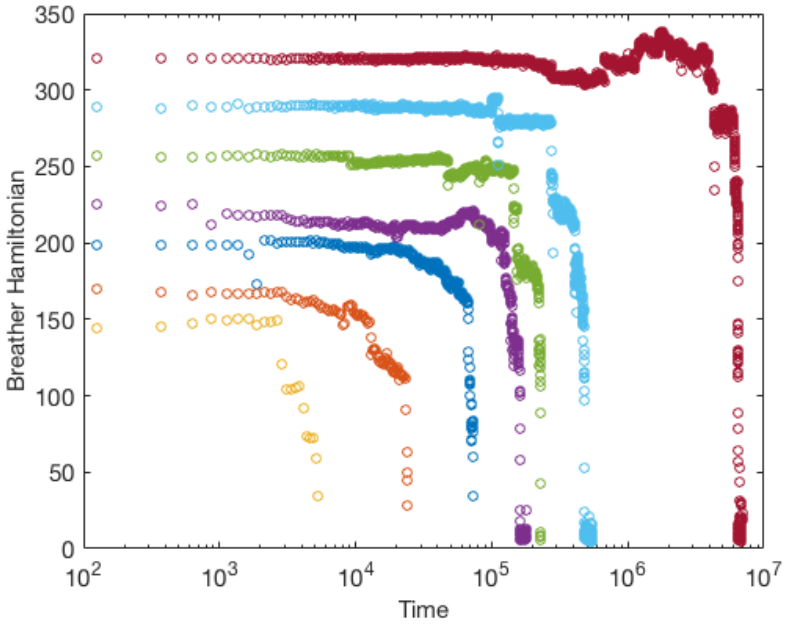

Figure 2.8: The time evolutions for the energy of the same seven breathers from Figure 2.7 after filtering out the fast harmonics by averaging over intervals of 250 units. One can immediately observe that larger breathers live exponentially longer.

The first step in answering these questions is to classify and investigate the nature of rare events, which is done in the next chapter.

2.3 Numerical Low-Pass Filters

2.3.1 Building a Low-Pass Filter

Throughout this work (for breathers of initial norm $|z| \approx 5$) it is common to refer to the three characteristic times of the system:

- Times of the order of one breather period, which range in the domain 10^{-2} to 10^{-1} units. During these time ranges, most coordinates of the wave-function stay constant, with the exception of the phases of the breathers, which increase linearly.

- Times of the orders 10^0 to 10^1, during which the backgrounds evolves slowly and

the breather height barely changes.

- Times of the order 10^5 to 10^6 and beyond, during which breathers can spontaneously disappear or change location and size.

Even if the interest is to investigate events which occur over the longest of the three scales, it is crucial to study the first two scales, and how they are interconnected in order to form any theories on the evolution of breathers over scales of 10^5 units and beyond.

The first step in doing this is to numerically build a low-pass filter, which separates the dynamics of the fastly rotating breather from that of the slowly evolving background. In order to do this, one can use the `fft` (Fast Fourier Transform) protocol incorporated in the MATLAB library. The filtering algorithm consists of the following steps:

1. For a quantity with a known time dependence ($Z(t)$) which is stored into an array, calculate its time average $\bar{Z} \equiv \langle Z \rangle$.

2. Calculate the oscillating component of the signal through the subtraction $Z_{osc} \equiv Z - \bar{Z}$

3. Apply the `fft` (Fast Fourier Transform) algorithm on the oscillating component Z_{osc} to obtain the spectral distribution of the frequencies in this signal, i.e. $\mathcal{F}(Z_{osc})$

4. Define a cut-off frequency (f_{CO}), over which no components of the spectrum will be kept, and define the heavy-side step function filter

$$\mathcal{H}_{f_{CO}}(f) \equiv \begin{cases} 1 & f < f_{CO} \\ 0 & f \geq f_{CO} \end{cases} \tag{2.29}$$

5. Apply the low pass filter on the frequency spectrum by multiplying the low pass

projector with the initial Fourier transform to obtain the slow signal $S_{slow} \equiv \mathcal{H}_{f_{CO}}(f) \times \mathcal{F}(Z_{osc})$

6. Apply the Inverse Fast Fourier Transform (`ifft`) and add the initial average to get the slow signal $\bar{Z} + \mathcal{F}^{-1}(S_{slow})$

As an example, let us look at the behaviour of the first neighbour for a breather of height $|z_0| = 4$. The time dependency of this quantity is depicted in Figure 2.9. This function is large, reaching values of order $\mathcal{O}(1)$, due to the thermalisation with a Langevin heat bath with $T = 3$ and $\mu = -3.4$. In addition to the slowly fluctuating component from the positive temperature background, one also sees a small rapidly oscillating signal of size $\mathcal{O}(10^{-1})$, which comes from the interaction between the background and the breather. This fast harmonic present in the first neighbour has been described in Figures 2.6 and 2.4. After applying the filtering algorithm introduced in this chapter, one obtains the function depicted in Figure 2.10. One can see that the numerical filter defined above is highly effective at extracting the slow dynamics from the full trajectory.

2.3.2 Behaviour of Slow/Fast Quantities

A breather at site j will have a rotational frequency which can be approximated by $2A_j^2$ [27]. These frequencies are usually much larger than those generated by the backgrounds coming from the heat baths. It was already shown previously, in Figures 2.9 and 2.10 that these large breather frequencies also induce high order harmonics on the neighbours of the breather, which can be filtered out numerically. It is very relevant to see what happens in the opposite directions, i.e. to study how the background perturbs the dynamics of the breathers. For this, let us look at the example presented in Figure 2.11, where a lattice of 15 sites put in contact with backgrounds at infinite temperature evolves for 120 time units. A breather of height $|z_8| \approx 4$ is initialised in the middle of the lattice.

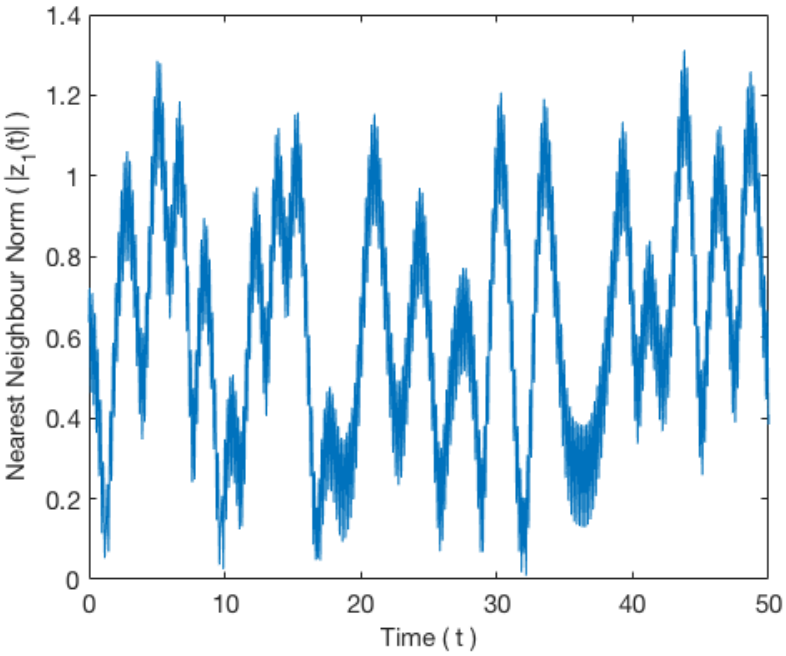

Figure 2.9: The evolution of the amplitude for the wave-function of the nearest neighbour of the breather.

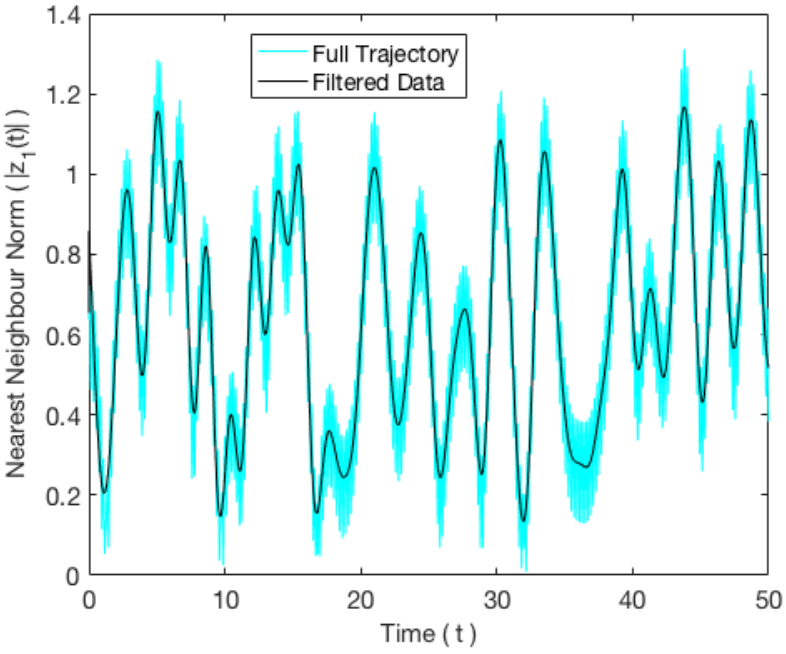

Figure 2.10: The same function as in Figure 2.9, after applying the numerical low pass filter introduced in this chapter

It is interesting to plot the evolution of the breather norm, as done in Figure 2.12. From this plot, one can infer that the breather amplitude is almost constant, around a value of $|z_8| \approx 3.83$ and contains fast oscillating terms of size $\approx 10^{-1}$. It is not clear at this stage what causes this behaviour. In order to explain this, one must build a perturbative calculation.

At this stage, it is interesting to make use of the low pass numerical filters introduced in Section 2.3.1. After filtering out the fast components from the breather norm, one obtains the much smoother time dependency depicted in Figure 2.13. One can see that the fluctuations of the breather's norm are of order 10^{-3} until the time of interaction (i.e. $t \approx 70$), when a small drift in the breather norm occurs. After this event, the small-size-fluctuation behaviour resumes.

At this stage one might ask:

- What causes the large fluctuations in Figure 2.12?
- When filtering out the fast frequencies, what leads to the smaller and slower fluctuations depicted in Figure 2.13? Also, is there a way to quantify these slower fluctuations and link them to the excitations from the background?
- What is the nature of the event observed at time $t \approx 70$, and what distinguishes this event from the rest of the evolution?

All these questions can only be answered through the means of a perturbative calculation, which is necessary to characterise the nature of the interaction between breathers and their backgrounds (see Chapter 4).

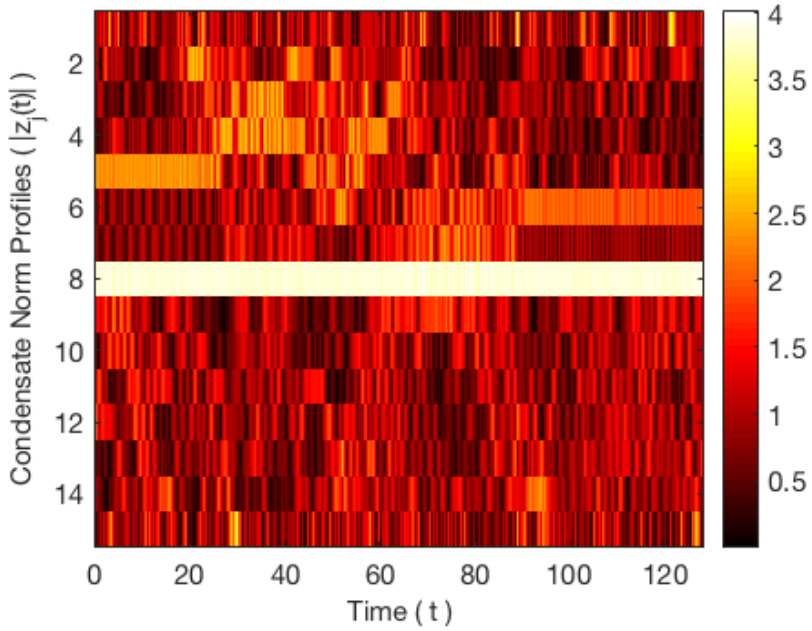

Figure 2.11: The evolution of the amplitude of the wave-function for the chain: One can observe that a large excitation is formed spontaneously at site $j = 6$, and after ≈ 70 units, this excitation interacts with the breather. The full nature of the interaction is not clear from this figure alone, and further plots are required.

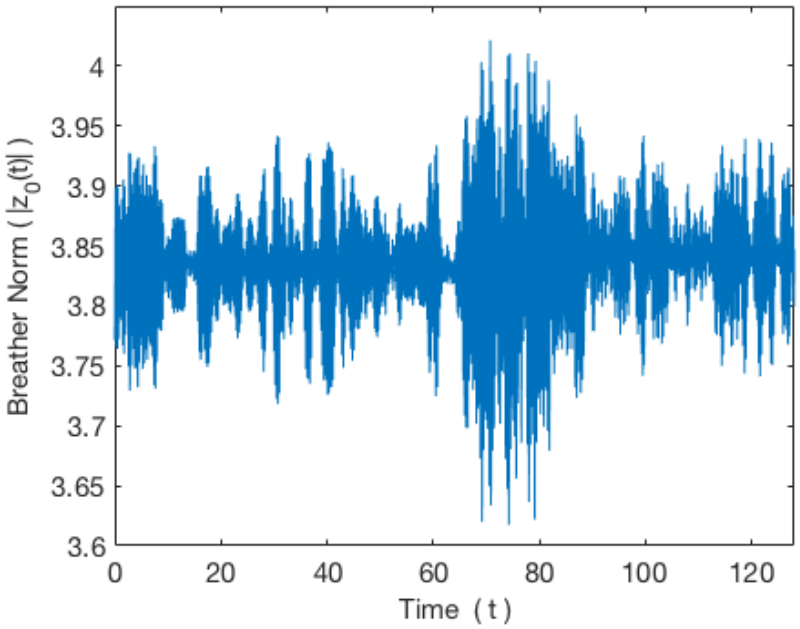

Figure 2.12: The breather norm fluctuates rapidly around the value $|z_0| \approx 3.85$. It is not clear whether there is any drift in this norm, other than the fast harmonics generated by the breather rotation.

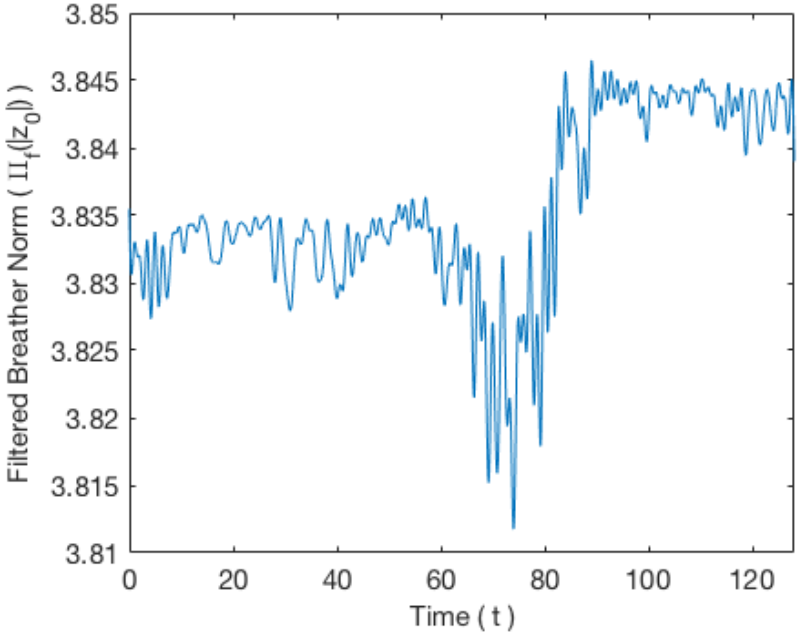

Figure 2.13: After applying the numerical low pass filter on the norm from Figure 2.12, one can see a clear jump at $t \approx 70$, which was not visible before applying the filter.

Chapter 3

Review of Extreme Events in the DNLSE

The nature of the extreme events will be studied more thoroughly throughout this chapter using both analytical and computational means. A possible hypothesis for their generation is the spontaneous formation of large excitations in the phonon background which strongly perturb the breather. Alternatively, rare events could be triggered by resonances or strong interactions due to crossing of a separatrix [44]. Before proceeding to algorithms which employ perturbative calculus, it would be very useful to clarify the nature of these events, and also attempt to quantify and organise them into several categories.

3.1 Analytical Investigation of Dimer Systems

The simplest analytical system one can look at consists of a dimer, which is a lattice with exactly two sites, in a micro-canonical ensemble. This type of set-up has been studied extensively in the literature since 1986, when Kenkre and Campbell came up with analytical solutions for the DNLSE dimer [44]. One decade later, it was further extensively investigated by Smerzi et al. [67]. In this simple system, the breather

would be defined as the site where the maximum mass is situated (there are only two possible locations). Because this system is closed, the overall mass and Hamiltonian are conserved. The phase space is of dimension 4, but given the two conservation laws present in a dimer, the real dimension for the degrees of freedom is two. The conservation laws state

$$\begin{aligned} \mathcal{N} \equiv A_0^2 + A_1^2 &= \texttt{constant} \\ H \equiv A_0^4 + A_1^4 + 2A_0A_1\cos(\psi_0 - \psi_1) &= \texttt{constant}. \end{aligned} \tag{3.1}$$

Naturally, one expects the absolute phases to have no physical meaning, and one would only look at the phase difference when characterising this simple model. Immediately, looking at the equations above, one can see that the conservation laws depend on the phase difference only, and not on the individual value of the phases. It is therefore useful to introduce the variable $\delta \equiv \psi_0 - \psi_1$. In addition, due to the conservation of mass, atoms can only migrate between two possible sites, making the visibility a very good candidate for the second variable of the system. The visibility can be defined as the difference in intensities, i.e. $P \equiv (A_0^2 - A_1^2)/\mathcal{N}$. The norm at the denominator normalises this quantity, bounding it to the interval $[-1, 1]$, regardless of the overall mass of the condensate.

The sytems of equations from (3.1) can be solved to calculate the values of the amplitudes of the dimer

$$\begin{aligned} A_0 &= \sqrt{\mathcal{N}\tfrac{1+P}{2}} \\ A_1 &= \sqrt{\mathcal{N}\tfrac{1-P}{2}}. \end{aligned} \tag{3.2}$$

These expressions can be substituted in the Hamiltonian to express this quantity in terms of δ and P

$$H = \frac{\mathcal{N}^2}{2}(1 + P^2) + \mathcal{N}\sqrt{1 - P^2}\cos(\delta). \tag{3.3}$$

Now, given the fact that both H and $\mathcal{N}$ are conserved quantities, it is more elegant

to use the reduced Hamiltonian

$$\mathcal{H} \equiv \frac{\mathcal{N}}{2} P^2 + \sqrt{1-P^2}\cos(\delta), \tag{3.4}$$

which will also be conserved for all trajectories of the dimer.

In polar coordinates, the four coordinates of the dimer evolve as

$$\begin{aligned} d_t A_0 &= A_1 \sin(\psi_0 - \psi_1) \\ d_t \psi_0 &= 2A_0^2 + \tfrac{A_1}{A_0}\cos(\psi_0 - \psi_1) \\ d_t A_1 &= A_0 \sin(\psi_1 - \psi_0) \\ d_t \psi_1 &= 2A_1^2 + \tfrac{A_0}{A_1}\cos(\psi_1 - \psi_0), \end{aligned} \tag{3.5}$$

but now having the knowledge that the trajectory is bound to a two-dimensional subspace, it is highly desirable to express the differential equation in terms of δ and P and arrive to

$$\begin{aligned} d_t P &= 2\sqrt{1-P^2}\sin(\delta) \\ d_t \delta &= 2P\Big[\mathcal{N} - \tfrac{1}{\sqrt{1-P^2}}\cos(\delta)\Big]. \end{aligned} \tag{3.6}$$

Renormalising the time as $\tau \equiv 2t$, one can obtain the equations of the dimer

$$\begin{aligned} d_\tau P &= \sqrt{1-P^2}\sin(\delta) \\ d_\tau \delta &= P\Big[\mathcal{N} - \tfrac{1}{\sqrt{1-P^2}}\cos(\delta)\Big], \end{aligned} \tag{3.7}$$

which also satisfy the conservation laws $\mathcal{N} = \texttt{constant}$ and $\mathcal{H} \equiv \frac{\mathcal{N}}{2}P^2 + \sqrt{1-P^2}\cos(\delta) = \texttt{constant}$. These equations, together with the two conservation laws are everything we need to understand the dynamics of dimers.

At this stage, it is useful to present a numerical test where for different values of $\{P_0, \delta_0\}$ and a fixed value of $\mathcal{N}$ (in this case the overall mass was assigned the value 6), the system is allowed to evolve until the orbit closes. Note that the system is two dimensional and periodic, regardless of the value of the initial conditions. Some of these orbits are visible in Figure 3.1. There, one can notice two types of orbits:

- Orbit I: For positive initial values of P, the orbit goes to negative values of the visibility. These orbits are centred around the stationary point ($\delta = \pi, P = 0$), and start as concentric circles which grow until they degenerate to an ellipsoid like trajectory centred around the same stationary point. The orbits never contain points which have $\delta = 0$, meaning that the phase difference is not allowed to explore all the possible values. This type of orbit corresponds to a pendulum like trajectory, where the location of maximum amplitude shifts from site $j = 0$ to site $j = 1$ repeatedly, in a periodic manner, following a zigzag like pattern.

- Orbit II: For positive initial values of P, the visibility always stays positive (or more generally, it never changes sign, no matter how much time passes). These orbits allow the phase difference to explore all possible values, including $\delta = 0$. This orbit corresponds to fluctuations in the breather height, without ever letting the breather change location. In other words, the size of the breather changes, but its location never does so.

These two types of orbits are the typical regimes of a pendulum, in one case the pendulum oscillates around an equilibrium value, and in the other the initial energy is large enough to allow the pendulum to rotate all the way (the phase can take all possible values in the interval $(0, 2\pi]$).

There is also a border on the y-axis, given by $P_{separatrix}$ which shows the threshold of P over which all orbits are of type II. Below this value, both orbits are possible. The next logical step is to find an analytical equation for this separatrix.

Let us take two points (A and B) on an ellipsoid like trajectory (Orbit I) and write the conservation of the reduced Hamiltonian

$$\mathcal{H} = \frac{\mathcal{N}}{2} P_A^2 + \sqrt{1 - P_A^2}\cos(\delta_A) = \frac{\mathcal{N}}{2} P_B^2 + \sqrt{1 - P_B^2}\cos(\delta_B). \tag{3.8}$$

Let us take point A to be the point for which P reaches its maximum value. Using either Langrange multipliers, or simply by observing Figure 3.1, one can deduce that the

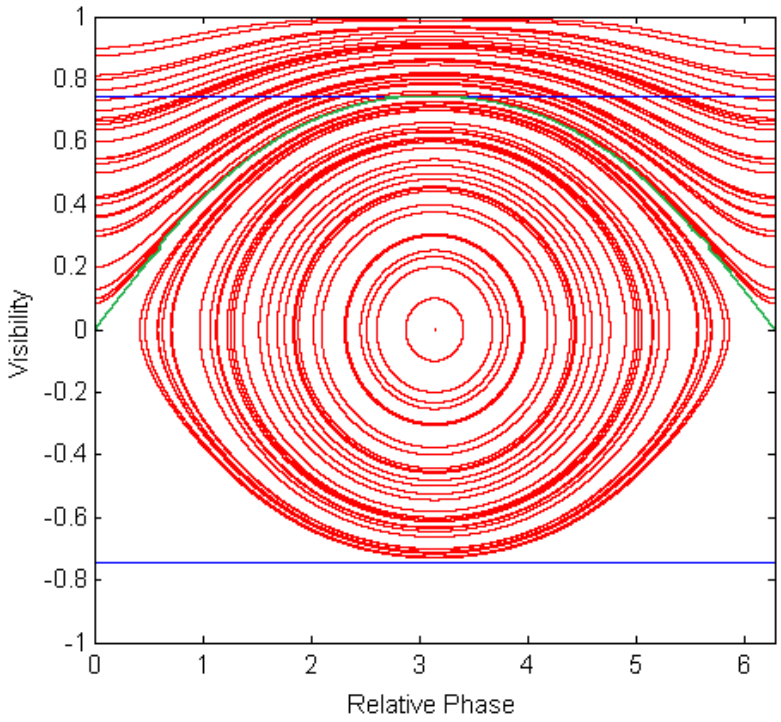

Figure 3.1: Trajectories for a dimer for different initial conditions. One can observe two types of periodic orbits: orbits which do not allow the system to pass through $\delta = 0$ and orbits which do allow this value of the phase difference. The blue horizontal lines denotes the upper and lower thresholds of the parameter P required to generate the separatrix plotted in green.

maximum value of P is always reached when δ is exactly equal to π. The conservation law from (3.8) therefore can be expressed as

$$\frac{\mathcal{N}}{2}P_{max}^2 - \sqrt{1-P_{max}^2} = \frac{\mathcal{N}}{2}P_B^2 + \sqrt{1-P_B^2}\cos(\delta_B), \tag{3.9}$$

where B is any other point on the ellipsoid-like trajectory.

In order to find the separatrix, one will look for the largest possible orbit of Type I, which goes as close as possibe to the edges of Figure 3.1, given by the pairs ($\delta = 0, P = 0$) and ($\delta = 2\pi, P = 0$). Without loss of generality, we choose the first point (the origin) as point B (i.e. $B(0,0)$ will be on the ellipsoid). Replacing P_B and δ_B with zero in the previous equation we arrive at the following boundary condition

$$\frac{\mathcal{N}}{2}P_{max}^2 - \sqrt{1-P_{max}^2} = 1. \tag{3.10}$$

Introducing the new variable $V \equiv A_0^2 - A_1^2$, one immediately arrives to $V_{max} = P_{max}/\mathcal{N}$. Making all the substitutions in (3.10) one can determine the maximum visibility which defines the separatrix

$$V_{max} = 2\sqrt{\mathcal{N}-1}. \tag{3.11}$$

Now one can use that $\mathcal{N} = A_0^2 + A_1^2$ and that $V = A_0^2 - A_1^2$ to define the pair of dimer amplitudes which generate the separatrix

$$A_1 = A_0 \pm \sqrt{2}, \tag{3.12}$$

which implies that in order to generate a shift of the maximum excitation from site $j = 0$ to site $j = 1$, the first neighbour must have a minimum value of $A_0 - \sqrt{2} = |z_0| - \sqrt{2}$. The emergence of this separatrix will be the phenomenon responsible for the occurrence of bound states in spatially extended system. The model of the dimer cannot offer more

information beyond this simple separatrix model, and in order to model other extreme events further investigations are required.

From (3.11), it immediately follows that the threshold values for the parameter P which generate the separatrix

$$P_{boundary} = \pm 2\frac{\sqrt{\mathcal{N}-1}}{N}, \tag{3.13}$$

which are the equations of the two blue horizontal lines in Figure 3.1. It is easy to see that

$$\lim_{x\to\infty} P_{boundary} = 0, \tag{3.14}$$

which implies that as the mass of the dimer is increased, the red orbits from Figure 3.1 become more and more flat.

3.2 Partial Averaging near Resonance

Let us now return to a lattice of generic length, where a breather sits at one end (site $j = 0$) and let us write the differential equation for the breather wave function

$$\begin{aligned} d_t A_0 &= A_1 \sin(\psi_0 - \psi_1) \\ d_t \psi_0 &= 2A_0^2 + \tfrac{A_1}{A_0}\cos(\psi_1 - \psi_0), \end{aligned} \tag{3.15}$$

where the breather phase will be $\psi_0 = \omega t + \phi_0$. We can now use the clean time separation which was identified in Figure 2.4 to build the hypothesis that the first neighbour evolves much slower than the breather, therefore barely changing over one breather rotation. Therefore $A_1 \approx \bar{A}_1$ and $\psi_1 \approx \bar{\psi}_1$, where the over-bar represents the initial value of a variable (a constant). In addition one can also use that the breather amplitude and the ϕ_0 are also slow variables. This transforms the equations for the

breather wave-function into

$$\begin{aligned} d_t A_0 &= \bar{A}_1 \sin(\omega t + \bar{\phi}_0 - \bar{\psi}_1) \\ d_t \psi_0 &= 2\bar{A}_0^2 + \frac{\bar{A}_1}{\bar{A}_0} \cos(\omega t + \bar{\phi}_0 - \bar{\psi}_1), \end{aligned} \tag{3.16}$$

which can be integrated over one full rotation to arrive to

$$\begin{aligned} \delta A_0^{(1)} &= 0 \\ \delta \psi_0^{(1)} &= 2\bar{A}_0^2 \times \tfrac{2\pi}{\omega}, \end{aligned} \tag{3.17}$$

and from this it follows naturally to choose $\omega \equiv 2\bar{A}_0^2$, since we want the breather phase to change by exactly 2π after one full rotation. This means that, as a first approximation, after the breather rotates for one full rotation, the increments are

$$\begin{aligned} \delta A_0^{(1)} &= 0 \\ \delta \psi_0^{(1)} &= 2\pi, \end{aligned} \tag{3.18}$$

which means that after one full rotation the breather barely changes amplitude and, that in order to find the actual drift (any non-zero change in amplitude), one must go to higher terms in the expansions, which is not the point at this stage of the work. It will later be proved that the order at which this drift is different from zero is given by $\mathcal{O}(\omega^{-3})$. One might ask oneself though, if the rotation of the nearest neighbour of the breather can sometimes interfere with the frequency ω, and how would this drift change in the case of such a particular state.

In order to study this possibility, let as assume that we are on a resonant hyper-surface where the first neighbour of the breather rotates with a frequency in the vicinity of ω/m. The order of this resonant hyper-surface will be given by the denominator m. First we start by assuming that the mass of the first neighbour is

$$A_1^2 = \frac{A_0^2}{m}, \tag{3.19}$$

and proceed as before, by averaging over time from 0 $2\pi m/\omega$ this time to arrive at

$$\begin{aligned} \delta\psi_0^{(1)} &= 2\pi m \\ \delta\psi_1^{(1)} &= 2\pi \\ \delta A_0^{(1)} &= 0 \\ \delta A_1^{(1)} &= 0. \end{aligned} \tag{3.20}$$

All the rest of the Bose-Hubbard chain will obey the DNLSE, decoupled from sites $j = 0$ and $j = 1$ (i.e. $j = 1$ is effectively a reflective boundary in this first approximation). If m were not to be an integer (or at least rational) number, no integration interval could be found which would separate the dimer from the rest of the chain. Any dimer structures where the frequencies are not in resonance are not stationary points of the DNLSE in the first approximation, therefore they are more unstable.

Now, let us return to the differential equations for the phases at sites $j = 0$ and $j = 1$ (3.20), and obtain the approximate frequencies

$$\begin{aligned} d_t\psi_0 \equiv \omega &= 2A_0^2 + \mathcal{O}(1) \\ d_t\psi_1 \equiv \omega_1 &= 2A_1^2 + \mathcal{O}(1), \end{aligned} \tag{3.21}$$

and from this one can approximate the phase difference $\delta \equiv \psi_0 - \psi_1$ as $\delta = (\omega - \omega_1)t + \bar{\xi}$, where $\bar{\xi}$ is the initial phase difference. Combining what we know from (3.19) and (3.21) we arrive at

$$\delta = \omega\frac{m-1}{m}t + \bar{\xi}. \tag{3.22}$$

The differential equation for the breather norm (3.15) becomes

$$d_t A_0 \approx \sqrt{\frac{\omega}{2m}}\sin\left(\omega\frac{m-1}{m}t + \bar{\xi}\right). \tag{3.23}$$

This differential equation can be used to perform partial averaging near resonance, by integrating the derivative for one breather rotation exactly (i.e. by calculating

$\int_0^{2\pi/\omega} dt d_t A_0$ this time, therefore shrinking the integration interval from (3.20) by a factor of m). Luckily, this integral has a clear analytical solution given by

$$\delta A_0^{(1)} \approx \frac{1}{\sqrt{\omega}} \times \frac{\sqrt{m}}{\sqrt{2}(m-1)} \Big[\cos(\bar{\xi}) - \cos\Big(\bar{\xi} - \frac{2\pi}{m}\Big)\Big], \tag{3.24}$$

$$\delta A_0^{(1)} = \mathcal{O}(\omega^{-1/2}). \tag{3.25}$$

For very high order resonances, the limit

$$\lim_{m\to\infty} \delta A_0^{(1)} = 0, \tag{3.26}$$

suggests that higher order resonances play much less important roles than the first resonances (i.e. small values of m are expected to dominate the resonance patterns). This is also confirmed by the plot presented in Figure (3.2), where one can see the dependence of $\delta A_0^{(1)}(\hat{\xi})$ for the first seven resonances. Indeed, the plot confirms that as the order of the resonance increases the value of the drift goes down, becoming completely flat (at value zero) for very high orders. In addition, the largest drifts occur when the initial phase difference is $\bar{\xi} \in \{0, \pi\}$ for the resonance $A_1 = A_0/\sqrt{2}$, and at slightly different values from these initial phases for higher order resonances.

It appears that in the presence of resonances the drifts after one full rotation are of order $\mathcal{O}(\omega^{-1/2})$, while the drifts in the absence of these events are of order $\mathcal{O}(\omega^{-3})$. The second finding will be later proved analytically using Multiple Time Scale Analysis methods, but for now it can be confirmed by looking at the filtered drifts in Figure 2.13.

It follows from these findings that the bound states which occur due to the crossing of the separatrix in the previous section might not be the only strong interactions between the breather and its nearest neighbour. At this stage there are three different elements observed to affect the resonances in simulations

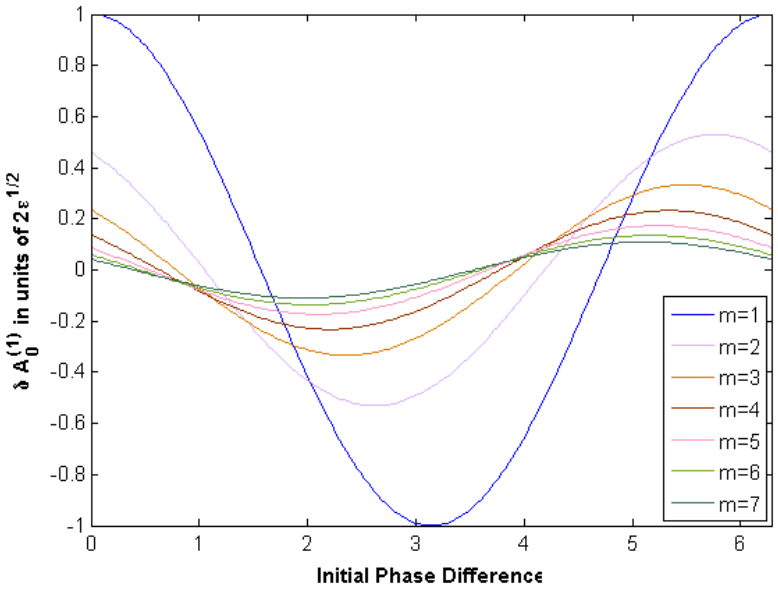

Figure 3.2: Change in breather amplitude after one full rotation in the presence of resonances of order $m \in \{1, 2, 3, ..., 7\}$. Higher order resonances induce smaller changes in the norm.

- The low order resonances induce stronger drifts, and high order resonances induce almost no change at all in the breather norm.

- Low order resonances occur when the neighbour is quite tall (of a similar order of magnitude as the breather), and as it was seen in Figure 2.7 larger excitations decay exponentially slower than small excitations. This means that not only is the interaction stronger for low order resonances, but also the time-spans during which these interactions occur are exponentially longer.

- Smaller excitations are exponentially more likely to occur in the phonon background. This means that higher order resonances are exponentially more likely to appear, but this counter- balances the previous two points. Even if the low order resonances are much stronger, they are exponentially less likely to occur, meaning that the weak interactions might play an important role on their own.

These three elements suggest that the breather life-times might strongly depend on

the temperature and chemical potential of the background, since these quantity dictate how the histograms of the amplitudes at the nearest neighbour look like. This hypothesis will be confirmed in Chapter 6.3.2, using Heterogeneous Multiscale Integration Techniques.

3.3 Numerical Investigation - Phase Scanning in the case of Catastrophic Collisions

Let us now look at a large perturbation (i.e. $|z_1|^2 > \mathcal{O}(1)$) in the absence of resonances. For this numerical experiment, we have chosen a breather of initial mass $|z_0| = 16$ and a neighbour of mass $|z_1|^{=}4.5$. These two values do not define a resonant hyper-surface, but the first neighbour can evolve in such a way to encounter such a surface sooner or later.

The phase difference δ was a random angle in the full domain interval $[0, 2\pi]$. The breather was initialised at one end (site $j = 0$) of a lattice with $N = 8$ sites which was put in contact with Langevin thermostats which generate backgrounds of order $\mathcal{O}(1)$. Two types of thermostats have been used:

- Finite temperature heat baths with $T = 10$ and $\mu = -6.4$ which generate backgrounds of average height $\langle |z_j| \rangle = 1$.
- Infinite temperature heat baths with $a = -\lim_{T\to\infty} \frac{T}{\mu} = 1$ which also generate background of average height 1.

Even if the average height for the two backgrounds are identical, the histograms for the amplitudes are different, therefore the statistics generated are expected not to coincide.

First, let us look on how the breather amplitude changes for the two scenarios by observing the trends in Figure 3.3. The findings there suggest that, in both scenarios, the largest drift in amplitude occur when the initial breather phase is $\delta = \pi$. In addition,

for both systems, there seems to be a preference for shifts towards a smaller value of the breather than for increases. However, before making any definitive statements on this finding, it is more cautious to consult the full data, and not just the overall trends.

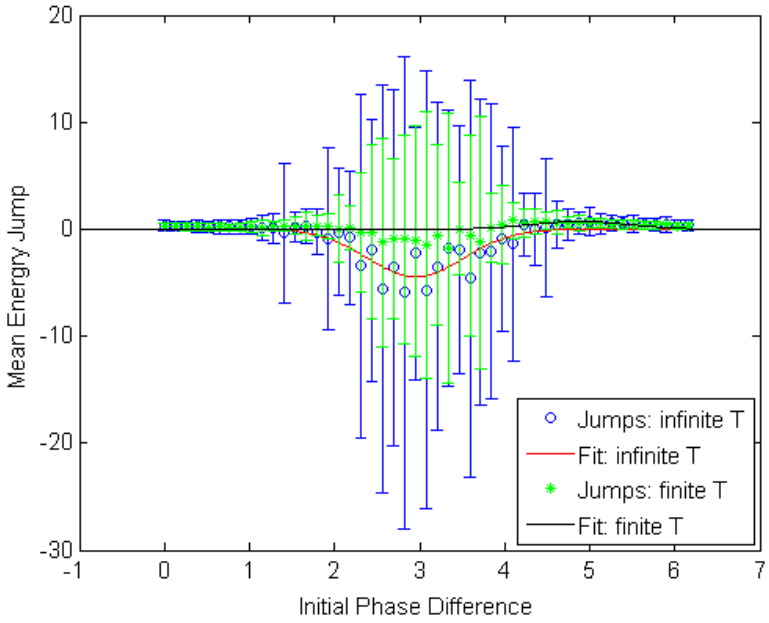

Figure 3.3: Average jumps in the breather Hamiltonian for different values of the initial phase difference. Initially, $|z_0|^2 = 16$ and $|z_1|^=4.5$ for all trajectories.

The raw data used to generate Figure 3.3 is presented in Figure 3.4. It now becomes apparent that negative jumps in energy (breather collapse) are catastrophic events. Both finite and infinite temperature scenarios appear to generate very similar types of transitions. This is because, even if the heat baths operate differently, the first neighbour and the breather start with pre-set values and the large excitations are not generated spontaneously by the heat baths, but are artificially imposed by the user. In order to see why the background doesn't seem to affect much the collisions, one must actually study the nature of these energy drifts. This will be done by performing amplitude scanning and looking at possible resonances.

Finally, in order to shed some light on the jumps observed in the numerics, one can look at the change of energy at site $j = 1$. We are trying to find out if the energy is

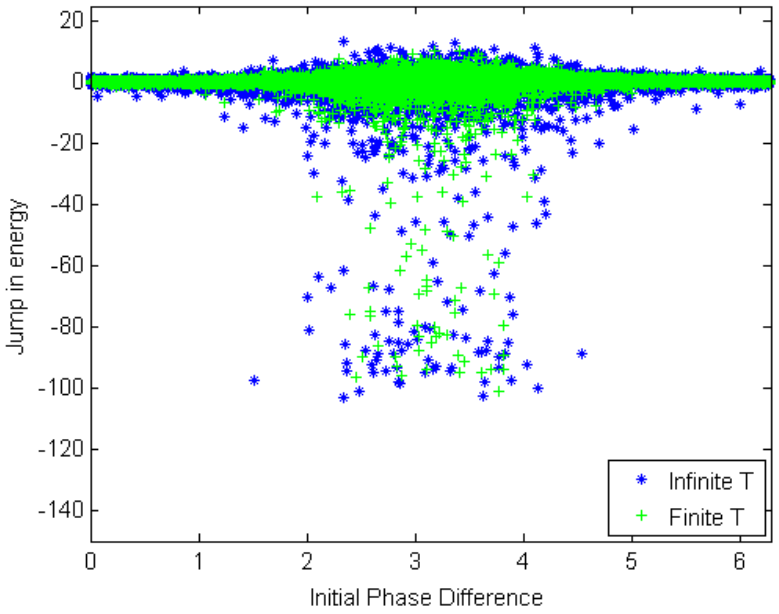

Figure 3.4: Raw data for the breather jumps used to generate the trends observed in Figure 3.3.

transferred from the breather to its nearest neighbour, like in the case of the crossing of a separatrix (note that here we are below the separatrix at $|z|^2 = (4 - \sqrt{2})^2 \approx 6.7$, so we shouldn't observe dimer-like shifts), or is simply dissipated into the background and ultimately absorbed by the heat baths. Figure 3.5 clarifies this issue, showing a clear shift of energy from site $j = 0$ to site $j = 1$, with very little dissipation of energy into the background. This findings explains why the different nature of the heat baths does not seem to affect the trajectories dramatically.

By doing the phase scanning in the case of catastrophic collisions, we discovered that $\delta = \pi$ is the phase difference with the most destructive consequences for the breather. The decays in energy however, seem to simply consist of events where most of energy shifts from site $j = 0$ to site $j = 1$, without the disappearance of the breather. The nearest neighbour might spontaneously increase to a value close to the separatrix at $|z|^2 = (4 - \sqrt{2})^2 \approx 6.7$, causing the breather to suddenly change location without significantly affecting its shape. This experiment does not explain, however, whether

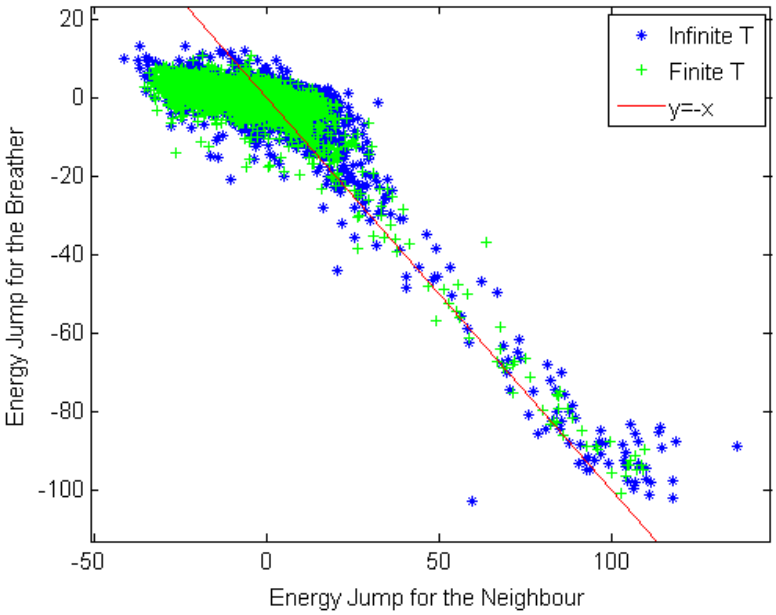

Figure 3.5: Transition curve for the energy between sites $j = 0$ and $j = 1$. Most of the energy lost by the breather seems to simply transfer to the nearest neighbour.

resonances play any role in the overall dynamics of breathers. This phenomenon would be better studied by the complementary type of scanning, that generated by varying the norm of the nearest neighbour.

The amplitude at site $j = 1$ is smaller than that of the breather but nevertheless, can act as a smaller breather of its own. This smaller excitation is more susceptible to destructive events from the background than the breather at $j = 0$ is. The excitation at site $j = 1$ can suddenly destabilise at any stage of the evolution and because of this, the breather can experience a drift of order $\mathcal{O}(\varepsilon^{-1/2})$ (where the smallness parameter ε, was defined as the inverse of the breather frequency). This drift is three orders of magnitude larger than the diffusion observed during laminar dynamics.

3.4 Numerical Investigation - Amplitude Scanning in the case of Catastrophic Collisions

It is now useful to perform the second type of scanning, where the initial phase difference between the breather and its nearest neighbour is kept constant, and the size of the neighbour is changed. We have now seen in all three previous examples that the most catastrophic type of interactions occurs for values of δ in the proximity of π, for both resonances and rare events. Therefore this will be the value of the initial phase difference chosen for this experiment.

In this new experiment, the heat baths have been set at $T = 3$ and $\mu = -3.4$ and the breather height was taken to be $|z_0|^2 = 36$. This larger value than what we had previously was chosen to work in a domain where the separatrix at $|z_0| - \sqrt{2}$ is sufficiently well separated from any possible resonance peaks which might appear at $|z_0|/\sqrt{2}$. The background was thermalised with the heat baths and then the nearest neighbour was given a random height $|z_1|^2 \in [0, 36]$. Once again, the average change in the breather energy was recorded. The results of this experiment are summarised in Figure 3.6. After varying the height of the nearest neighbour, one can arrive at the following conclusions:

- There is a strong jump in energy at the separatrix at $\left|\frac{z_1}{z_0}\right|^2 = \left(\frac{6-\sqrt{2}}{6}\right)^2 \approx 0.58$, which comes from the strong interaction of dimers described at the beginning of this chapter.
- There is a clear resonance peak of order $m = 2$ at $\left|\frac{z_1}{z_0}\right|^2 = \left(\frac{6-\sqrt{2}}{6}\right)^2 \approx 1/2$. This is clear evidence of resonance between the breather and its nearest neighbour
- There is a more modest resonance peak of order $m = 3$ at $\left|\frac{z_1}{z_0}\right|^2 = \left(\frac{6-\sqrt{2}}{6}\right)^2 \approx 1/3$.
- All higher order resonances were too weak and unstable to register any significant jumps in the breather height.

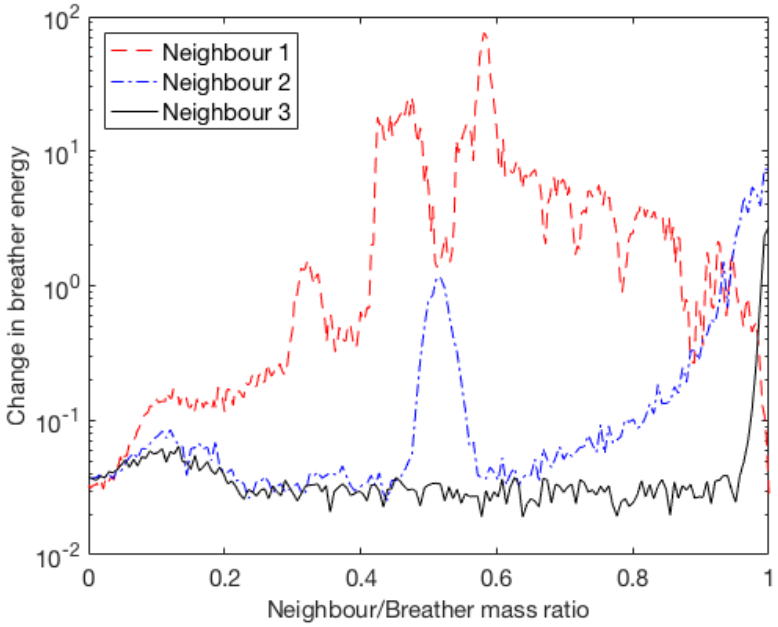

Figure 3.6: Interaction between the breather and its three nearest neighbours. The strongest interactions are with the excitations at site $j = 1$. There is a weak resonance with the second neighbour, and for the third neighbours all interactions are severely inhibited.

When the experiment was repeated for an amplitude scan at site $j = 2$ (findings summarised by the red curve in Figure 3.6), only one resonance peak survived (that corresponding to a resonance of order $m = 2$). This surviving peak was much less intense than what was observed in the case of nearest neighbour interactions. For interactions with the second neighbour, δ was chosen randomly, since there is no analytical knowledge of any special phase difference for sites which are two lattice positions apart.

Repeating the experiments with neighbours which are further away from the breather show close to no interaction at all. The breather Hamiltonian only starts to change when these neighbours reach sizes similar to the main excitation, which are beyond the interest of this current experiment, since such freak excitations are astronomically unlikely to occur.

At this stage, there is both analytical and numerical evidence of two types of strong interactions - those caused by the crossing of a separatrix, or those caused by the sudden crossing of resonant hyper-surface which creates drifts of order $\mathcal{O}(\varepsilon^{-1/2})$ (where ε is the inverse of the large rotational frequency of the breather), much larger than those observed in the numerics in the absence of resonance (of order $\mathcal{O}(\varepsilon^{-3})$). The frequency with which these rare phenomena occur is strongly dependent on the parameters of the heat baths. Excitations like the ones studied here (both in the analytical and the numerical investigations) spontaneously occur very rarely in systems which are freely evolving during time-spans of many orders of magnitude. Nevertheless, these toy models will prove very helpful when introducing Heterogeneous Multiscale Integration Methods (Chapter 6), which require clear definitions of rare events.

Chapter 4

Multiple Time Scale Analysis of Pinned Breathers

When simulating BEC in optical lattices with the DNLSE, discrete breathers are favoured in the presence of repulsive atomic interactions that are typical, for example, of ^{87}Rb atoms. Several methods have been suggested for the generation of discrete breathers in the DNLSE including the evolution from Gaussian wavepackets [8,68] and the relaxation from random phase states via localized losses [27].

Breathers have been mostly investigated in the presence of small backgrounds, when perturbative techniques can be developed to determine their stability [37,39]. Here we focus on the properties of localised solutions in the presence of a large (order $\mathcal{O}(1)$) fluctuating background. The background can either evolve in an isolated set-up, where the total energy and mass are conserved, or after including the interaction with suitable thermostats. In the latter case, the action of the heat baths is mimicked by implementing stochastic Langevin equations like in [50], where the temperature and the chemical potential of the background are given by the parameters of the reservoir.

Without loss of generality, we introduce a singular perturbation expansion for tall breathers in contact with a large background on one of their sides only. This simplified set up allows for the direct integration of analytical yet implicit expressions. As demon-

strated by the computational tests, the analytical findings can be extended to breathers in contact with a background on both sides, to lattices of any length, and under a large variety of configurations, i.e. periodic boundary conditions (PBC), reflecting boundary conditions (by imposing zeros at the ends of the Bose-Hubbard chain) or in contact with heat baths at the chain's ends.

In an ideal breather, the tails are perfectly synchronised with the oscillations at its peak and decay exponentially fast along the lattice. When the background is large, however, this synchronisation is destroyed and the dynamics of the background follow trajectories which are much slower than the breather oscillation. For large enough backgrounds, the breather's tails are completely covered by and indistinguishable from the background: in practice the localized solution occupies just a single site in the lattice. Even under these conditions, it is possible to investigate the stability of the localized solution and to determine the perturbations induced by the background on the breather.

We study the coupling between the breather and its surroundings by determining the leading perturbative order at which there is a change in the breather size after one oscillation period. Our work sheds light on the mechanism of adiabatic decoupling between localized solutions and their surroundings, leading to a analytical expressions that quantify the slow drifts in the breather amplitude due to the very weak interactions between the breather and its neighbours. In Sections 4.1, 4.2, and 4.3 we present the multiple-scale analysis based on the perturbation expansion in the inverse of the breather frequency. By averaging over one period of the breather rotation, we obtain a core differential equation 4.62 that describes the extremely slow dynamics of the breather amplitude. The theory is successfully compared with numerical simulations in Section 4.8 where we show its independence of the lattice length and application to infinitely-extended backgrounds. We also show that trimer and dimer configurations are topologically different from more extended systems, and that they display a higher degree of stability. Conclusions and future developments are presented in Section 4.10.

4.1 Separation of Time Scales - Outline of the general procedure

4.1.1 Asymptotic Expansions

The starting point is the Discrete Nonlinear Schrödinger Equation which can be written as

$$\frac{dz_j}{dt} \equiv d_t z_j = 2i|z_j|^2 z_j + iz_{j-1} + iz_{j+1}, \tag{4.1}$$

where the time t is dimensionless [8], $z_{-1} = 0$, while the boundary conditions at $j = N$ will be discussed later on.

In this chapter we investigate a set-up where a tall breather sits at $j = 0$, i.e. we set $|z_0(0)|^2 = I \gg 1$, to be compared with a background of amplitude order $\mathcal{O}(1)$. It is well known that the breather will eventually decay on a time scale that depends on its height, as we have noticed in Figure 2.7, back in Chapter 2.2.2. This type of exponential scaling is further confirmed by more numerical simulations which are presented in Chapter 6. Additionally, our collaborators in Florence, Stefano Iubini and Paolo Politi, obtained identical scaling curves for the breather life-times as a function of their initial mass [69]. We tackle the problem with a perturbative approach where the smallness parameter is not the background amplitude, as previously considered [37], but the inverse of the breather amplitude.

Upon expressing the breather state in polar coordinates, $z_0 \equiv A_0 \mathrm{e}^{i\psi_0}$, while using a standard Cartesian representation for the other lattice sites ($z_j = x_j + iy_j$, $j \geq 1$) the breather evolution can be written as

$$d_t A_0 = x_1 \sin\psi_0 - y_1 \cos\psi_0 \tag{4.2}$$

$$d_t \psi_0 = 2A_0^2 + A_0^{-1}(x_1 \cos\psi_0 + y_1 \sin\psi_0)\,. \tag{4.3}$$

From this representation it is transparent that if $A_0 \gg 1$, the phase ψ_0 rotates very

rapidly with a frequency given by $\omega \approx 2A_0^2 \gg 1$. From now on, $\varepsilon = 1/\omega$ is considered to be a smallness parameter for the development of a suitable perturbative approach. By introducing the "slow" phase $\phi_0 = \psi_0 - \omega t$, the DNLSE can be written as

$$\begin{aligned}
d_t A_0 &= x_1 \sin(\omega t + \phi_0) - y_1 \cos(\omega t + \phi_0) \\
d_t \phi_0 &= 2A_0^2 - \varepsilon^{-1} + {A_0}^{-1}\big[x_1 \cos(\omega t + \phi_0) + \\
&\quad + y_1 \sin(\omega t + \phi_0)\big] \\
d_t x_1 &= -2(x_1^2 + y_1^2)y_1 - y_2 - A_0 \sin(\omega t + \phi_0) \\
d_t y_1 &= 2(x_1^2 + y_1^2)x_1 + x_2 + A_0 \cos(\omega t + \phi_0) \\
d_t x_j &= -2(x_j^2 + y_j^2)y_j - y_{j-1} - y_{j+1} \qquad j \geq 2 \\
d_t y_j &= 2(x_j^2 + y_j^2)x_j + x_{j-1} + x_{j+1} \qquad j \geq 2\ .
\end{aligned} \tag{4.4}$$

By writing the DNLSE in this fashion, one separates the lattice wave-function between the breather in polar coordinates and the background sites in Cartesian coordinates. At this stage, it is important to remember the findings presented in Figure 2.4 , where one could clearly see that that the background thermalises to a common frequency with roughly the same size of fluctuations. This justifies the choice of the hybrid polar-Cartesian basis. Remarkably enough, the mass of the breather was very stable around the initial value $|z_0(0)|^2$, and its frequency was very slightly fluctuating around $2|z_0(0)|^2$. This in turn, justifies the choice of the definition of the smallness parameter. The only sites that have frequency statistics different from the background are the nearest neighbours of the breather, which, as it will emerge later in this chapter, contain rapidly oscillating components at low orders in their asymptotic expansions. The perturbative approach is developed for breathers in contact with backgrounds only on one side and is then extended to the general case when the breather sits at a random lattice site and is perturbed by small excitations arriving from backgrounds on both sides. Figure 2.4 shows that there is a clear separation of time scales due to the much faster oscillation of the breather with respect to its surrounding.

Two time scales appear naturally in the system: a short one of order $\varepsilon = 1/\omega$

associated to the fast rotation of the breather's phase and a "long" one of order $\mathcal{O}(1)$ associated to the chaotic motion of the background. The most appropriate way to handle this kind of problems is to consider multiple time scales by introducing two time variables and thereby by rewriting the time derivative as

$$d_t = \varepsilon^{-1}\partial_{t_1} + \partial_{t_2}\,, \tag{4.5}$$

where t_1 and t_2 represent the fast and slow time scales, respectively [59].

Before proceeding with the formal expansion, it is useful to go back to Eq. (4.4) to estimate the variation of the different variables over a time scale of order ε. It is legitimate to assume that the time dependence of the fields is due to the fast rotation ω and thereby neglect the variation of all the variables appearing in the r.h.s. of the above equations. Upon integrating Eq. (4.4) for a time $\Delta t = \varepsilon$ one obtains

$$\begin{aligned}
\Delta A_0 &\approx -\varepsilon\big[x_1\cos(\omega t+\phi_0) + y_1\sin(\omega t+\phi_0)\big] \\
&= \mathcal{O}(\varepsilon) \\
\Delta\phi_0 &\approx \varepsilon A_0^{-1}\big[x_1\sin(\omega t+\phi_0) - y_1\cos(\omega t+\phi_0)\big] \\
&= \mathcal{O}(\varepsilon^{3/2}) \\
\Delta x_1 &\approx -\varepsilon\big[2(x_1^2+y_1^2)y_1 + y_2\big] + \\
&\quad +\varepsilon A_0\cos(\omega t+\phi_0) \\
&= \mathcal{O}(\varepsilon^{1/2}) \\
\Delta y_1 &\approx \varepsilon\big[2(x_1^2+y_1^2)x_1 + x_2\big] + \\
&\quad +\varepsilon A_0\sin(\omega t+\phi_0) \\
&= \mathcal{O}(\varepsilon^{1/2}) \\
\Delta x_j &\approx \varepsilon\big[-2(x_j^2+y_j^2)y_j - y_{j-1} - y_{j+1}\big] \\
&= \mathcal{O}(\varepsilon) \\
\Delta y_j &\approx \varepsilon\big[2(x_j^2+y_j^2)x_j + x_{j-1} + x_{j+1}\big] \\
&= \mathcal{O}(\varepsilon),
\end{aligned} \tag{4.6}$$

where we have used the definition of the smallness parameter ($\varepsilon \equiv 1/\omega \approx \frac{1}{2A_0^2}$) to determine the order of magnitude of the breather amplitude (i.e. $A_0 = \mathcal{O}(\varepsilon^{-1/2})$).

These results suggest that any asymptotic expansion with respect to ε should include half-integer powers (i.e. it should be done with respect to $\sqrt{\varepsilon}$) and also provide information on where the series should start for each variable. More precisely, we consider a perturbation expansion given by

$$\begin{aligned}
A_0 &\sim \varepsilon^{-1/2} A_0^{[-1]} + \textstyle\sum_{m\geq 2} \varepsilon^{m/2} A_0^{[m]}(t_1, t_2) \\
\phi_0 &\sim \phi_0^{[0]} + \textstyle\sum_{m\geq 3} \varepsilon^{m/2} \phi_0^{[m]}(t_1, t_2) \\
x_1 &\sim x_1^{[0]} + \textstyle\sum_{m\geq 1} \varepsilon^{m/2} x_1^{[m]}(t_1, t_2) \\
y_1 &\sim y_1^{[0]} + \textstyle\sum_{m\geq 1} \varepsilon^{m/2} y_1^{[m]}(t_1, t_2) \\
x_{j\geq 2} &\sim x_j^{[0]} + \textstyle\sum_{m\geq 2} \varepsilon^{m/2} x_j^{[m]}(t_1, t_2) \\
y_{j\geq 2} &\sim y_j^{[0]} + \textstyle\sum_{m\geq 2} \varepsilon^{m/2} y_j^{[m]}(t_1, t_2)\,.
\end{aligned} \tag{4.7}$$

This perturbation is singular, since it includes the diverging term $\varepsilon^{-1/2} A_0^{[-1]}(t_2)$. This follows from our initial assumption of dealing with tall breathers.

By inserting the power expansion (4.7) into Eq. (4.4) and by a further Taylor expansion of the sinusoidal functions, we are able to split each equation into a series of separate conditions for the different powers of $\sqrt{\varepsilon}$. Our target is to quantify the weak coupling between the breather and its surroundings, by looking for the first term in the expansion of the breather amplitude which does not average to zero over one full rotation. Finding an analytical expression for this term would not only quantify the order of magnitude of the slow derivative, but it would also provide an upper bound of diffusive processes and characterise the size and nature of the breather 'tails' in the presence of large backgrounds. The pinned breather is extremely localised and only the nearest neighbour contributes directly to the slow drifts of the breather mass.
At lowest order of $\sqrt{\varepsilon}$ for each differential equation, we find:

$$
\begin{aligned}
\partial_{t_1} A_0^{[-1]} &= 0 \\
\partial_{t_2} A_0^{[-1]} &= 0 \\
\partial_{t_1} \phi_0^{[0]} &= -1 + 2(A_0^{[-1]})^2 \\
\partial_{t_2} \phi_0^{[0]} &= 0 \\
\partial_{t_1} x_j^{[0]} &= 0 \qquad j \geq 1 \\
\partial_{t_1} y_j^{[0]} &= 0 \qquad j \geq 1 \, .
\end{aligned}
\tag{4.8}
$$

The first two equations show that $A_0^{[-1]}$ is a constant. With our initial choice $A_0^{[-1]} = 1/\sqrt{2}$, it turns out that $\phi_0^{[0]}$ is a constant as well. The last couple of equations tell us that the leading contributions of the background variables are slow for all sites with $j \neq 0$.

Repeating this algorithm for higher orders, one can write the following system of differential equations

At order $\varepsilon^{-1/2}$ we find:

$$
\begin{aligned}
\partial_{t_1} x_1^{[1]} &= -A_0^{[-1]} \sin(t_1 + \phi_0^{[0]}) \\
\partial_{t_1} y_1^{[1]} &= +A_0^{[-1]} \cos(t_1 + \phi_0^{[0]}) \, .
\end{aligned}
\tag{4.9}
$$

At order 1 we find:

$$
\begin{aligned}
\partial_{t_1} A_0^{[2]} &= x_1^{[0]} \sin(t_1 + \phi_0^{[0]}) - \\
&\quad - y_1^{[0]} \cos(t_1 + \phi_0^{[0]}) \\
\partial_{t_2} x_1^{[0]} + \partial_{t_1} x_1^{[2]} &= -2 y_1^{[0]} ({x_1^{[0]}}^2 + {y_1^{[0]}}^2) - y_2^{[0]} \\
\partial_{t_2} y_1^{[0]} + \partial_{t_1} y_1^{[2]} &= +2 x_1^{[0]} ({x_1^{[0]}}^2 + {y_1^{[0]}}^2) + x_2^{[0]} \\
\partial_{t_2} x_j^{[0]} + \partial_{t_1} x_j^{[2]} &= -2 y_j^{[0]} ({x_j^{[0]}}^2 + {y_j^{[0]}}^2) - \\
&\quad - y_{j-1}^{[0]} - y_{j+1}^{[0]} \qquad \forall j \geq 2 \\
\partial_{t_2} y_j^{[0]} + \partial_{t_1} y_j^{[2]} &= +2 x_j^{[0]} ({x_j^{[0]}}^2 + {y_j^{[0]}}^2) + \\
&\quad + x_{j-1}^{[0]} + x_{j+1}^{[0]} \qquad \forall j \geq 2 \, .
\end{aligned}
\tag{4.10}
$$

At order $\varepsilon^{1/2}$ we find:

$$\begin{aligned}
\partial_{t_1} A_0^{[3]} &= x_1^{[1]} \sin(t_1 + \phi_0^{[0]}) - \\
&\quad - y_1^{[1]} \cos(t_1 + \phi_0^{[0]}) \\
\partial_{t_1} \phi_0^{[3]} &= 4 A_0^{[2]} A_0^{[-1]} + \\
&\quad \left[x_1^{[0]} \cos(t_1 + \phi_0^{[0]}) + \right. \\
&\quad \left. + y_1^{[0]} \sin(t_1 + \phi_0^{[0]}) \right] / A_0^{[-1]} \\
\partial_{t_2} x_1^{[1]} + \partial_{t_1} x_1^{[3]} &= -2[2 x_1^{[0]} y_1^{[0]} x_1^{[1]} + ({x_1^{[0]}}^2 + 3 {y_1^{[0]}}^2) y_1^{[1]}] \\
\partial_{t_2} y_1^{[1]} + \partial_{t_1} y_1^{[3]} &= +2[(3 {x_1^{[0]}}^2 + {y_1^{[0]}}^2) x_1^{[1]} + 2 x_1^{[0]} y_1^{[0]} y_1^{(1)}] \, .
\end{aligned} \tag{4.11}$$

At order ε we find:

$$\begin{aligned}
\partial_{t_2} A_0^{[2]} + \partial_{t_1} A_0^{[4]} &= x_1^{[2]} \sin(t_1 + \phi_0^{[0]}) - \\
&\quad - y_1^{[2]} \cos(t_1 + \phi_0^{[0]}) \\
\partial_{t_1} \phi_0^{[4]} &= \left[x_1^{[1]} \cos(t_1 + \phi_0^{[0]}) + \right. \\
&\quad \left. + y_1^{[1]} \sin(t_1 + \phi_0^{[0]}) \right] / A_0^{[-1]} \\
\partial_{t_2} x_1^{[2]} + \partial_{t_1} x_1^{[4]} &= -2 {x_1^{[1]}}^2 y_1^{[0]} - 4 x_1^{[0]} x_1^{[2]} y_1^{[0]} - \\
&\quad - 4 x_1^{[0]} x_1^{[1]} y_1^{[1]} - 6 y_1^{[0]} {y_1^{[1]}}^2 - \\
&\quad - 2 {x_1^{[0]}}^2 y_1^{[2]} - 6 {y_1^{[0]}}^2 y_1^{[2]} - y_2^{[2]} - \\
&\quad - A_0^{[-1]} \phi_0^{[3]} \cos(t_1 + \phi_0^{[0]}) - \\
&\quad - A_0^{[2]} \sin(t_1 + \phi_0^{[0]}) \\
\partial_{t_2} y_1^{[2]} + \partial_{t_1} y_1^{[4]} &= 6 x_1^{[0]} {x_1^{[1]}}^2 + 6 {x_1^{[0]}}^2 x_1^{[2]} + x_2^{[2]} + \\
&\quad + 2 x_1^{[2]} {y_1^{[0]}}^2 + 4 x_1^{[1]} y_1^{[0]} y_1^{[1]} + \\
&\quad + 2 x_1^{[0]} {y_1^{[1]}}^2 + 4 x_1^{[0]} y_1^{[0]} y_1^{[2]} + \\
&\quad + A_0^{[2]} \cos(t_1 + \phi_0^{[0]}) - \\
&\quad - A_0^{[-1]} \phi_0^{[3]} \sin(t_1 + \phi_0^{[0]}) \, .
\end{aligned} \tag{4.12}$$

At order $\varepsilon^{3/2}$ we find:

$$\begin{aligned}\partial_{t_2} A_0^{[3]} + \partial_{t_1} A_0^{[5]} &= \phi_0^{[3]} x_1^{[0]} \cos(t_1 + \phi_0^{[0]}) - \\ &\quad - y_1^{[3]} \cos(t_1 + \phi_0^{[0]}) + \\ &\quad + x_1^{[3]} \sin(t_1 + \phi_0^{[0]}) + \\ &\quad + \phi_0^{[3]} y_1^{[0]} \sin(t_1 + \phi_0^{[0]}) \, .\end{aligned} \tag{4.13}$$

Finally, at order ε^2 we find:

$$\begin{aligned}\partial_{t_2} A_0^{[4]} + \partial_{t_1} A_0^{[6]} &= \phi_0^{[4]} x_1^{[0]} \cos(t_1 + \phi_0^{[0]}) + \\ &\quad + \phi_0^{[3]} x_1^{[1]} \cos(t_1 + \phi_0^{[0]}) - \\ &\quad - y_1^{[4]} \cos(t_1 + \phi_0^{[0]}) + \\ &\quad + x_1^{[4]} \sin(t_1 + \phi_0^{[0]}) + \\ &\quad + \phi_0^{[4]} y_1^{[0]} \sin(t_1 + \phi_0^{[0]}) + \\ &\quad + \phi_0^{[3]} y_1^{[1]} \sin(t_1 + \phi_0^{[0]}) \, .\end{aligned} \tag{4.14}$$

We will see that the first order at which the breather derivative does not average to zero is $\mathcal{O}(\varepsilon^2)$. In order to prove this fact, one must solve the coupled differential equations for all orders lower than ε and determine the corresponding expressions of the expansion terms.

At order $\mathcal{O}(1)$ (4.10), one can recognize the DNLSE on the right hand side. Using both the previous findings from partial averaging and the clear background breather separation observed in the numerics from plots in Figures 2.4 and 2.5, one can make the assumption that at this order, the background and the breather are completely decoupled. This assumption, together with the equations from (4.10) implies that $\partial_{t_1} x_1^{[2]} = \partial_{t_1} y_1^{[2]} = 0$. In other words, $x_1^{[2]}$ and $y_1^{[2]}$ are slow functions of time.

For generic sites, (4.10) at order 1 reduces to:

$$\begin{aligned} \partial_{t_2} x_j^{[0]} &= -2y_j^{[0]}({x_j^{[0]}}^2 + {y_j^{[0]}}^2) - \\ &\quad -y_{j-1}^{[0]} - y_{j+1}^{[0]} \\ \partial_{t_2} y_j^{[0]} &= +2x_j^{[0]}({x_j^{[0]}}^2 + {y_j^{[0]}}^2) + \\ &\quad +x_{j-1}^{[0]} + x_{j+1}^{[0]} \end{aligned} \tag{4.15}$$

where one has used that $x_j^{[2]}$ and $y_j^{[2]}$ are slow variables, from identical considerations to the one stated for the nearest neighbour. The fact that $x_j^{[2]}$ and $y_j^{[2]}$ are slow functions will be used extensively while performing averaging later in this chapter.

4.1.2 Decoupling due to the separation of time scales

Let us now study whether at order $\mathcal{O}(1)$, the breather and the background are decoupled for time spans of one breather rotation. If this is true, at zero-th order (i.e. $\mathcal{O}(\varepsilon^0)$), breathers can be replaced by pinned vacancies that act on the background as reflective boundaries. This means that the evolution of all zero-order terms $\left\{(x_j^{[0]}, y_j^{[0]})\right\}$ is independent of the evolution of the breather for all $j \neq 0$. This vacancy-breather analogy is confirmed by the simulations presented in Figure 4.1, where one can see that the background follows similar trajectories in the cases when at site $j = 0$ there is either a tall pinned breather or a reflective boundary. The differential equation for the background becomes:

$$i\partial_{t_2} z_{j\neq 0}^{[0]} = -2\left|z_j^{[0]}\right|^2 z_j^{[0]} - z_{j-1}^{[0]} - z_{j+1}^{[0]} \tag{4.16}$$

where $z_0^{[0]} \equiv 0$ is a reflective boundary. Figure 4.1 shows how the amplitude of the zero-order wave-function for the nearest neighbour of the breather obtained from Eq. (4.16) compares with that of the full solution of Eq. (4.1)). The slow function approximates the full trajectory very well for several hundred breather periods. After a while, the two trajectories separate due to the chaotic nature of the DNLSE. The reflective boundary

approximation becomes even more accurate when the size of the breather is increased, bounding the two trajectories close together for much longer times than those shown in Figure 4.1.

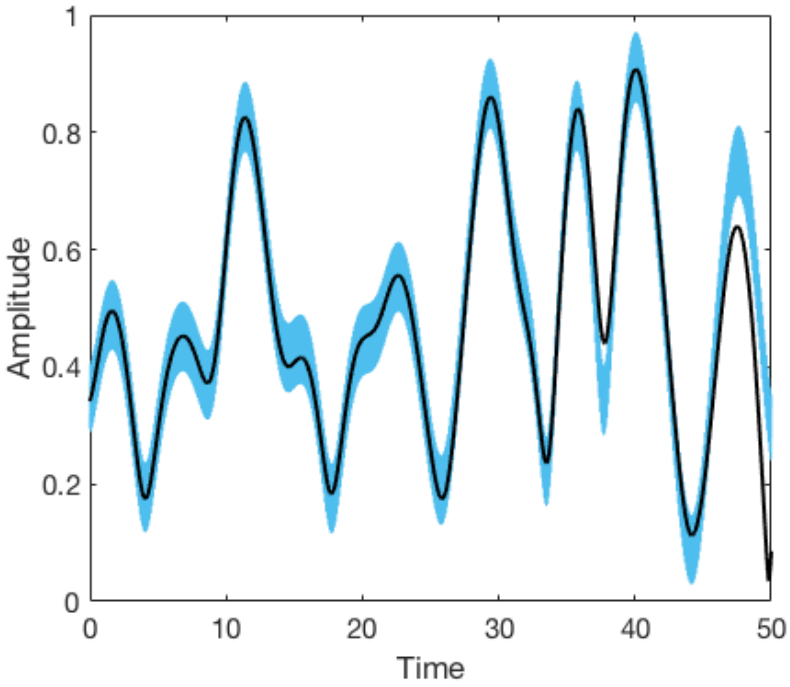

Figure 4.1: Time evolution of the amplitude of the nearest neighbour on the right of the breather obtained by integrating the DNLSE Eq. (4.1) (light blue strip) and from the zero-order reduced equation (4.16) (black line). Replacing the breather with a reflective boundary produces a similar dynamics of the background. The breather had an initial amplitude of $|z_0| = 6$ and sat in the middle of a 15 sites lattice which was thermalised at infinite temperature and had the average occupation number $\langle |z_j|^2 \rangle = 0.5$. Analogous decouplings occur for both the left and the right neighbours.

Backgrounds characterised by low temperatures tend to be less chaotic and therefore, in their presence, this breather/vacancy analogy is satisfied over significantly longer time-scales. It is however worth noting that even for high-temperature backgrounds, one can still obtain results for the breather fluctuations and for the background dynamics similar to those of Figure 4.1 when using the simplified equation (4.16). As will be later seen in this thesis, one can build a decoupling theory which is valid for times far longer than the separation time seen in Figure 4.1, since it is possible to

express the fluctuations in the breather size as a function of the zero-order background at any given time, regardless of what the initial condition is. In order to build this theory however, it is crucial to use the adiabatic decoupling between the zero-order wave-function of the background and the breather oscillations.

This type of decoupling is also addressed in [70] where it is shown that breathers induce weakly non-ergodic dynamics. These localised solutions split the lattice into mutually disconnected regions, thermalised at different chemical potentials and different temperatures.

A clear evidence for the separation of the two time scales is also presented in Figure 2.6. There, one can see that the background evolves over time scales of $\mathcal{O}(10)$, while the breather height is effectively frozen over scales of this magnitude. In addition, the sites in the background frequently reach amplitudes which are close to zero, even if their overall size is of order $\mathcal{O}(1)$. This provides an additional justification for the choice of a hybrid polar-Cartesian system, which was introduced to avoid diverging derivatives for small values of the background amplitudes. From Figure 2.6 one sees that the first neighbour (red line) displays a fast component of oscillation that comes from the breather. This component originates in the first non-trivial terms identified in Eq. (4.17). Note that the breather amplitude does not display any visible variations during times which characterise the evolution of the slow background.

This assumption will be later confirmed by additional numerical tests and it will prove very powerful when trying to find the first non-zero derivative after averaging.

4.2 First Non-Trivial Terms in The Perturbative Calculation

The differential equations at specified orders of the perturbation need to be integrated to obtain the dynamical expressions of the perturbative terms. In doing this, slow terms appear as integration constants. The solvability condition is then imposed

by the requirements that the energy and the norm have to remain conserved at any given order of the perturbation.

We have seen above how to obtain non-trivial differential equations for the breather and its nearest neighbour. By integrating the first non-zero terms for the breather amplitude and its nearest neighbours from Eqs. (4.9)-(4.10) and by making use of the fact that the background is slow and $A_0^{[-1]}$ and $\phi_0^{[0]}$ are constants, we obtain,

$$\begin{aligned} A_0^{[2]} &= -x_1^{[0]}\cos(t_1+\phi_0^{[0]}) - y_1^{[0]}\sin(t_1+\phi_0^{[0]}) + \\ &\quad + C_1(t_2) \\ x_1^{[1]} &= A_0^{[-1]}\cos(t_1+\phi_0^{[0]}) + C_2(t_2) \\ y_1^{[1]} &= A_0^{[-1]}\sin(t_1+\phi_0^{[0]}) + C_3(t_2) \end{aligned} \tag{4.17}$$

where $C_1(t_2)$, $C_2(t_2)$ and $C_3(t_2)$ are slow functions to be determined.

Meanwhile, we know that the Hamiltonian of the system is, at order $O(\varepsilon^{-1/2})$,

$$\begin{aligned} H_{O(1/\sqrt{\varepsilon})} &= \sqrt{2}\big[A_0^{[2]} + x_1^{[0]}\cos(t_1+\phi_0^{[0]}) + \\ &\quad + y_1^{[0]}\sin(t_1+\phi_0^{[0]})\big] \end{aligned} \tag{4.18}$$

where we have made use of the equality $A_0^{[-1]} = 1/\sqrt{2}$.

Upon substituting the analytical expression for $A_0^{[2]}$ in (4.17) one obtains:

$$H_{O(1/\sqrt{\varepsilon})} = \sqrt{2}C_1(t_2) \tag{4.19}$$

which requires C_1 to be constant to guarantee that the Hamiltonian is conserved. This constant is zero, since any other value would induce secular terms when integrating higher order terms.

By imposing the conservation of norm at order $\sqrt{\varepsilon}$ we obtain the additional constraint:

$$x_1^{[0]}C_2(t_2) + y_1^{[0]}C_3(t_2) = 0\,. \tag{4.20}$$

Therefore the two unknown slow functions must satisfy:

$$\begin{aligned} C_2(t_2) &= -Ky_1^{[0]} \\ C_3(t_2) &= Kx_1^{[0]} \end{aligned} \tag{4.21}$$

where K is a real number to be determined.

The differential equation for x_1 at order $\mathcal{O}(\varepsilon^{1/2})$ reads

$$\begin{aligned} \partial_{t_1} x_1^{[3]} + \partial_{t_2} x_1^{[1]} = -2(x_1^{[0]} x_1^{[1]} y_1^{[0]} + \\ + {x_1^{[0]}}^2 y_1^{[1]} + 3{y_1^{[0]}}^2 y_1^{[1]}). \end{aligned} \tag{4.22}$$

Replacing $x_1^{[1]}$ and $y_1^{[1]}$ with their analytical expressions from (4.17) one arrives at

$$\begin{aligned} \partial_{t_1} x_1^{[3]} + \partial_{t_2} C_2 = \\ = -2[x_1^{[0]} y_1^{[0]} (A_0^{[-1]} \cos(t_1 + \phi_0^{[0]}) + C_2) + \\ + ({x_1^{[0]}}^2 + 3{y_1^{[0]}}^2)(A_0^{[-1]} \sin(t_1 + \phi_0^{[0]}) + C_3)]. \end{aligned} \tag{4.23}$$

From this it follows that the most general form that $x_1^{[3]}$ can have is $D_1(t_2) + D_2(t_2) \times t_1 + D_3(t_2)\sin(t_1 + \phi_0^{[0]}) + D_4(t_2)\cos(t_1 + \phi_0^{[0]})$. The Hamiltonian at order $\mathcal{O}(\varepsilon)$ contains terms of the sort $A_0^{[-1]} x_1^{[3]} \cos(t_1 + \phi_0^{[0]})$ and $A_0^{[-1]} y_1^{[3]} \sin(t_1 + \phi_0^{[0]})$ in addition to a plethora of terms which can all be written as $B_1(t_2) + B_2(t_2)\sin(t_1 + \phi_0^{[0]}) + B_3(t_2)\cos(t_1 + \phi_0^{[0]}) + \texttt{high harmonics}$. This implies that the Ansätze of $x_1^{[3]}$ and $y_1^{[3]}$ are of the type $B_1(t_2) + B_2(t_2)\sin(t_1 + \phi_0^{[0]}) + B_3(t_2)\cos(t_1 + \phi_0^{[0]})$, which means that $D_2(t_2) = 0$. Isolating only the slow terms of equation (2) one arrives at

$$\begin{aligned} \partial_{t_2} C_2(t_2) = -2\Big[2x_1^{[0]} y_1^{[0]} C_2(t_2) + \\ + C_3(t_2)\big({x_1^{[0]}}^2 + 3{y_1^{[0]}}^2\big)\Big]. \end{aligned} \tag{4.24}$$

Using the constraint (4.21) and making all possible simplifications leads to:

$$Kx_2^{[0]} = 0 \tag{4.25}$$

which implies that K must be zero for extended lattices where $x_2^{[0]} \neq 0$. The slow terms that appear from the integration over the fast time scale are all zero, i.e. $C_1(t_2) = C_2(t_2) = C_3(t_2) = 0$ so that, Eq. (4.17) reduces to

$$\begin{aligned} A_0^{[2]} &= -x_1^{[0]} \cos(t_1 + \phi_0^{[0]}) - y_1^{[0]} \sin(t_1 + \phi_0^{[0]}) \\ x_1^{[1]} &= A_0^{[-1]} \cos(t_1 + \phi_0^{[0]}) \\ y_1^{[1]} &= A_0^{[-1]} \sin(t_1 + \phi_0^{[0]}) \, . \end{aligned} \tag{4.26}$$

By using these solutions, it becomes apparent that the second equation in (4.12) simplifies to $\partial_{t_1} \phi_0^{[4]} = 1$. This fast term appears because in the differential equation of the slow phase there is the term $2A_0^2 - \omega$ which has a first non-zero component at order ε.

The expressions (4.26) can now be averaged over one full rotation by making use of the fact that $x_1^{[0]}$ and $y_1^{[0]}$ are slow and that $A_0^{[-1]}$ is time-independent,

$$\begin{aligned} \int_0^{2\pi} dt_1 A_0^{[2]} &= 0 \\ \int_0^{2\pi} dt_1 x_1^{[1]} &= 0 \\ \int_0^{2\pi} dt_1 y_1^{[1]} &= 0. \end{aligned} \tag{4.27}$$

Therefore, the first non-trivial terms are zero when averaged over one full rotation for both the breather and its nearest neighbour. In order to quantify the coupling between breather and background, one is therefore forced to continue the perturbative analysis to higher orders as shown below.

4.3 Higher Order Terms in the Perturbative Calculation

At order $\mathcal{O}(\varepsilon^{1/2})$ Eq. (4.11) for the breather norm states

$$\partial_{t_1} A_0^{[3]} = x_1^{[1]} \sin(t_1 + \phi_0^{[0]}) - y_1^{[1]} \cos(t_1 + \phi_0^{[0]}). \tag{4.28}$$

By using the findings of Eq. (4.26) and by substituting $x_1^{[1]}$ and $y_1^{[1]}$, one arrives at $\partial_{t_1} A_0^{[3]}$=0. Therefore $A_0^{[3]}$ is a slow function of the type:

$$A_0^{[3]} = C_4(t_2). \tag{4.29}$$

The Hamiltonian of the system at order $O(1)$ is the Hamiltonian of the zero order wave-function plus the contribution of $4A_0^{[3]} {A_0^{[-1]}}^3$. Therefore

$$A_0^{[3]} = 0 \tag{4.30}$$

which naturally averages to zero over one full rotation as well. It now follows that we must go to even higher orders to obtain a slow drift in the breather norm.

The Bose-Hubbard Hamiltonian at order $\mathcal{O}(\varepsilon^{1/2})$ is

$$\begin{aligned} H_{BH}^{[1]} &= 4\Big({x_1^{[0]}}^2 + {x_1^{[0]}}^2\Big)(x_1^{[0]} x_1^{[1]} + y_1^{[0]} y_1^{[1]}) + \\ &\quad + 2A_0^{[-1]}(x_1^{[2]} \cos(t_1 + \phi_0^{[0]}) + y_1^{[2]} \sin(t_1 + \phi_0^{[0]})) + \\ &\quad + 2(x_1^{[1]} x_2^{[0]} + y_1^{[1]} y_2^{[0]}) + 4{A_0^{[-1]}}^3 A_0^{[4]}, \end{aligned} \tag{4.31}$$

and therefore this must be a conserved quantity. Making use of the analytical expressions for $x_1^{[1]}$ and $y_1^{[1]}$ from (4.26), and of the fact that $x_2^{[2]}$ and $y_2^{[2]}$ are slow functions we can write this as

$$M(t_2) \cos(t_1 + \phi_0^{[0]}) + N(t_2) \sin(t_1 + \phi_0^{[0]}) + A_0^{[4]} = \texttt{constant} \tag{4.32}$$

where M and N are slow functions of t_2. It immediately follows that the Ansatz for

$A_0^{[4]}$ is $\texttt{constant} - M(t_2)\cos(t_1+\phi_0^{[0]}) - N(t_2)\sin(t_1+\phi_0^{[0]})$. The constant in this Ansatz must be zero, otherwise secular terms would be introduced into the system. Therefore

$$A_0^{[4]} = M(t_2)\cos(t_1+\phi_0^{[0]}) + N(t_2)\sin(t_1+\phi_0^{[0]}), \tag{4.33}$$

where M and N are unknown slow functions. Regardless of their expressions, we can immediately see that when averaged over one rotation, $A_0^{[4]}$ still averages to zero. Therefore we must go to higher orders still.

At order $\mathcal{O}(\varepsilon)$ Eq. (4.12) for the breather norm states

$$\partial_{t_2} A_0^{[2]} + \partial_{t_1} A_0^{[4]} = x_1^{[2]}\sin(t_1+\phi_0^{[0]}) - y_1^{[2]}\cos(t_1+\phi_0^{[0]}) \tag{4.34}$$

and we now have a clear analytical expression for $A_0^{[2]}$ at (4.26) and in addition we possess the knowledge that $x_1^{[2]}$ and $y_1^{[2]}$ are slow functions (they do not depend on t_1, but only on t_2), and we have an Ansatz for $A_0^{[4]}$ (4.33). Using all this information, we can find the following expressions for the expansions at order $\mathcal{O}(\varepsilon)$ at the nearest neighbour

$$\begin{aligned} x_1^{[2]} &= -\partial_{t_2} y_1^{[0]} + M \\ y_1^{[2]} &= \partial_{t_2} x_1^{[0]} + N; \end{aligned} \tag{4.35}$$

where $\partial_{t_2} x_1^{[0]}$ and $\partial_{t_2} y_1^{[0]}$ are the DNLSE derivatives of the zero order wave-function (of the form (4.15)).

It is now appropriate to move to the breather phase, and look at the equations from (4.11) and (4.12) which, for the phase dictate that

$$\begin{aligned} \partial_{t_1}\phi_0^{[3]} &= 4A_0^{[2]}A_0^{[-1]} + \\ &\quad \big[x_1^{[0]}\cos(t_1+\phi_0^{[0]}) + \\ &\quad + y_1^{[0]}\sin(t_1+\phi_0^{[0]})\big]/A_0^{[-1]} \\ \partial_{t_1}\phi_0^{[4]} &= \big[x_1^{[1]}\cos(t_1+\phi_0^{[0]}) + \\ &\quad + y_1^{[1]}\sin(t_1+\phi_0^{[0]})\big]/A_0^{[-1]}. \end{aligned} \tag{4.36}$$

All the terms on the right hand side now have known analytical expressions. After making all the possible simplifications these two equations can be solved to obtain

$$\begin{aligned} \phi_0^{[3]} &= \Big(4A_0^{[-1]} - \tfrac{1}{A_0^{[-1]}}\Big)[-x_1^{[0]}\sin(t_1+\phi_0^{[0]}) \\ &\quad +y_1^{[0]}\cos(t_1+\phi_0^{[0]})] + P(t_2) \\ \phi_0^{[4]} &= t_1 + Q(t_2) \end{aligned} \tag{4.37}$$

where $P(t_2)$ and $Q(t_2)$ are slow functions.

Under the assumption that the zero-order wave-function for the background obeys the DNLSE, one can deduce from (4.15) that

$$\begin{aligned} x_1^{[2]} &= -\partial_{t_2} y_1^{[0]} + M, \\ y_1^{[2]} &= \partial_{t_2} x_1^{[0]} + N \end{aligned} \tag{4.38}$$

where M and N are slow functions. At this stage of the procedure, it is possible to solve all equations from (4.11) and (4.12) and find the analytical expressions of $\phi_0^{[3]}$, $A_0^{[4]}$ and $\phi_0^{[4]}$.

Finally one can determine $x_1^{[3]}$, $y_1^{[3]}$ and $A_0^{[5]}$ up to a slow component from the equations at (4.11) and (4.13)

$$\begin{aligned} x_1^{[3]} &= +2\big({x_1^{[0]}}^2 + 3{y_1^{[0]}}^2\big)A_0^{[-1]}\cos(t_1+\phi_0^{[0]}) \\ &\quad -4x_1^{[0]}y_1^{[0]}A_0^{[-1]}\sin(t_1+\phi_0^{[0]}) + R(t_2) \\ y_1^{[3]} &= +2\big(3{x_1^{[0]}}^2 + {y_1^{[0]}}^2\big)A_0^{[-1]}\sin(t_1+\phi_0^{[0]}) \\ &\quad -4x_1^{[0]}y_1^{[0]}A_0^{[-1]}\cos(t_1+\phi_0^{[0]}) + S(t_2) \\ A_0^{[5]} &= -(R+Py_1^{[0]})\cos(t_1+\phi_0^{[0]}) + \\ &\quad +\tfrac{(-1+8{A_0^{[-1]}}^2)({x_1^{[0]}}^2-{y_1^{[0]}}^2)}{2A_0^{[-1]}}\cos^2(t_1+\phi_0^{[0]}) + \\ &\quad +(Px_1^{[0]}-S)\sin(t_1+\phi_0^{[0]}) - \tfrac{x_1^{[0]}y_1^{[0]}}{2A_0^{[-1]}}\sin[2(t_1+\phi_0^{[0]})] + \\ &\quad +4A_0^{[-1]}x_1^{[0]}y_1^{[0]}\sin[2(t_1+\phi_0^{[0]})] + U(t_2) \end{aligned} \tag{4.39}$$

where $R(t_2)$, $S(t_2)$ and $U(t_2)$ are slow functions of time.

Looking at the norm at order $\mathcal{O}(\varepsilon^{3/2})$ one can see terms of the type $A_0^{[-1]}A_0^{[4]}$, $x_j^{[0]}x_j^{[3]}$ and $y_j^{[0]}y_j^{[3]}$. We now know that $A_0^{[-1]}A_0^{[4]}$ consists of the sum of two fast sinusoidals, and that no slow terms are present there. We also have for $j \geq 2$ that $\partial_{t_1} x_j^{[3]} = \partial_{t_1} y_j^{[3]} = 0$. Closing the solvability condition at this order of the norm would lead to analytical expressions for M and N, but we are not interested in this, since, as will later become apparent, these terms cancel, and their exact analytical expressions are not relevant. Also, to close the solvability conditions for the slow parts, the most elegant approach is to assume that $R = S = 0$, and $x_j^{[3]} = y_j^{[3]} = 0$ for all $j \geq 2$. Without making this assumption, one would arrive at a final expression for the non zero derivative which contains denominators (which diverge). There is no way to know this a priori to finalising the calculation. If one adds these terms in `Mathematica` a posteriori, one can observe the divergences.

With this in mind, we can further simplify the expressions from (4.39) to

$$\begin{aligned}
x_1^{[3]} &= +2\big({x_1^{[0]}}^2 + 3{y_1^{[0]}}^2\big)A_0^{[-1]}\cos(t_1+\phi_0^{[0]}) \\
&\quad -4x_1^{[0]}y_1^{[0]}A_0^{[-1]}\sin(t_1+\phi_0^{[0]}) \\
y_1^{[3]} &= +2\big(3{x_1^{[0]}}^2 + {y_1^{[0]}}^2\big)A_0^{[-1]}\sin(t_1+\phi_0^{[0]}) \\
&\quad -4x_1^{[0]}y_1^{[0]}A_0^{[-1]}\cos(t_1+\phi_0^{[0]}) \\
A_0^{[5]} &= \tfrac{1}{A_0^{[-1]}}\Big\{\tfrac{(-1+8{A_0^{[-1]}}^2)}{4}({x_1^{[0]}}^2 - {y_1^{[0]}}^2)\cos\big[2(t_1+\phi_0^{[0]})\big] + \\
&\quad A_0^{[-1]}Px_1^{[0]}\sin(t_1+\phi_0^{[0]}) - A_0^{[-1]}Py_1^{[0]}\cos(t_1+\phi_0^{[0]}) + \\
&\quad x_1^{[0]}y_1^{[0]}\big(-1+8{A_0^{[-1]}}^2\big)\sin(t_1+\phi_0^{[0]})\cos(t_1+\phi_0^{[0]})\Big\} + \\
&\quad +U(t_2)
\end{aligned} \tag{4.40}$$

where $U(t_2)$ is an unknown function of time.

It is also useful to notice here, that when one substitutes all the higher order functions on the right hand side of equation (4.13), one arrives to

$$\partial_{t_2} A_0^{[3]} + \partial_{t_1} A_0^{[5]} = 0 \tag{4.41}$$

which means that even if $A_0^{[5]}$ seems to have non zero terms when averaging over one full rotation, the derivative for the breather norm at order $\mathcal{O}(\varepsilon^{3/2})$ is still zero. Let us proceed to do the same type of substitution for the derivative at (4.14) to see what the average drift is at $\mathcal{O}(\varepsilon^2)$.

4.4 Derivative at order $\mathcal{O}(\varepsilon^2)$

Let us now introduce the notation

$$D_{\varepsilon^2}^A \equiv \partial_{t_2} A_0^{[4]} + \partial_{t_1} A_0^{[6]}. \tag{4.42}$$

This is the lowest-order term providing an average non-zero slow contribution to the evolution of the breather mass, as it will soon become apparent. With the help of Eq. (4.14), replacing all the known functions with their explicit expressions, and after averaging over one fast rotation (i.e. taking $\langle * \rangle \equiv \frac{1}{2\pi}\int_0^{2\pi}(*)dt_1$) we arrive at,

$$\begin{aligned}\langle D_{\varepsilon^2}^A \rangle = x_1^{[0]}\sin(\phi_0^{[0]}) - y_1^{[0]}\cos(\phi_0^{[0]}) + P(t_2) - \\ -\langle y_1^{[4]}\cos(t_1+\phi_0^{[0]})\rangle + \langle x_1^{[4]}\sin(t_1+\phi_0^{[0]})\rangle\end{aligned} \tag{4.43}$$

where $P(t_2)$ is one of the unknown slow functions in the expression of $\phi_0^{[3]}$ in Eq. (4.39) and $x_1^{[4]}$, $y_1^{[4]}$ are unknown high order terms for the wave-function of the nearest neighbour.

It is now useful to express $\langle y_1^{[4]}\cos(t_1+\phi_0^{[0]})\rangle$ and $\langle x_1^{[4]}\sin(t_1+\phi_0^{[0]})\rangle$ as functions of the zero-order wave-function and of the five unknown slow terms: $x_2^{[2]}$, $y_2^{[2]}$, $M(t_2)$, $N(t_2)$ and $P(t_2)$.

From the expansion of the DNLSE at site $j=1$, we write the differential equation

for the derivative of x_1 at order ε:

$$\begin{aligned}\partial_{t_1} x_1^{[4]} + \partial_{t_2} x_1^{[2]} &= -2{x_1^{[1]}}^2 y_1^{[0]} - 4x_1^{[0]} x_1^{[2]} y_1^{[0]} - \\ &\quad -4x_1^{[0]} x_1^{[1]} y_1^{[1]} - 6y_1^{[0]} {y_1^{[1]}}^2 - \\ &\quad -2{x_1^{[0]}}^2 y_1^{[2]} - 6{y_1^{[0]}}^2 y_1^{[2]} - \\ &\quad -A_0^{[-1]} \phi_0^{[3]} \cos(t_1 + \phi_0^{[0]}) - \\ &\quad -A_0^{[2]} \sin(t_1 + \phi_0^{[0]}) - y_2^{[2]}.\end{aligned} \tag{4.44}$$

At this stage, one can replace all the known terms on the right hand side with their expressions from (4.39) and make all possible simplifications. In addition, $\partial_{t_2} x_1^{[2]}$ can be substituted with its analytical expression and moved to the right hand side.

We integrate both sides with respect to the fast time t_1. This leads to an analytical expression for $x_1^{[4]}$ which contains the terms $x_2^{[2]}$, $y_2^{[2]}$, $M(t_2)$, $N(t_2)$ and $P(t_2)$ which are all slow functions. After integrating this equation, one finds that $x_1^{[4]}$ contains terms which are different from the other high order functions of (4.39) because they contain expressions of the type $F(t_2) \times t_1$. These terms appear in the Hamiltonian at order $\varepsilon^{3/2}$, together with the known function $\phi_0^{[4]} = t_1 + Q(t_2)$ and the term $A_0^{[6]}$.

The next required step is to calculate $\langle x_1^{[4]} \sin(t_1 + \phi_0^{[0]}) \rangle$ which again contains the slow terms $x_2^{[2]}$, $y_2^{[2]}$, $M(t_2)$, $N(t_2)$ and $P(t_2)$:

$$\begin{aligned}\langle x_1^{[4]} \sin(t_1 + \phi_0^{[0]}) \rangle &= -\frac{A_0^{[-1]} P}{2} + \\ &+ \Bigg\{ 6{A_0^{[-1]}}^2 y_1^{[0]} + 2 \Bigg[-4y_1^{[0]} ({x_1^{[0]}}^4 + \\ &\quad + x_1^{[0]} x_2^{[0]} + 2{x_1^{[0]}}^2 {y_1^{[0]}}^2 + {y_1^{[0]}}^4) + \\ &\quad + (2{x_1^{[0]}}^2 + {x_2^{[0]}}^2 - 2{y_1^{[0]}}^2) y_2^{[0]} + \\ &\quad + {y_2^{[0]}}^3 \Bigg] + y_2^{[2]} + y_3^{[0]} \Bigg\} \cos(\phi_0^{[0]}).\end{aligned} \tag{4.45}$$

Analogously, one can obtain an expression for $\langle y_1^{[4]} \cos(t_1 + \phi_0^{[0]}) \rangle$, and then express

the average from (4.43) as

$$\begin{aligned}
\langle D^A_{\varepsilon^2} \rangle \;=\; & y_2^{[2]} \cos(\phi_0^{[0]}) - x_2^{[2]} \sin(\phi_0^{[0]}) - \\
& -2{A_2^{[0]}}^3 \sin(\phi_0^{[0]} - \psi_2^{[0]}) + \\
& +A_1^{[0]} \Big[\big(-2 + 8{A_1^{[0]}}^4 \big) \sin(\phi_0^{[0]} - \psi_1^{[0]}) + \\
& +4A_1^{[0]} A_2^{[0]} \sin(\phi_0^{[0]} - 2\psi_1^{[0]} + \psi_2^{[0]}) \Big] \\
& -A_3^{[0]} \sin(\phi_0^{[0]} - \psi_3^{[0]}) \\
& +\partial_{t_2} M(t_2) \cos(\phi_0^{[0]}) + \\
& +\partial_{t_2} N(t_2) \sin(\phi_0^{[0]}) \\
& -2{A_1^{[0]}}^2 \big[N(t_2) \cos(\phi_0^{[0]} - 2\psi_1^{[0]}) + \\
& +M(t_2) \sin(\phi_0^{[0]} - 2\psi_1^{[0]}) \big] \\
& +4{A_1^{[0]}}^2 \big[N(t_2) \cos(\phi_0^{[0]}) - \\
& -M(t_2) \sin(\phi_0^{[0]}) \big].
\end{aligned} \tag{4.46}$$

Here, it was more convenient to express the zero-order wave-functions using polar coordinates via the transformation: $x_j^{[0]} \to A_j^{[0]} \cos(\psi_j^{[0]})$ and $y_j^{[0]} \to A_j^{[0]} \sin(\psi_j^{[0]})$. At this stage it is not obvious at all whether this term is zero or not. In order to simplify this expression, it is crucial to use the solvability conditions, which ensure that the perturbation developed here still conserves mass and energy, since it originates from the Bose-Hubbard Model.

4.5 Fluxes for the Hamiltonian and the Norm at order $\mathcal{O}(\varepsilon)$ for a Bose Hubbard Chain

Let us start by looking at the norm and the Hamiltonian for a one-dimensional Bose-Hubbard chain (denoted by the subscript X_c), given by

$$\begin{aligned} A_c &= \textstyle\sum_{j>1}(x_j^2+y_j^2) \\ H_c &= \textstyle\sum_{j>1}(x_j^2+y_j^2)^2+ \\ &\quad +2\textstyle\sum_{j\geq 1}(x_j x_{j+1}+y_j y_{j+1}) \end{aligned} \tag{4.47}$$

where x_j and y_j obey the general DNLSE (for all sites with $j \geq 2$), just as was initially discussed in (4.4), and have the generic asymptotic expansions $x_j \sim x_j^{[0]} + \varepsilon x_j^{[2]} +$ `H.O.T.` and $y_j \sim y_j^{[0]} + \varepsilon y_j^{[2]} +$ `H.O.T.` from the expressions at (4.7). Note that in the Hamiltonian, there is also a term which couples sites $j = 2$ and $j = 1$, even if site 1 is not part of the chain we study here. This term was included to make sure that after we add the contributions from the dimer, all the required terms are present for the overall system (dimer-chain).

At order [0] these two quantities are simply those corresponding to the Bose Hubbard model for the zero-order wave-function, and therefore are perfectly conserved (together with the contribution from $x_1^{[0]}$ and $y_1^{[0]}$). Remarkably enough, for the chain there are no contributions at all at order 1, therefore the only conservation laws at this order will come from the dimer ($j \in \{0,1\}$) only. The first order at which the conservation law is no longer trivial for the chain is order [2], corresponding to the terms proportional with ε.

It is now useful to identify the contributions at order $\mathcal{O}(\varepsilon)$ for the quantities at

(4.47) after we replace all x_j and y_j with their asymptotic expansions. These are

$$\begin{aligned} A_c^{[2]} &= 2\sum_{j>1}(x_j^{[0]}x_j^{[2]} + y_j^{[0]}y_j^{[2]}) \\ H_c^{[2]} &= 4\sum_{j>1}\left({x_j^{[0]}}^2 + {y_j^{[0]}}^2\right)(x_j^{[0]}x_j^{[2]} + y_j^{[0]}y_j^{[2]}) + \\ &\quad +2\sum_{j\geq 1}(x_j^{[2]}x_{j+1}^{[0]} + x_j^{[0]}x_{j+1}^{[2]} + y_j^{[2]}y_{j+1}^{[0]} + y_j^{[0]}y_{j+1}^{[2]}). \end{aligned} \tag{4.48}$$

If we want the time derivatives (here we refer to the slow time, denoted by t_2) of these two quantities we need all the derivatives for the functions at order [0] and [2]. But the zero order wave function obeys the DNLSE, therefore we will have that

$$\begin{aligned} \partial_{t_2}x_j^{[0]} &= -2y_j^{[0]}({x_j^{[0]}}^2 + {y_j^{[0]}}^2) - \\ &\quad -y_{j-1}^{[0]} - y_{j+1}^{[0]} \\ \partial_{t_2}y_j^{[0]} &= +2x_j^{[0]}({x_j^{[0]}}^2 + {y_j^{[0]}}^2) + \\ &\quad +x_{j-1}^{[0]} + x_{j+1}^{[0]}. \end{aligned} \tag{4.49}$$

Similarly, one can write the expansions for the differential equations at order $\mathcal{O}(\varepsilon)$ to obtain

$$\begin{aligned} \partial_{t_2}x_j^{[2]} &= -2y_j^{[2]}({x_j^{[0]}}^2 + 3{y_j^{[0]}}^2) - 4x_j^{[2]}x_j^{[0]}y_j^{[0]} - \\ &\quad -y_{j-1}^{[2]} - y_{j+1}^{[2]} \\ \partial_{t_2}y_j^{[2]} &= +2x_j^{[2]}(3{x_j^{[0]}}^2 + {y_j^{[0]}}^2) + 4y_j^{[2]}x_j^{[0]}y_j^{[0]} \\ &\quad +x_{j-1}^{[2]} + x_{j+1}^{[2]}. \end{aligned} \tag{4.50}$$

Using these expressions for the slow derivatives we can now apply the chain rule to the quantities from (4.48). Luckily, the large majority of terms simplify, just as one might expect from coupled quantum transport where conservation laws are in place. After this process is finalised, we are left with

$$\begin{aligned} \partial_{t_2}A_c^{[2]} &= 2(-x_2^{[2]}y_1^{[0]} - x_2^{[0]}y_1^{[2]} + y_2^{[2]}x_1^{[0]} + y_2^{[0]}x_1^{[2]}) \\ \partial_{t_2}H_c^{[2]} &= 2(x_2^{[0]}\partial_{t_2}x_1^{[2]} + x_2^{[2]}\partial_{t_2}x_1^{[0]} + y_2^{[0]}\partial_{t_2}y_1^{[2]} + y_2^{[2]}\partial_{t_2}y_1^{[0]}) \end{aligned} \tag{4.51}$$

where $x_1^{[2]}$ and $y_1^{[2]}$ have the known expressions from (4.35), and their derivatives can im-

mediately be determined through a new set of chain rules. What is crucial to remember at this stage is that

1. Most contributions for the expressions at (4.48) cancel, leaving out only the terms which come from the interaction between the chain in the dimer 'breather - neighbour';

2. The expressions for both $\partial_{t_2} A_c^{[2]}$ and $\partial_{t_2} H_c^{[2]}$ are of the form $m x_2^{[2]} + n y_2^{[2]} + p$, where m, n, p have exact, known expressions which are seen at (4.51).

In conclusion the fluxes for both the norm and the Hamiltonian for the Bose-Hubbard chain are linear combinations of $x_2^{[2]}$ and $y_2^{[2]}$, where all proportionality constants are known.

4.6 Fluxes for the Hamiltonian and the Norm at order $\mathcal{O}(\varepsilon)$ for a dimer containing a breather

When it comes to the dimer (denoted in the equations by the subscript X_d) consisting of the breather and its nearest neighbour, the Bose Hubbard Hamiltonian and the norm are

$$\begin{aligned} A_d &= A_0^2 + x_1^2 + y_1^2 \\ H_d &= A_0^4 + (x_1^2 + y_1^2)^2 + \\ &\quad + 2A_0\big[x_1 \cos(t_1 + \phi_0^{[0]}) + y_1 \sin(t_1 + \phi_0^{[0]})\big]. \end{aligned} \tag{4.52}$$

Note that even if these variables only contain the wave-functions at sites $j = 0$ and $j = 1$ they are still coupled to the rest of the chain, as one might expect. At order zero, the coupling is simply the DNLSE, as discussed previously. At higher order, the coupling takes a more complex shape, and this is the purpose of studying the balance of the fluxes between the breather and the background.

Once again, we replace all the variables on the RHS with their asymptotic expansions and we separate the different orders of $\mathcal{O}(\sqrt{\varepsilon})$. Given the fact that most of these equations have already been used to derive the high order functions, there is no surprise that they will lead to the trivial identity $0 = 0$. However, once again, at order $\mathcal{O}(\varepsilon)$ we obtain a non-trivial result:

$$\begin{aligned} A_d^{[2]} &= 2(x_1^{[0]}x_1^{[2]} + y_1^{[0]}y_1^{[2]}) \\ H_d^{[2]} &= \sqrt{2}U(t_2) - \\ &\quad -\Big({x_1^{[0]}}^2 + {y_1^{[0]}}^2\Big)\Big[\tfrac{15}{2} - 4x_1^{[0]}(x_2^{[0]} - M) - 4y_1^{[0]}(y_2^{[0]} - N)\Big] - \\ &\quad -8\Big({x_1^{[0]}}^2 + {y_1^{[0]}}^2\Big)^3. \end{aligned} \tag{4.53}$$

In order to calculate the flows of energy and mass from the dimer towards the rest of the chain, we have to take the time derivatives of these quantities, which will be

$$\begin{aligned} \partial_{t_2} A_d^{[2]} &= 2(\partial_{t_2}x_1^{[0]}x_1^{[2]} + x_1^{[0]}\partial_{t_2}x_1^{[2]} + \partial_{t_2}y_1^{[0]}y_1^{[2]} + y_1^{[0]}\partial_{t_2}y_1^{[2]}) \\ \partial_{t_2} H_d^{[2]} &= 2(x_1^{[0]}\partial_{t_2}x_1^{[0]} + y_1^{[0]}\partial_{t_2}y_1^{[0]})(\tfrac{15}{2} + 4Mx_1^{[0]} + 4Ny_1^{[0]} - \\ &\quad -4x_1^{[0]}x_2^{[0]} - 4y_1^{[0]}y_2^{[0]}) - 24\Big({x_1^{[0]}}^2 + {y_1^{[0]}}^2\Big)^2 \times \\ &\quad \times 2(x_1^{[0]}\partial_{t_2}x_1^{[0]} + y_1^{[0]}\partial_{t_2}y_1^{[0]}) + 4\Big({x_1^{[0]}}^2 + {y_1^{[0]}}^2\Big) \times \\ &\quad \times(-x_1^{[0]}\partial_{t_2}x_2^{[0]} - y_1^{[0]}\partial_{t_2}y_2^{[0]} - x_2^{[0]}\partial_{t_2}x_1^{[0]} - y_2^{[0]}\partial_{t_2}y_1^{[0]} + \\ &\quad +\partial_{t_2}Mx_1^{[0]} + \partial_{t_2}Ny_1^{[0]} + M\partial_{t_2}x_1^{[0]} + N\partial_{t_2}y_1^{[0]}) + \\ &\quad +\sqrt{2}\partial_{t_2}U. \end{aligned} \tag{4.54}$$

Now we can replace the derivatives of the zero-order wave-functions with the DNLSE expressions and the derivatives of $x_1^{[2]}$ and $y_1^{[2]}$ by applying the chain rule on (4.35). Doing so in the expressions from (4.54) will lead to cumbersomely long expressions, and the use of a symbolic programming language such as `Mathematica` or `MAPLE` is strongly advised.

However, what is crucial to observe from this process is that

1. All the fast contributions in the norm and Hamiltonian of the dimer disappear - i.e. all dependencies are on t_2 and the quantities are completely independent of t_1. This is remarkable since most terms contained fast sinusoidals, which all cancelled out;

2. The expressions for both $\partial_{t_2} A_d^{[2]}$ and $\partial_{t_2} H_d^{[2]}$ are long analytical expressions, which do not depend at all on either $x_2^{[2]}$ or $y_2^{[2]}$.

4.7 Solvability Conditions

At the stage we have the flow of energy and norm from the dimer and from the rest of the chain. A balanced equation implies that

$$\begin{aligned} \partial_{t_2} N_d^{[2]} &= -\partial_{t_2} N_c^{[2]} \\ \partial_{t_2} H_d^{[2]} &= -\partial_{t_2} H_c^{[2]} \end{aligned} \tag{4.55}$$

which will be the solvability conditions for the mass end energy at order $\mathcal{O}(\varepsilon)$. These equations will be of the type

$$\begin{aligned} m_1 x_2^{[2]} + n_1 y_2^{[2]} &= p_1 \\ m_2 x_2^{[2]} + n_2 y_2^{[2]} &= p_2. \end{aligned} \tag{4.56}$$

By using the Cramer rule, we find that the two equations are always linearly independent and that the discriminant of this system is strictly positive, as long as $U(t_2)$ is exactly zero. After the algebraic operations are completed,

$$\begin{aligned} x_2^{[2]} = & \Big(-\tfrac{17 A_1^{[0]}}{2} + 8 {A_1^{[0]}}^5 \Big) \cos(\psi_1^{[0]}) + \\ & + 4 {A_1^{[0]}}^2 A_2^{[0]} \cos(2\psi_1^{[0]} - \psi_2^{[0]}) - \\ & - 2 {A_2^{[0]}}^3 \cos(\psi_2^{[0]}) - A_3^{[0]} \cos(\psi_3^{[0]}) + \\ & + \partial_{t_2} N - 4 {A_1^{[0]}}^2 M - \\ & 2 {A_1^{[0]}}^2 [M \cos(2\phi_0^{[0]}) + N \sin(2\phi_0^{[0]})] \end{aligned} \tag{4.57}$$

$$
\begin{aligned}
y_2^{[2]} \;=\; & \Big(-\tfrac{17A_1^{[0]}}{2} + 8{A_1^{[0]}}^5\Big)\sin(\psi_1^{[0]}) + \\
& + 4{A_1^{[0]}}^2 A_2^{[0]} \sin(2\psi_1^{[0]} - \psi_2^{[0]}) - \\
& - 2{A_2^{[0]}}^3 \sin(\psi_2^{[0]}) - A_3^{[0]} \sin(\psi_3^{[0]}) - \\
& - \partial_{t_2} M - 4{A_1^{[0]}}^2 N + \\
& 2{A_1^{[0]}}^2 [N\cos(2\phi_0^{[0]}) - M\sin(2\phi_0^{[0]})].
\end{aligned}
$$

The solvability conditions have been used to determine the expressions (4.57) for $x_2^{[2]}$ and $y_2^{[2]}$. However, the functions $M(t_2)$, $N(t_2)$, $P(t_2)$ and $Q(t_2)$ cannot be determined from the solvability conditions. These terms cancel at all orders leading to the trivial relation $0 = 0$. We show in the next subsection, however, that the explicit form of these functions is not necessary when determining the first differential equation in the perturbation expansion that does not average to zero over one period of the breather rotation.

We can now replace $x_2^{[2]}$ and $y_2^{[2]}$ with their analytical expressions obtained in (4.46) to obtain,

$$\langle D_{\varepsilon^2}^A \rangle = \frac{13}{2} A_1^{[0]} \sin(\phi_0^{[0]} - \psi_1^{[0]}). \tag{4.58}$$

It is quite remarkable that $M(t_2)$, $N(t_2)$ and $P(t_2)$ do not appear in the final expression of Eq. (4.58). This justifies a posteriori the truncation of the calculations made in the application of the solvability conditions above. We also note that:

$$\langle D_{\varepsilon^2}^A \rangle = \langle \partial_{t_2} A_0^{[4]} + \partial_{t_1} A_0^{[6]} \rangle = \langle \partial_{t_1} A_0^{[6]} \rangle \tag{4.59}$$

and finally obtain

$$\langle \partial_{t_1} A_0^{[6]} \rangle = \frac{13}{2} A_1^{[0]} \sin(\phi_0^{[0]} - \psi_1^{[0]}) \; . \tag{4.60}$$

Eq. (4.60) is the main result of this chapter of the thesis and is compared with numerical simulations of the DNLSE in the next section.

4.8 Breather fluctuations and comparison with simulations

4.8.1 Size of fluctuations

The amplitude of the breather fluctuates in time around a constant value $\varepsilon^{-1/2}A_0^{[-1]}$. For low orders of ε, the fluctuations average to zero over one fast rotation. More remarkably, our calculations are able to determine the magnitude of the slow perturbation which does not cancel over one fast oscillation. These slow drifts in the derivative of the breather norm appear at order $\mathcal{O}(\varepsilon^2)$, and for lattices with more than three sites ($N > 3$) are given by:

$$\langle d_t A_0 \rangle = \frac{13}{2}\varepsilon^2 A_1^{[0]} \sin(\phi_0^{[0]} - \psi_1^{[0]}) + \mathcal{O}(\varepsilon^{5/2}) \tag{4.61}$$

as a direct consequence of formula (4.60). $A_1^{[0]}$ and $\psi_1^{[0]}$ are the amplitude and the phase of the wave-function at the nearest site of the breather. Remarkably, the slow drift depends only on the state of the nearest neighbour of the breather, all interactions with more distant sites cancelling out after imposing the solvability conditions (4.55).

Note that Eq. (4.61) has been derived for breathers in contact with a background on one side only. Extensions to more generic configurations require a sum of both left and right contributions

$$\langle d_t A_0 \rangle = \frac{13}{2}\varepsilon^2 \sum_{j=\pm 1} A_j^{[0]} \sin(\phi_0^{[0]} - \psi_j^{[0]}) + \mathcal{O}(\varepsilon^{5/2})\,. \tag{4.62}$$

This is an approximation since in the case of breathers in contact with backgrounds on both sides, there are two solvability conditions for four unknown high order functions and mixed terms of left and right backgrounds. These terms and the flow of energy from one side of the breather to the other are negligible so that the derivative of the breather norm only contains two contributions of the type shown in Eq. (4.61).

For lattices of length $N > 3$, we run computational simulations and record the evolution of $A_0(t_1, t_2)$. This variable contains numerous high order terms which average to zero over one full oscillation of the breather. In order to extract the slow drifts, one must take the Fourier Transform of A_0, apply a Heaviside step function filter, and then take the inverse Fourier Transform. Analogously, one applies the same algorithm on $A_1(t_1, t_2)$ to obtain a numerical approximation of the zero-th order amplitude of the nearest neighbour.

Let $\Pi_f(X)$ denote a low-pass filtered version of a signal X, f being the cut-off frequency: all frequencies above this value are filtered out before applying, the inverse Fourier Transform. The averaged equation (4.61) implies that:

$$-2\pi\frac{13}{2}\varepsilon^3\Pi_f(A_1) \leq \Pi_f(A_0) \leq 2\pi\frac{13}{2}\varepsilon^3\Pi_f(A_1) \tag{4.63}$$

where one has used that $-1 \leq \sin(x) \leq 1 \ \ \forall x \in \mathbb{R}$ and also the properties of the Fourier transforms for derivatives $\mathcal{F}(X') = i\omega\mathcal{F}(X)$. The analytical predictions given by the multiple time scale analysis can therefore be tested by checking the truthfulness of (4.63). A similar idea is presented in [71], where the authors make analytical predictions on the behaviour of a multiple scale system, which are ultimately confirmed by computational tests which consist of numerical filtering.

In order to test the accuracy of (4.60), (4.61) and (4.62), we focus on the fluctuations of the time derivative of the breather amplitude ($d_t|z_0|$), as shown in Figure 4.2. This test shows the evolution of $d_t|z_0|$ over a time span of 100 time units for a breather of initial size $|z_0| = 5$. In Figure 4.2 (a), one can see that the fluctuations of the time derivative of the breather norm from the integration of Eq. (4.1) are of order $\mathcal{O}(1)$. This is not surprising, since when applying the two-scale differential operator $\varepsilon^{-1}\partial_{t_1} + \partial_{t_2}$ on the first non-trivial term from (4.26) one obtains a contribution of the form $\varepsilon^{-1}\partial_{t_1}\left(\varepsilon A_0^{[2]}\right)$, which creates fluctuations of order $\mathcal{O}(1)$. This dominant component in the derivative of the norm, however, vanishes when averaged over one full rotation.

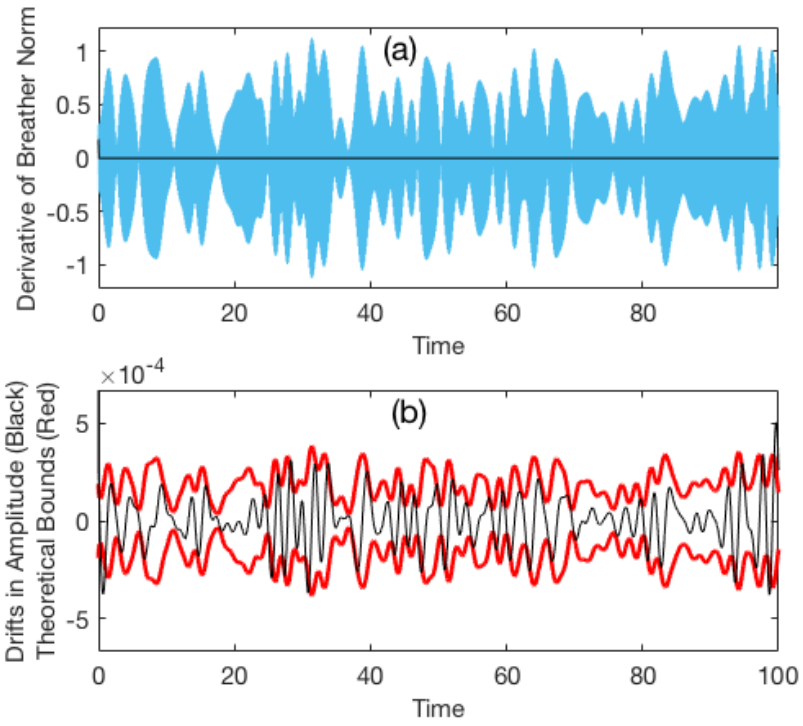

Figure 4.2: Time evolution of $d_t|z_0|$ over a time span of 100 time units. (a) $d_t|z_0|$ from the numerical integration of Eq. (4.1) (pale blue curve) and after the fast oscillating components have been filtered out (black line). (b) Same as (a) but magnified by a factor of 5000 (black line) with the analytical bounds from the inequalities (4.63) (red lines).

In order to see only the slow components of the derivative, one must use numerical low pass filters. Figure 4.2 (b) displays the same quantity, $d_t|z_0|$, but after the application of the numerical low pass filter and suitable magnification. The same black curve is also shown in the upper diagram, where due to the large difference in the magnitude of the fluctuations, it appears to be almost flat. What is remarkable is the excellent agreement between the slow fluctuations given by the numerical integration of Eq. (4.1) and the analytical boundaries predicted by the inequalities of Eq. (4.63). The extension of formula (4.61) to symmetric backgrounds is tested in Figure 4.3

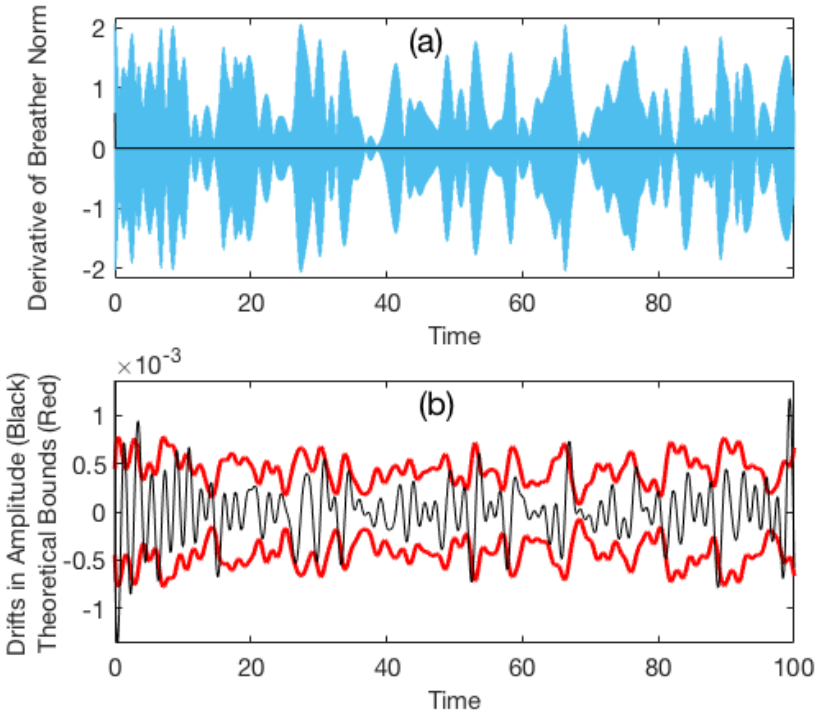

Figure 4.3: Same as Figure 4.2 but for a breather with backgrounds on both sides. (a) Time evolution of $d_t|z_0|$ over a time span of 100 time units from the numerical integration of Eq. (4.1) (pale blue curve) and after the fast oscillating components have been filtered out (black line). (b) Same as (a) but magnified by a factor of 5000 (black line) with the analytical bounds from the inequalities (4.63) based on Eq. (4.62) (red lines).

4.8.2 Stability of the trimer configuration

A Bose-Hubbard chain with only three sites ($N = 3$) is known as a trimer and has been the subject of extensive research [40, 72–75]. Our perturbative model is capable of explaining why trimer configurations give rise to breathers with a higher stability with respect to longer lattices.

One can obtain a slow drift equation for a dimer by replacing in (4.46) all the wave-functions for sites with $j \geq 2$ with zero. The averaged equation for the breather amplitude (4.46) reads

$$\begin{aligned}
\langle D^A_{\varepsilon^2} \rangle \;=\; & y_2^{[2]} \cos(\phi_0^{[0]}) - x_2^{[2]} \sin(\phi_0^{[0]}) - \\
& -2{A_2^{[0]}}^3 \sin(\phi_0^{[0]} - \psi_2^{[0]}) + \\
& +A_1^{[0]} \Big[\big(-2 + 8{A_1^{[0]}}^4 \big) \sin(\phi_0^{[0]} - \psi_1^{[0]}) + \\
& +4A_1^{[0]} A_2^{[0]} \sin(\phi_0^{[0]} - 2\psi_1^{[0]} + \psi_2^{[0]}) \Big] \\
& -A_3^{[0]} \sin(\phi_0^{[0]} - \psi_3^{[0]}) \\
& +\partial_{t_2} M(t_2) \cos(\phi_0^{[0]}) + \\
& +\partial_{t_2} N(t_2) \sin(\phi_0^{[0]}) \\
& -2{A_1^{[0]}}^2 \big[N(t_2) \cos(\phi_0^{[0]} - 2\psi_1^{[0]}) + \\
& +M(t_2) \sin(\phi_0^{[0]} - 2\psi_1^{[0]}) \big] \\
& +4{A_1^{[0]}}^2 \big[N(t_2) \cos(\phi_0^{[0]}) - \\
& -M(t_2) \sin(\phi_0^{[0]}) \big].
\end{aligned} \tag{4.64}$$

In a dimer configuration, all sites with $j \geq 2$ have $A_j = 0$, and all $x^{[k]}_{j\geq 2} = y^{[k]}_{j\geq 2} = 0 \;\; \forall \;\; k$. This also implies that $M = N = 0$. Under these circumstances, the equation from (4.64) greatly simplifies to:

$$\langle D^A_{\varepsilon^2} \rangle \;=\; A_1^{[0]} \big(-2 + 8{A_1^{[0]}}^4 \big) \sin(\phi_0^{[0]} - \psi_1^{[0]}). \tag{4.65}$$

In the presence of small backgrounds $8{A_1^{[0]}}^5 \ll 2A_1^{[0]}$, therefore (4.65) can be ap-

proximated by:

$$\langle D^{A}_{\varepsilon^2} \rangle \quad = \quad -2A_1^{[0]} \sin(\phi_0^{[0]} - \psi_1^{[0]}). \tag{4.66}$$

In the case when the breather sits at the middle of a trimer lattice, one can add independent left and right contributions, just as it was done for the case of lattices of generic lengths, and arrive at the expression (4.67).

This provides a new formula which will is valid when the breather does not have more than one neighbour on each side (i.e. the breather is either in a dimer or at the middle of a trimer). For backgrounds which are dominantly below one, this formula is:

$$\langle d_t A_0 \rangle = -2\varepsilon^2 \sum_{j=\pm 1} A_j^{[0]} \sin(\phi_0^{[0]} - \psi_j^{[0]}) + \mathcal{O}(\varepsilon^{5/2}) \, . \tag{4.67}$$

This makes the noise in the case of dimers and trimers around 3.25 times smaller than the one calculated for extended lattices, with $N > 3$. Formula (4.67) is confirmed by the numerical tests presented in Figure 4.4 which are done using the same low pass filters as introduced in the previous section. The difference in derivative between trimers and extended lattice configurations also implies a different size for the area of the Poincaré sections in the two cases. One can expect that extended systems produce Poincaré sections which are roughly $3.25^2 \approx 10$ times larger in area. The Poincaré section is taken by sampling the data after each complete rotation of the breather that takes $2\pi\varepsilon$ time units. Here ε is the inverse of the frequency which is determined numerically by applying Fast Fourier Transforms on the evolution of the real part of the breather norm.

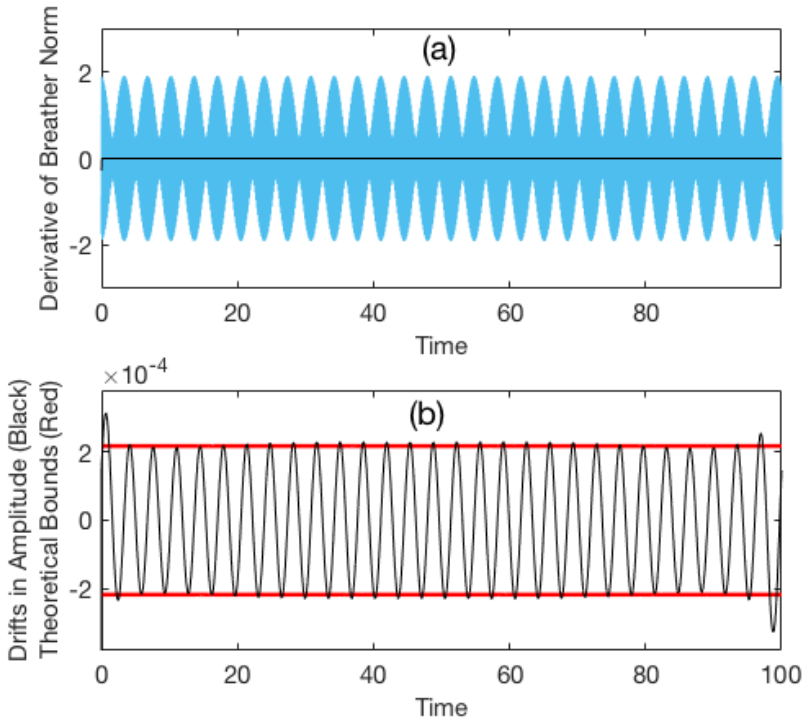

Figure 4.4: Time evolution of $d_t|z_0|$ in a three site lattice with the breather located in the middle of the chain over a time span of 100 units. (a) $d_t|z_0|$ from the numerical integration of Eq. (4.1) (pale blue curve) and after the fast oscillating components have been filtered out (black line). (b) Same as (a) but magnified by a factor of 5000 (black line) with the analytical bounds from the inequalities (4.63) after the factor 13/2 has been replaced by -2 to accommodate for limited size effects (red lines).

4.9 A less fluctuating quantity. Defining a slow norm

The asymptotic expansion for the breather norm had the form

$$A_0 = \varepsilon^{-1/2} A_0^{[-1]} + \sum_{m\geq 2} \varepsilon^{m/2} A_0^{[m]}(t_1, t_2), \tag{4.68}$$

where $A_0^{[m]}(t_1, t_2)$ are the higher order terms determined in this chapter and $A_0^{[-1]}$ is a constant (equal to $1/\sqrt{2}$). Using the information we gathered from solving the high orders of the perturbations, we can now write

$$\begin{aligned} A_0 = \frac{\varepsilon^{-1/2}}{\sqrt{2}} - \varepsilon\Big[x_1^{[0]}\cos(t_1+\phi_0^{[0]}) + y_1^{[0]}\sin(t_1+\phi_0^{[0]})\Big] + \\ +\varepsilon^2\Big[M(t_2)\cos(t_1+\phi_0^{[0]}) + N(t_2)\sin(t_1+\phi_0^{[0]})\Big] + \mathcal{O}(\varepsilon^{5/2}). \end{aligned} \tag{4.69}$$

We can now see that in the expression for the breather amplitude there is a dominant term at order $\mathcal{O}(\varepsilon)$ which oscillates on the scale of t_1. At this order, we can approximate $x_1^{[0]}$, $y_1^{[0]}$ and $\phi_1^{[0]}$ with x_1, y_1 and ϕ_0. Any corrections that would need to be made after this approximation would appear at higher order terms. Therefore we can approximate the fast oscillating component by

$$A_{osc} \equiv -\varepsilon\Big[x_1\cos(t_1+\phi_0) + y_1\sin(t_1+\phi_0)\Big], \tag{4.70}$$

and if we return to the original expression of the breather phase $\psi_0 \equiv \omega t + \phi_0 = t_1 + \phi_0$, this becomes

$$A_{osc} = -\varepsilon\Big[x_1\cos(\psi_0) + y_1\sin(\psi_0)\Big] = -\varepsilon A_1\cos(\psi_0 - \psi_1). \tag{4.71}$$

We can therefore write an expression for a variable which will oscillate less than A_0, that could be used to measure diffusions without taking into account the noise which would originate from the rather large oscillations at order $\mathcal{O}(\varepsilon)$. This quantity is given

by

$$Q = A_0 - A_{osc} = A_0 + \varepsilon A_1 \cos(\psi_0 - \psi_1). \tag{4.72}$$

This can be extended for systems with symmetric configurations, like we saw throughout this work. The definition of the slowly varying variable becomes

$$Q = A_0 + \varepsilon\Big[A_1 \cos(\psi_0 - \psi_1) + A_{-1} \cos(\psi_0 - \psi_{-1})\Big]. \tag{4.73}$$

The advantage of this quantity is that it fluctuates less than A_0, and sometimes it is more convenient to plot the time dependency of $Q(t)$ than that of $A_0(t)$. There is however, a slight disadvantage in the fact that one has to store the evolution of seven variables now instead of one. Given the fact that the simulations usually span very long integration times, this can make the data files very large. Alternatively, one could only store the value of $Q(t)$ and not that of A_0 and all the other variables, but this means that more operations are performed during the integration, and that one loses information when encountering events where the perturbation no longer holds. When the system arrives to a non-perturbative event, the quantity Q is no longer a good approximation of the slow part of A_0.

In order to avoid these issues, one can also store the trajectory of $A_0(t)$ and average the amplitudes over every 500 time units or so and this would flatten the fluctuations considerably. A time of 500 units might seem to be very long, but we are in the presence of trajectories which barely change over spans of $\mathcal{O}(10^5)$ units, therefore one would still have a considerable amount of data points to look at drifts and diffusions.

4.10 Conclusions

Tall breathers tend to decouple from the background even when the latter is relatively strong. If the breather amplitude is large enough, all background sites, including the nearest neighbours, perceive the breather as a purely reflective boundary. This

localised solution is very stable, displaying fast fluctuations which average to zero over one oscillation period. In order to quantify the slow changes of the breather size, one has to consider high orders of a (singular) perturbation expansion, the smallness parameter being the inverse of the breather mass. Here we have developed a multiple time-scales perturbative approach, which, with the help of conditions arising from energy and mass conservation, is able to predict topological differences among dimers, trimers, and lattices with $N > 3$. Breathers in trimer configurations are shown to be more stable than those in larger lattices. For spatially extended lattices, the bounds of the slow derivatives (given by the inequality (4.63)) are independent of the system size. This explains why, for long periods of time, these localised solutions are not affected by the phonon backgrounds they are in direct contact with.

During most of the evolution, in the absence of large excitations, the wave-function is perturbative in character and obeys the dynamics described by the zero-order equation (4.16). Very rarely, the phonon background spontaneously creates a neighbouring excitation large enough to take the system out of the perturbative regime, causing a sudden change in the breather shape.

The existence of a clear perturbative regime, even in the presence of large backgrounds, suggests that most of the trajectories of the system can be simulated with the help of averaged differential equations where the fast time scale has been eliminated. This type of model would be useful for investigating phenomena which occur during time scales that are larger than the fast fluctuations of the breather, such as the effect of breathers on quantum transport and the thermalisation of backgrounds in the presence of breathers.

If one wants to study the entire evolution of breathers, perturbative techniques do not suffice. They can be used however to differentiate between slow processes and catastrophic events, which occur when Eq. (4.62) is violated.

Breather lifetimes are characterised by three time-scales: the very small period of the breather rotation, the times over which the background evolves, and the times over

which rare events may occur. The first order at which there is a non-zero term in the second time scale is ε^2 for the derivative of the breather norm. This term, however, averages to zero over the second time scale if one makes the assumption that correlations between the zero-th order wave-function components decay very rapidly. What follows from this is that, under the assumption of a very slow diffusion, the evolution of the breather is most likely given by events which occur on the third time scale, i.e. rare events. As the amplitude of the breather is increased drastically, the spontaneous formation of an excitation of order $\sqrt{\varepsilon}$ decreases exponentially, since the background amplitudes have probability distributions which decay exponentially fast [34]. This might imply that in those domains, the lifetime of breathers is not dictated by rare events, but by diffusion processes which could occur at even higher orders than that at which the first non-zero terms occurs.

Chapter 5

Averaging, Effective Hamiltonians and Adiabatic Invariants

5.1 Time averaging of the DNLSE dynamics

The averaging algorithm is developed for lattices where a single pinned breather sits at the edge of a one-dimensional Bose-Hubbard chain (the sites are identified using the coordinate $j \in \{0, 1, 2, ..., N-1\}$, where N denotes the length of the chain). As in the case of the Multiple Time Scale Analysis (MTSA) algorithm presented in Chapter 4, the breather is set to occupy the site $j = 0$, and all the background sites are located on the same side of the breather. Using the work from Chapter 4, one can state that, in the presence of backgrounds of order $\mathcal{O}(1)$, breathers are very well localised, occupying a single site in the lattice. In addition, these localised modes are characterised by fast dynamics which adiabatically decouple from their surroundings, rotating with frequencies which are much higher then the characteristic peaks found in the background spectrum [34]. One can take advantage of this separation of time-scales to build a perturbative calculation through which one arrives to an averaged discrete

nonlinear Schrödinger equation (AvDNLSE).

Since the averaging algorithm employs perturbation analysis elements, one must start by defining a basis for the phase space where all variables have continuous, well defined derivatives (i.e. there are no divergences, and all Taylor expansions are used within their convergence radii). This coordinate system is given by the polar coordinates of the breather and of the Cartesian coordinates of the background $\{(A_0, \psi_0), (x_j, y_j) | \forall j > 0\}$. The only fast variable in this set is ψ_0, the phase of the breather, which can be approximated by the monotonously increasing phase of a harmonic oscillator with frequency ω. It is now possible to transition to a set of coordinates which are all slow $\{(A_0, \phi_0), (x_j, y_j) | \forall j > 0\}$, through the transformation $d_t\phi_0(t) = d_t\psi_0(t) - \omega(t)$. As it was stated before, when expressing the DNLSE in a hybrid polar-Cartesian system of slow coordinates (4.4), one arrives at

$$\begin{aligned}
d_t A_0 &= x_1 \sin(\omega t + \phi_0) - y_1 \cos(\omega t + \phi_0) \\
d_t \phi_0 &= 2A_0^2 - \omega + {A_0}^{-1}\big[x_1 \cos(\omega t + \phi_0) + \\
&\quad + y_1 \sin(\omega t + \phi_0)\big] \\
d_t x_1 &= -2(x_1^2 + y_1^2) y_1 - y_2 - A_0 \sin(\omega t + \phi_0) \\
d_t y_1 &= 2(x_1^2 + y_1^2) x_1 + x_2 + A_0 \cos(\omega t + \phi_0) \\
d_t x_j &= -2(x_j^2 + y_j^2) y_j - y_{j-1} - y_{j+1} \qquad j \geq 2 \\
d_t y_j &= 2(x_j^2 + y_j^2) x_j + x_{j-1} + x_{j+1} \qquad j \geq 2.
\end{aligned} \tag{5.1}$$

It now becomes visible that in this system of coordinates the only divergence for the derivatives occurs when $A_0 \to 0$. Since the current perturbative theory is developed for breathers (bright solitons, with $A_0 \gg 0$), this divergence however is not important within the averaging regime.

One can now use the fact that all the coordinates in the set $\{(A_0, \phi_0), (x_j, y_j) | \forall j > 0\}$ are slow. As a first approximation, one can consider that all these variables are constant during a full breather rotation. Integrating (5.1) (i.e. applying the operator $\int_0^t (*) dt'$) one arrives at

$$
\begin{aligned}
\delta A_0^{(1)} &= -\big[\tilde{x}_1\cos(\omega t+\tilde{\phi}_0)+\tilde{y}_1\sin(\omega t+\tilde{\phi}_0)\big]/\omega+ \\
&\quad +\big[\tilde{x}_1\cos(\tilde{\phi}_0)+\tilde{y}_1\sin(\tilde{\phi}_0)\big]/\omega \\
\delta\phi_0^{(1)} &= \tilde{A}_0^{-1}\big[\tilde{x}_1\sin(\omega t+\tilde{\phi}_0)-\tilde{y}_1\cos(\omega t+\tilde{\phi}_0)\big]/\omega- \\
&\quad -\tilde{A}_0^{-1}\big[\tilde{x}_1\sin(\tilde{\phi}_0)-\tilde{y}_1\cos(\tilde{\phi}_0)\big]/\omega \\
&\quad +(2\tilde{A}_0^2-\omega)t \\
\delta x_1^{(1)} &= -\big[2(\tilde{x}_1^2+\tilde{y}_1^2)\tilde{y}_1+\tilde{y}_2\big]\times t+ \\
&\quad +\tilde{A}_0\big[\cos(\omega t+\tilde{\phi}_0)-\cos(\tilde{\phi}_0)\big]/\omega \\
\delta y_1^{(1)} &= \big[2(\tilde{x}_1^2+\tilde{y}_1^2)\tilde{x}_1+\tilde{x}_2\big]\times t+ \\
&\quad +\tilde{A}_0\big[\sin(\omega t+\phi_0)-\sin(\phi_0)\big]/\omega \\
\delta x_j^{(1)} &= \big[-2(\tilde{x}_j^2+\tilde{y}_j^2)\tilde{y}_j-\tilde{y}_{j-1}-\tilde{y}_{j+1}\big]\times t \\
\delta y_j^{(1)} &= \big[2(\tilde{x}_j^2+\tilde{y}_j^2)\tilde{x}_j+\tilde{x}_{j-1}+\tilde{x}_{j+1}\big]\times t,
\end{aligned}
\tag{5.2}
$$

where the tilde over-script denotes the initial value of a given coordinate ($\tilde{\psi}\equiv\psi(t=0)$). If one takes the frequency to be $\omega\equiv 2\tilde{A}_0^2$ and evaluates the infinitesimal drifts from (5.2) after one rotation exactly (i.e. at time $t=2\pi/\omega$), one obtains

$$
\begin{aligned}
\delta A_0^{(1)}|_{t=2\pi/\omega} &= 0 \\
\delta\phi_0^{(1)}|_{t=2\pi/\omega} &= 0 \\
\delta x_1^{(1)}|_{t=2\pi/\omega} &= -\big[2(\tilde{x}_1^2+\tilde{y}_1^2)\tilde{y}_1+\tilde{y}_2\big]\times 2\pi/\omega \\
\delta y_1^{(1)}|_{t=2\pi/\omega} &= \big[2(\tilde{x}_1^2+\tilde{y}_1^2)\tilde{x}_1+\tilde{x}_2\big]\times 2\pi/\omega \\
\delta x_j^{(1)}|_{t=2\pi/\omega} &= \big[-2(\tilde{x}_j^2+\tilde{y}_j^2)\tilde{y}_j-\tilde{y}_{j-1}-\tilde{y}_{j+1}\big]\times 2\pi/\omega \\
\delta y_j^{(1)}|_{t=2\pi/\omega} &= \big[2(\tilde{x}_j^2+\tilde{y}_j^2)\tilde{x}_j+\tilde{x}_{j-1}+\tilde{x}_{j+1}\big]\times 2\pi/\omega.
\end{aligned}
\tag{5.3}
$$

The slow drifts after precisely one rotation can be used to determine the average derivative of a quantity X, which we will denote by $D_t^{\mathrm{I}}X$. This will be given by $D_t^{\mathrm{I}}X\equiv\omega/(2\pi)\times\delta X^{(1)}|_{t=2\pi/\omega}$. For the hybrid system of coordinates, these average derivatives will be:

$$
\begin{aligned}
D_t^{\mathrm{I}} A_0 &\equiv \omega/(2\pi) \times \delta A_0^{(1)}|_{t=2\pi/\omega} \\
&= 0 \\
D_t^{\mathrm{I}} \phi_0 &\equiv \omega/(2\pi) \times \delta \phi_0^{(1)}|_{t=2\pi/\omega} \\
&= 0 \\
D_t^{\mathrm{I}} x_1 &\equiv \omega/(2\pi) \times \delta x_1^{(1)}|_{t=2\pi/\omega} \\
&= -2(\tilde{x}_1^2 + \tilde{y}_1^2)\tilde{y}_1 - \tilde{y}_2 \\
D_t^{\mathrm{I}} y_1 &\equiv \omega/(2\pi) \times \delta y_1^{(1)}|_{t=2\pi/\omega} \\
&= +2(\tilde{x}_1^2 + \tilde{y}_1^2)\tilde{x}_1 + \tilde{x}_2 \\
D_t^{\mathrm{I}} x_j &\equiv \omega/(2\pi) \times \delta x_j^{(1)}|_{t=2\pi/\omega} \\
&= -2(\tilde{x}_j^2 + \tilde{y}_j^2)\tilde{y}_j - \tilde{y}_{j-1} - \tilde{y}_{j+1} \\
D_t^{\mathrm{I}} y_j &\equiv \omega/(2\pi) \times \delta y_j^{(1)}|_{t=2\pi/\omega} \\
&= +2(\tilde{x}_j^2 + \tilde{y}_j^2)\tilde{x}_j + \tilde{x}_{j-1} + \tilde{x}_{j+1},
\end{aligned}
\tag{5.4}
$$

which implies that, under this first approximation, all sites in the background ($j \geq 1$) obey the DNLSE, and are completely decoupled from the breather. The breather does not change at all in this first approximation. This is, once again, the breather-reflective boundary analogy described in the previous chapter. As we might have expected from the very stable nature of the soliton, both the breather phase and its amplitude do not change at all when taking the first order average. The breather wave-function is simply a constant which does not interact with its surroundings, and can be replaced by a reflective boundary ($|z_0(t)| = 0 \ \forall \ t$). It now becomes apparent that one must go to higher orders to obtain an averaged equation where the background and the breather are coupled.

In order to go to higher orders, one must first approximate all the slow coordinates

with the expressions

$$\begin{aligned} A_0(t) &\rightarrow \tilde{A}_0 + \delta A_0^{(1)}(t) \\ \phi_0(t) &\rightarrow \tilde{\phi}_0 + \delta \phi_0^{(1)}(t) \\ x_j(t) &\rightarrow \tilde{x}_j + \delta x_j^{(1)}(t) \\ y_j(t) &\rightarrow \tilde{y}_j + \delta y_j^{(1)}(t), \end{aligned} \tag{5.5}$$

in the DNLSE from (5.1). The corrections must be expressed for a generic time t, and not only after one full rotation, to make sure that no important dynamics from interference or any other wave phenomena are missed. It is now useful to introduce a smallness parameter, using the same definition that was utilised throughout this thesis, i.e. $\varepsilon \equiv \omega^{-1} = 1/(2\tilde{A}_0^2)$, which helps quantify the orders of magnitude of the corrections introduced after the change of variables at (5.5). All coordinates are replaced with their new expressions in the differential equations of (5.2). After this substitution is complete, one expands all the equations in terms of the smallness parameter, and checks the leading order of the correction. The dominant order of the corrections will be $\mathcal{O}(\varepsilon)$ for the breather amplitude and $\mathcal{O}(\varepsilon^{3/2})$ for the breather phase. Similarly, the wave-function for the nearest neighbour has correction as large as $\mathcal{O}(\varepsilon^{1/2})$, while all the other background sites have their first corrections at $\mathcal{O}(\varepsilon)$. These findings are absolutely identical to what we obtained through asymptotic expansions in Chapter 4 at (4.6).

After expressing all differential equations as power series of the smallness parameter, through the use of Taylor expansions we can approximate the differential equations with

$$\begin{aligned} d_t A_0 &= \tilde{x}_1 \sin(\omega t + \tilde{\phi}_0) - \tilde{y}_1 \cos(\omega t + \tilde{\phi}_0) + \\ &\quad + \delta x_1^{(1)} \sin(\omega t + \tilde{\phi}_0) - \delta y_1^{(1)} \cos(\omega t + \tilde{\phi}_0) + \texttt{H.O.T.} \\ d_t \phi_0 &= \Big[\tilde{x}_1 \cos(\omega t + \tilde{\phi}_0) + \tilde{y}_1 \sin(\omega t + \tilde{\phi}_0)\Big]/\tilde{A}_0 + \\ &\quad + \Big[\delta x_1^{(1)} \cos(\omega t + \tilde{\phi}_0) + \delta y_1^{(1)} \sin(\omega t + \tilde{\phi}_0)\Big]/\tilde{A}_0 - \\ &\quad - \delta A_0^{(1)} \Big[\tilde{x}_1 \cos(\omega t + \tilde{\phi}_0) + \tilde{y}_1 \sin(\omega t + \tilde{\phi}_0)\Big]/\tilde{A}_0^2 \\ &\quad + \texttt{H.O.T.} \end{aligned} \tag{5.6}$$

$$
\begin{aligned}
d_t x_1 &= -\big[2(\tilde{x}_1^2+\tilde{y}_1^2)\tilde{y}_1+\tilde{y}_2\big]- \\
&\quad -4\delta x_1^{(1)}\tilde{x}_1\tilde{y}_1-2\delta y_1^{(1)}(\tilde{x}_1^2+3\tilde{y}_1^2)-\delta y_2^{(1)}- \\
&\quad -4\delta x_1^{(1)}\delta y_1^{(1)}\tilde{x}_1-6\delta {y_1^{(1)}}^2\tilde{y}_1-2\delta {x_1^{(1)}}^2\tilde{y}_1- \\
&\quad -\delta A_0^{(1)}\sin(\omega t+\tilde{\phi}_0)-\tilde{A}_0\sin(\omega t+\tilde{\phi}_0)+\texttt{H.O.T.} \\
d_t y_1 &= +\big[2(\tilde{x}_1^2+\tilde{y}_1^2)\tilde{x}_1+\tilde{x}_2\big]+ \\
&\quad +4\delta y_1^{(1)}\tilde{x}_1\tilde{y}_1+2\delta x_1^{(1)}(3\tilde{x}_1^2+\tilde{y}_1^2)+\delta x_2^{(1)}+ \\
&\quad +4\delta x_1^{(1)}\delta y_1^{(1)}\tilde{y}_1+6\delta {x_1^{(1)}}^2\tilde{x}_1+2\delta {y_1^{(1)}}^2\tilde{x}_1+ \\
&\quad +\delta A_0^{(1)}\cos(\omega t+\tilde{\phi}_0)+\tilde{A}_0\cos(\omega t+\tilde{\phi}_0)+\texttt{H.O.T.}
\end{aligned}
\tag{5.7}
$$

$$
\begin{aligned}
d_t x_2 &= -\big[2(\tilde{x}_2^2+\tilde{y}_2^2)\tilde{y}_2+\tilde{y}_1+\tilde{y}_3\big]-\delta y_1^{(1)}+\texttt{H.O.T.} \\
d_t y_2 &= +\big[2(\tilde{x}_2^2+\tilde{y}_2^2)\tilde{x}_2+\tilde{x}_1+\tilde{x}_3\big]+\delta x_1^{(1)}+\texttt{H.O.T.}
\end{aligned}
\tag{5.8}
$$

$$
\begin{aligned}
d_t x_{j>2} &= -\big[2(\tilde{x}_j^2+\tilde{y}_j^2)\tilde{y}_j+\tilde{y}_{j-1}+\tilde{y}_{j+1}\big]+\texttt{H.O.T.} \\
d_t y_{j>2} &= +\big[2(\tilde{x}_j^2+\tilde{y}_j^2)\tilde{x}_j+\tilde{x}_{j-1}+\tilde{x}_{j+1}\big]+\texttt{H.O.T.}
\end{aligned}
\tag{5.9}
$$

For all the Taylor expansions of the derivatives, we now replace $\delta A_0^{(1)}$, $\delta\phi_0^{(1)}$, $\delta x_j^{(1)}$ and $\delta y_j^{(1)}$ with their full analytical expressions from (5.2). The expressions for the derivatives become rather long and therefore we use a programming language which can manipulate symbolic calculations (such as `Mathematica` or `MAPLE`). Once this algebraic operation is completed, all derivatives will be expressed as functions of $\tilde{A}_0$, $\tilde{\phi}_0$, $\tilde{x}_j$ and $\tilde{y}_j$, in addition to the fast phase variables t and ω.

The next step is to redefine the time as $T \equiv \omega t+\tilde{\phi}_0$, so that all trigonometric functions will have very simple arguments (just the variable T). When doing this substitution, one must replace the variable t by $\frac{T-\tilde{\phi}_0}{\omega}$ in all the expressions of $\delta A_0^{(1)}$, $\delta\phi_0^{(1)}$, $\delta x_j^{(1)}$ and $\delta y_j^{(1)}$.

At this stage, ω can be replaced with $1/\varepsilon$ and $\delta A_0^{(1)}$ with $1/\sqrt{2\varepsilon}$, and all derivatives from (5.6)-(5.9) can be written as power series of ε. In order to determine the drifts according to the second order approximation, we have to integrate these power series

for T ranging from $\tilde{\phi}_0$ to $t_{max}/\varepsilon + \tilde{\phi}_0$. This interval corresponds to a time span of $t \in [0, t_{max}]$ for the natural time. Finally, one can determine the infinitesimal increments $\left\{(\delta A_0^{(2)}, \delta\phi_0^{(2)}), (\delta x_j^{(2)}, \delta y_j^{(2)}) | \forall j > 0\right\}$ by evaluating these integrals at $t_{max} = 2\pi\varepsilon$.

Just as done for the order `I`, the value of these increments is evaluated after one rotation exactly to approximate the values of the derivatives

$$\begin{aligned} D_t^{\mathtt{II}} A_0 &\equiv \omega/(2\pi) \times \delta A_0^{(2)}|_{t=2\pi/\omega} \\ D_t^{\mathtt{II}} \phi_0 &\equiv \omega/(2\pi) \times \delta \phi_0^{(2)}|_{t=2\pi/\omega} \\ D_t^{\mathtt{II}} x_j &\equiv \omega/(2\pi) \times \delta x_j^{(2)}|_{t=2\pi/\omega} \\ D_t^{\mathtt{II}} y_j &\equiv \omega/(2\pi) \times \delta y_j^{(2)}|_{t=2\pi/\omega}, \end{aligned} \tag{5.10}$$

which leads to the following analytical expressions

$$\begin{aligned} D_t^{\mathtt{II}} A_0 &= \varepsilon\big[\cos(\tilde{\phi}_0)(2\tilde{y}_1(\tilde{x}_1^2 + \tilde{y}_1^2) + \tilde{y}_2) - \\ &\quad - \sin(\tilde{\phi}_0)(2\tilde{x}_1(\tilde{x}_1^2 + \tilde{y}_1^2) + \tilde{x}_2)\big] + \mathcal{O}(\varepsilon^2) \\ D_t^{\mathtt{II}} \phi_0 &= \varepsilon + \\ &\quad + \varepsilon^{3/2}\sqrt{2}\big[\sin(\tilde{\phi}_0)(2\tilde{y}_1(\tilde{x}_1^2 + \tilde{y}_1^2) + \tilde{y}_2) + \\ &\quad + \cos(\tilde{\phi}_0)(2\tilde{x}_1(\tilde{x}_1^2 + \tilde{y}_1^2) + \tilde{x}_2)\big] + \\ &\quad + \mathcal{O}(\varepsilon^{5/2}) \end{aligned} \tag{5.11}$$

$$
\begin{aligned}
D_t^{\mathrm{II}} x_1 &= -2(\tilde{x}_1^2+\tilde{y}_1^2)\tilde{y}_1-\tilde{y}_2+ \\
&\quad +\sqrt{\varepsilon}\times\sqrt{2}\big[2\tilde{x}_1\tilde{y}_1\cos(\tilde{\phi}_0)+ \\
&\quad +(\tilde{x}_1^2+3\tilde{y}_1^2)\sin(\tilde{\phi}_0)\big]+ \\
&\quad +\varepsilon\big[\tilde{y}_1\cos(2\tilde{\phi}_0)-\tilde{x}_1\sin(2\tilde{\phi}_0)-6\tilde{y}_1\big]+ \\
&\quad +\varepsilon\times D_{x_1}^{\varepsilon}+\mathcal{O}(\varepsilon^{3/2}) \\
D_t^{\mathrm{II}} y_1 &= +2(\tilde{x}_1^2+\tilde{y}_1^2)\tilde{x}_1+\tilde{x}_2- \\
&\quad -\sqrt{\varepsilon}\times\sqrt{2}\big[2\tilde{x}_1\tilde{y}_1\sin(\tilde{\phi}_0)+ \\
&\quad +(3\tilde{x}_1^2+\tilde{y}_1^2)\cos(\tilde{\phi}_0)\big]+ \\
&\quad +\varepsilon\big[\tilde{x}_1\cos(2\tilde{\phi}_0)+\tilde{y}_1\sin(2\tilde{\phi}_0)+6\tilde{x}_1\big]+ \\
&\quad +\varepsilon\times D_{y_1}^{\varepsilon}+\mathcal{O}(\varepsilon^{3/2})
\end{aligned}
\tag{5.12}
$$

$$
\begin{aligned}
D_t^{\mathrm{II}} x_2 &= -2(\tilde{x}_2^2+\tilde{y}_2^2)\tilde{y}_2-\tilde{y}_1-\tilde{y}_3+ \\
&\quad +\sqrt{\varepsilon}\sin(\tilde{\phi}_0)/\sqrt{2}+\mathcal{O}(\varepsilon) \\
D_t^{\mathrm{II}} y_2 &= +2(\tilde{x}_2^2+\tilde{y}_2^2)\tilde{x}_2+\tilde{x}_1+\tilde{x}_3+ \\
&\quad -\sqrt{\varepsilon}\cos(\tilde{\phi}_0)/\sqrt{2}+\mathcal{O}(\varepsilon)
\end{aligned}
\tag{5.13}
$$

$$
\begin{aligned}
D_t^{\mathrm{II}} x_j &= -2(\tilde{x}_j^2+\tilde{y}_j^2)\tilde{y}_j-\tilde{y}_{j-1}-\tilde{y}_{j+1}+ \\
&\quad +\mathcal{O}(\varepsilon) \\
D_t^{\mathrm{II}} y_j &= +2(\tilde{x}_j^2+\tilde{y}_j^2)\tilde{x}_j+\tilde{x}_{j-1}+\tilde{x}_{j+1}+ \\
&\quad +\mathcal{O}(\varepsilon).
\end{aligned}
\tag{5.14}
$$

The averaged differential equations for the nearest neighbour (5.12) contain the corrections D_{x_1} and D_{y_1} at order $\mathcal{O}(\varepsilon)$. These expressions are proportional to π and arise from the integration of terms, say, $\tilde{K}$ which are generic functions of $\tilde{A}_0$, $\tilde{\phi}_0$, $\tilde{x}_j$ and $\tilde{y}_j$. When these integrals are performed, the result will be of the shape $\tilde{K}\times t$, and given the fact that the integrals are evaluated at $t=2\pi\varepsilon$, they will take the form $2\pi\tilde{K}\varepsilon$. These are secular terms at order $\mathcal{O}(\varepsilon)$, which will increase linearly with time, and should not be included in the final expressions of the derivatives [76]. As a rule of thumb, all factors proportional to π or higher powers of π are secular terms, and

should always be omitted.

Therefore, we will not keep D_{x_1} and D_{y_1} in the averaged equations, since their secular nature would generate trajectories which diverge and this would contradict the notion that the Hamiltonian of the system is conserved at all times. All averaging techniques must be performed under the assumption that the system is still symplectic, just as in the case of the original DNLSE. Once averaging is completed in a micro-canonical set-up, one can extend the equations to open systems which are allowed to exchange energy with the environment.

At this stage, one has an averaged differential equation which displays coupling between the breather and the background. The procedure could be continued to reach derivatives at third order, but for now, this is beyond the interest of this thesis work since the present goal is the simplest system that displays an interaction between the breather and the background. Note also that equations (5.11)-(5.14) originate from the truncation of a power series, which is not unique. One could go to arbitrarily high orders and include as many terms one pleases, but by doing so, the implementation of any numerical algorithm based on the idea of averaging would be slowed down considerably.

At this stage, we have coupled differential equations for the breather and the background which show a clear non-zero interaction. These equations however no longer originate from the Bose-Hubbard Hamiltonian, but from an average over a fast oscillation of this quantity. It is therefore important to determine which effective Hamiltonian generates these differential equations, and whether it is still possible to conserve the norm of the condensate when evolving the system under this newly obtained effective Hamiltonian.

It will later become apparent that the current equations are more than adequate to build an effective interaction Hamiltonian which will ultimately be used to create a hybrid integration scheme that will generate the full trajectories of breathers much faster than the DNLSE. Keeping more terms in the truncation of the averaged differential equations would have led to more algebraically complex expressions. This unnecessary

added level of computational difficulty would have slowed down the averaged model so much, that one would get no gain from using the AvNLSE instead of the full DNLSE.

5.2 The Effective Hamiltonian

The DNLSE (5.1) originates from the Bose-Hubbard Hamiltonian

$$\begin{aligned} H_{BH} &= \tfrac{1}{4}\textstyle\sum_{j\geq 0}(p_j^2+q_j^2)^2+ \\ &\quad +\textstyle\sum_{j\geq 0}(p_jp_{j+1}+q_jq_{j+1}), \end{aligned} \tag{5.15}$$

where $p_j \equiv x_j\sqrt{2}$ and $q_j \equiv y_j\sqrt{2}$ are the generalised coordinates of the system [50]. In addition to conserving the Bose-Hubbard Hamiltonian, the DNLSE also conserves the total norm of the condensate, given by $\mathcal{N} \equiv \frac{1}{2}\sum_{j\geq 0}(p_j^2+q_j^2)$.

Therefore, when building averaged differential equations where the fast time has been eliminated, one must make sure that the new trajectory also obey mass and energy conservation. Just as in the case of other perturbative approximations of the DNLSE (see Chapter 4), one cannot expect the new system to follow the same trajectory as the one given by the original equation, due to the chaotic nature of the Nonlinear Schrödinger Equation. Moreover, when employing the averaged equations in grand canonical ensembles, where the condensate is in contact with thermostats generated by Langevin noise [50], one will use much larger time steps for the averaged system than for the original equation. This implies that the noise will be sampled differently, even if the same seed is used to generate the two trajectories. However, the computational advantage of an algorithm which employs large steps is clearly undeniable.

Even if the trajectories given by the two algorithms will ultimately split, it is essential to make sure that in closed systems, the averaged equations do not artificially create or annihilate mass, and that the new trajectory is still bound to a hyper-surface given by a Hamiltonian. This new Hamiltonian will be referred to as the effective Hamiltonian of the system, and it will be constructed from the averaged equations which have

been obtained at (5.11)-(5.14). We will later see that the averaged equations alone cannot capture the full dynamics which happen during a breather's life-time, but they will constitute a solid starting point for a Hybrid Integration scheme.

The generalised coordinates for the background will once again be $p_j \equiv x_j\sqrt{2}$ and $q_j \equiv y_j\sqrt{2}$, while the breather will be denoted by an oscillator with phase ϕ_0 and intensity $I \equiv A_0^2$, as is usually done in slow-fast Hamiltonian systems [60]. The effective Hamiltonian will therefore be a function of

$$\begin{aligned} p_0 &\equiv \tilde{A}_0^2 \\ q_0 &\equiv \tilde{\phi}_0 \\ p_j &\equiv \tilde{x}_j\sqrt{2} \\ q_j &\equiv \tilde{y}_j\sqrt{2}. \end{aligned} \tag{5.16}$$

Since the expressions we have to deal with are generally algebraically complex, we have decided to use p_j and q_j instead of $\tilde{p}_j$ and $\tilde{q}_j$, even if the second notation would be more correct, since it would refer to the initial conditions (i.e. the values at which we start before performing integrations over one rotation exactly).

Since we are now working with the breather intensity, i.e. $p_0 = I_0 \equiv A_0^2$, it is highly encouraged to study the evolution of the breather in terms of $\dot{I}_0 = \dot{p}_0 = 2A_0\dot{A}_0$. Furthermore, when working with averaged differential equations, it is useful to employ the following convention, which is useful in avoiding ambiguities.

- The differential operator d_tX is the time derivative, as it is given by the Bose-Hubbard Hamiltonian (5.15)
- The differential operator $\dot{X}$ is the averaged time derivative, which as was previously shown, is not a unique operator, as it can depend on the averaging technique, on the number of terms kept in a truncation, and on other considerations such as on the omission of secular terms. From this stage onward, however, notations such as $D_t^{\mathrm{I}}X$ and $D_t^{\mathrm{II}}X$ will be replaced with the more compact $\dot{X}$

After expressing all the truncated differential equations from (5.11)-(5.14) in terms of these newly defined coordinates, one arrives to

$$\begin{aligned}\dot{p}_0 &= \tfrac{1}{\sqrt{2p_0}}\Big\{\big[q_1(p_1^2+q_1^2)+q_2\big]\cos(q_0)- \\ &\quad -\big[p_1(p_1^2+q_1^2)+p_2\big]\sin(q_0)\Big\},\end{aligned} \tag{5.17}$$

$$\begin{aligned}\dot{q}_0 &= \tfrac{1}{2p_0}+(\tfrac{1}{2p_0})^{3/2}\Big\{\big[q_1(p_1^2+q_1^2)+q_2\big]\sin(q_0)+ \\ &\quad +\big[p_1(p_1^2+q_1^2)+p_2\big]\cos(q_0)\Big\},\end{aligned} \tag{5.18}$$

$$\begin{aligned}\dot{p}_1 &= -(p_1^2+q_1^2)q_1-q_2+ \\ &\quad +\tfrac{1}{\sqrt{2p_0}}\Big\{(p_1^2+3q_1^2)\sin(q_0)+2p_1q_1\cos(q_0)\Big\}+ \\ &\quad +\tfrac{1}{2p_0}\big[q_1\cos(2q_0)-p_1\sin(2q_0)-3q_1\big],\end{aligned} \tag{5.19}$$

$$\begin{aligned}\dot{q}_1 &= (p_1^2+q_1^2)p_1+p_2- \\ &\quad -\tfrac{1}{\sqrt{2p_0}}\Big\{(3p_1^2+q_1^2)\cos(q_0)+2p_1q_1\sin(q_0)\Big\}+ \\ &\quad +\tfrac{1}{2p_0}\big[p_1\cos(2q_0)+q_1\sin(2q_0)+3p_1\big],\end{aligned} \tag{5.20}$$

$$\begin{aligned}\dot{p}_2 &= -(p_2^2+q_2^2)q_2-q_1-q_3+ \\ &\quad +\tfrac{1}{\sqrt{2p_0}}\sin(q_0),\end{aligned} \tag{5.21}$$

$$\begin{aligned}\dot{q}_2 &= (p_2^2+q_2^2)p_2+p_1+p_3- \\ &\quad -\tfrac{1}{\sqrt{2p_0}}\cos(q_0),\end{aligned} \tag{5.22}$$

$$\dot{p}_j = -(p_j^2+q_j^2)q_j-q_{j-1}-q_{j+1}, \tag{5.23}$$

$$\dot{q}_j = (p_j^2+q_j^2)p_j+p_{j-1}+p_{j+1}. \tag{5.24}$$

In the equations from (5.17)-(5.24), one has neglected the secular terms $D^{\varepsilon}_{x_1}$ and $D^{\varepsilon}_{y_1}$. The truncations have been kept up to the same orders as the averaged system derived at (5.11)-(5.14). The new equations however, should make it easier to construct

a Hamiltonian from which they can all be generated, similar to its parent Bose-Hubbard Hamiltonian from (5.15).

Since we want the dynamics to be given by an averaged Hamiltonian, H_{av}, it must be that

$$\begin{aligned} \dot{p}_j &= -\partial_{q_j} H_{av} \\ \dot{q}_j &= \partial_{p_j} H_{av}, \end{aligned} \tag{5.25}$$

$\forall j \geq 0$. This implies that the effective Hamiltonian can be constructed by adding contributions of the type

$$\begin{aligned} H_{av}\Big|_{partial} &= -\int dp_j \dot{q}_j + F \\ H_{av}\Big|_{partial} &= \int dq_j \dot{p}_j + G, \end{aligned} \tag{5.26}$$

where F is a function which is independent of p_j ($\partial_{p_j} F = 0$), and G is a function which is independent of q_j ($\partial_{q_j} G = 0$). Applying these formulas on all the eight approximate derivatives from (5.17)-(5.24), one will obtain all the required terms in an effective Hamiltonian which generate the approximate slow derivatives. The effective Hamiltonian will be given by

$$\begin{aligned} H_{av} &= \tfrac{1}{4}\textstyle\sum_{j>0}(p_j^2+q_j^2)^2 + \\ &+ \textstyle\sum_{j>0}(p_j p_{j+1} + q_j q_{j+1}) + \tfrac{1}{2}\ln(p_0) - \\ &- \tfrac{1}{\sqrt{2p_0}}\Big\{\big[q_1(p_1^2+q_1^2)+q_2\big]\sin(q_0) + \\ &+ \big[p_1(p_1^2+q_1^2)+p_2\big]\cos(q_0)\Big\} + \\ &+ \tfrac{1}{2p_0}\big[p_1 q_1 \sin(2q_0) + \\ &+ \tfrac{1}{2}(p_1^2-q_1^2)\cos(2q_0) + \\ &+ \tfrac{3}{2}(p_1^2+q_1^2)\big], \end{aligned} \tag{5.27}$$

which will dictate the trajectory of the averaged system. This new Hamiltonian contains two terms which are identical to those in the original Bose-Hubbard Hamiltonian at (5.15). All the additional terms present in (5.27) describe the weak interaction between the breather and its neighbours.

The final averaged differential equations will be

$$\begin{aligned}\dot{p}_0 &= \tfrac{1}{\sqrt{2p_0}}\Big\{\big[q_1(p_1^2+q_1^2)+q_2\big]\cos(q_0)- \\ &\quad -\big[p_1(p_1^2+q_1^2)+p_2\big]\sin(q_0)\Big\}+ \\ &\quad +\tfrac{1}{2p_0}\big[(p_1^2-q_1^2)\sin(2q_0)-2p_1q_1\cos(2q_0)\big]\end{aligned} \tag{5.28}$$

$$\begin{aligned}\dot{q}_0 &= \tfrac{1}{2p_0}+ \\ &\quad +(\tfrac{1}{2p_0})^{3/2}\Big\{\big[q_1(p_1^2+q_1^2)+q_2\big]\sin(q_0)+ \\ &\quad +\big[p_1(p_1^2+q_1^2)+p_2\big]\cos(q_0)\Big\}- \\ &\quad -(\tfrac{1}{2p_0})^2\times 2\big[p_1q_1\sin(2q_0)+\tfrac{1}{2}(p_1^2-q_1^2)\cos(2q_0)+ \\ &\quad +\tfrac{3}{2}(p_1^2+q_1^2)\big]\end{aligned} \tag{5.29}$$

$$\begin{aligned}\dot{p}_1 &= -(p_1^2+q_1^2)q_1-q_2+ \\ &\quad +\tfrac{1}{\sqrt{2p_0}}\Big\{(p_1^2+3q_1^2)\sin(q_0)+2p_1q_1\cos(q_0)\Big\}+ \\ &\quad +\tfrac{1}{2p_0}\big[q_1\cos(2q_0)-p_1\sin(2q_0)-3q_1\big]\end{aligned} \tag{5.30}$$

$$\begin{aligned}\dot{q}_1 &= (p_1^2+q_1^2)p_1+p_2- \\ &\quad -\tfrac{1}{\sqrt{2p_0}}\Big\{(3p_1^2+q_1^2)\cos(q_0)+2p_1q_1\sin(q_0)\Big\}+ \\ &\quad +\tfrac{1}{2p_0}\big[p_1\cos(2q_0)+q_1\sin(2q_0)+3p_1\big]\end{aligned} \tag{5.31}$$

$$\begin{aligned}\dot{p}_2 &= -(p_2^2+q_2^2)q_2-q_1-q_3+ \\ &\quad +\tfrac{1}{\sqrt{2p_0}}\sin(q_0)\end{aligned} \tag{5.32}$$

$$\begin{aligned}\dot{q}_2 &= (p_2^2+q_2^2)p_2+p_1+p_3- \\ &\quad -\tfrac{1}{\sqrt{2p_0}}\cos(q_0)\end{aligned} \tag{5.33}$$

$$\dot{p}_j = -(p_j^2+q_j^2)q_j-q_{j-1}-q_{j+1} \tag{5.34}$$

$$\dot{q}_j = (p_j^2+q_j^2)p_j+p_{j-1}+p_{j+1} \tag{5.35}$$

which are now fully Hamiltonian, and can be used in micro-canonical numerical simulations where the system is set to evolve at the intersection of two hyper-surfaces, one of constant norm and one of constant effective energy. Equations (5.28)-(5.35) will be referred to as the Average Nonlinear Schrödinger Equation, also abbreviated as the AvNLSE.

At this stage, it is relevant to look at the evolution of the mass of the condensate according to the newly derived differential equations. Ideally, the new equations should not artificially create or destroy mass. If we use the convention that $d_t(*)$ dictates the evolution of the system as it is given by the DNLSE (the evolution operator of the Bose-Hubbard Hamiltonian) and that $\dot{(*)}$ dictates the evolution of the system as it is given by the effective Hamiltonian from (5.16), we arrive to the following remarkable identity for micro-canonical set-ups:

$$d_t\mathcal{N} = \dot{\mathcal{N}} = 0, \tag{5.36}$$

which means that the new system conserves norm just as the initial DNLSE. Therefore, no matter how long the simulation will run for, mass will not be created or annihilated artificially when employing the new effective Hamiltonian from (5.27). Identity (5.36) was derived by applying $d_t(*)$ and $\dot{*}$ on the definition of the norm $\mathcal{N} \equiv I_0 + \frac{1}{2}\sum_{j\geq 1}(p_j^2 + q_j^2)$.

One cannot write a trivial identity like (5.36) for energies, since the two system are clearly characterised by different Hamiltonians. Moreover, the two trajectories separate by velocities given by

$$\begin{aligned} d_t H_{av} &= \mathcal{O}(\varepsilon^{1/2}) \\ \dot{H}_{BH} &= \mathcal{O}(\varepsilon^{1/2}), \end{aligned} \tag{5.37}$$

which implies that after one full breather rotation the two hyper-surfaces have separated by a distance of order $\mathcal{O}(\varepsilon^{3/2})$. Even if the energy hyper-surfaces cannot coincide, the effective Hamiltonian can still create a numerical algorithm which approximates the

full trajectory reasonably well, and during much shorter running times. Now that the effective Hamiltonian was constructed, it is useful to define its domain of applicability, and investigate how this quantity can be used to fasten up the integration of the DNLSE.

5.3 Effective Hamiltonian vs. Bose Hubbard Hamiltonian

The averaged equation was built under the assumption that the dynamics of the breather are much faster than those of the lattice. Additionally, one made the assumption that the breather is pinned at site $j = 0$ and no translations can occur during the evolution. Figure 5.1 shows the evolution of a closed system consisting of a breather in a lattice of length $N = 4$, where the breather sits at site $j = 0$, just as in the case of the theory developed in the previous chapters. Diagram (a) shows the evolution according to the Bose-Hubbard model (5.15): the breather is very stable and only the wave-function at site $j = 1$ shows some reminiscence of the fast harmonics induced by the breather rotation. In diagram (b) of Figure 5.1 one sees the evolution of the same system under the action of the effective Hamiltonian from (5.27). One can see that for approximately $\mathcal{O}(10)$ units, the two trajectories are very close, and then, due to the chaotic nature of the background dynamics, a clear separation occurs, just as one might expect from the action of the separation velocities at (5.37). Nevertheless, the averaged differential equation produces the same sort of decoupling as the full DNLSE, generating trajectories where the breather acts as a reflective boundary, interacting very weakly with its surroundings. This is consistent with the weakly non-ergodic trajectories described in [70]. In addition, if one puts the lattice in contact with Langevin heat baths at site $j = N - 1$, one can see that the two Hamiltonians produce identical profiles for the amplitudes of the background. These initial findings show a good agreement between the evolutions given by the Bose Hubbard Hamiltonian and those obtained through the faster integration of the Effective Hamiltonian.

We now study what happens in the case when the background is large enough to significantly disturb the breather and how the averaged system reacts when encountering these abnormally large perturbations. This scenario is encompassed by the trajectories depicted in Figure 5.2. One can now see that while the DNLSE (a) gives rise to scenarios when the breather strongly interacts with its surroundings, the AvNLSE (b) artificially enhances the stability of the breather, limiting the flow of energy from the breather to its surroundings. In addition, while inset (a) shows an evolution where the location of the maximum excitation changes with time, inset (b) generates an evolution where the location of the maximum excitation does not change at all, even in the presence of large perturbations. In addition, it was impossible to observe the complete decay of a breather when the effective Hamiltonian was employed. This is not surprising, given the fact that the expression of the new Hamiltonian (5.27) diverges when $A \to 0$, which implies that an infinite amount of energy has to be spent to make the breather decay.

It now becomes apparent that the effective Hamiltonian cannot capture the full dynamics of the system, and at this stage one will want to make use of a Heterogeneous Multiscale Integration method, like those presented in Ref. [64] where most of the trajectory is described by the use of a fast macro-integrator (here given by the Effective Hamiltonian at (5.27)), and occasionally by a slow micro-integrator (the Bose Hubbard Hamiltonian at (5.15)) which will only be employed when the state is in the proximity of a topological aberration where the macro-integrator would fail to generate a realistic trajectory. While the expressions for the two Hamiltonians are now known, it is still not clear at this stage what is the exact nature of these singularities.

5.4 Diffusion of the breather norm

In addition to the discrepancies which occur in the presence of rare excitations like those depicted in Figure 5.2, one also has the artificial diffusion of the breather norm induced by the averaged system. The truncations in the effective Hamiltonian at (5.27)

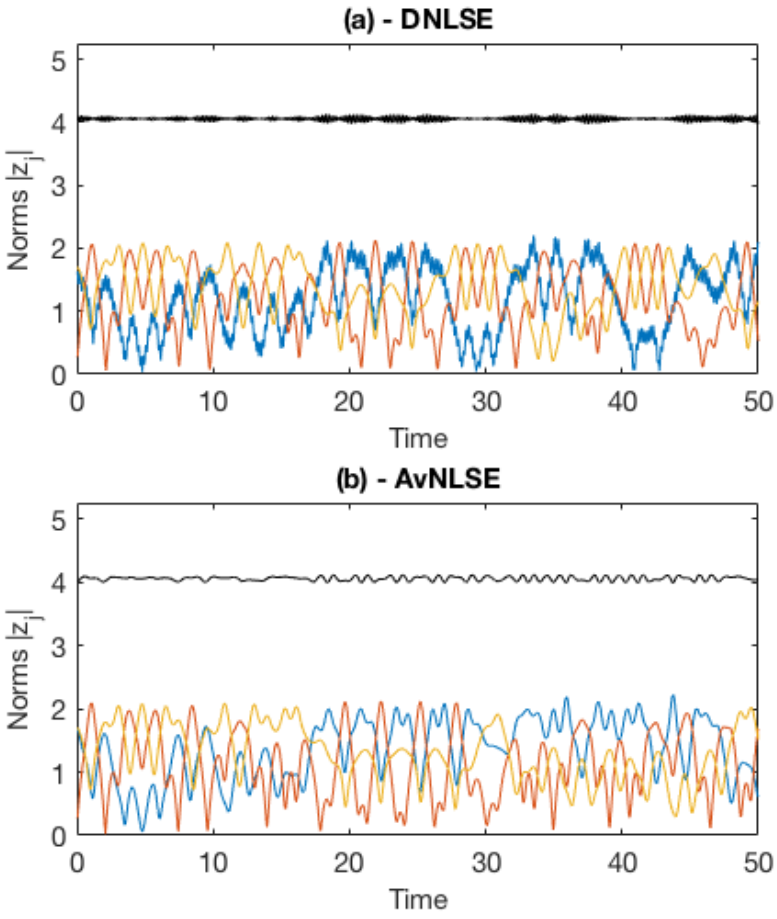

Figure 5.1: Time evolution of a four-mer as given by the DNLSE (a) and according to the averaged differential equation (b). The breather norm is depicted in black, the nearest neighbour norm in blue, and the norms for the second and third neighbours in red and yellow receptively.

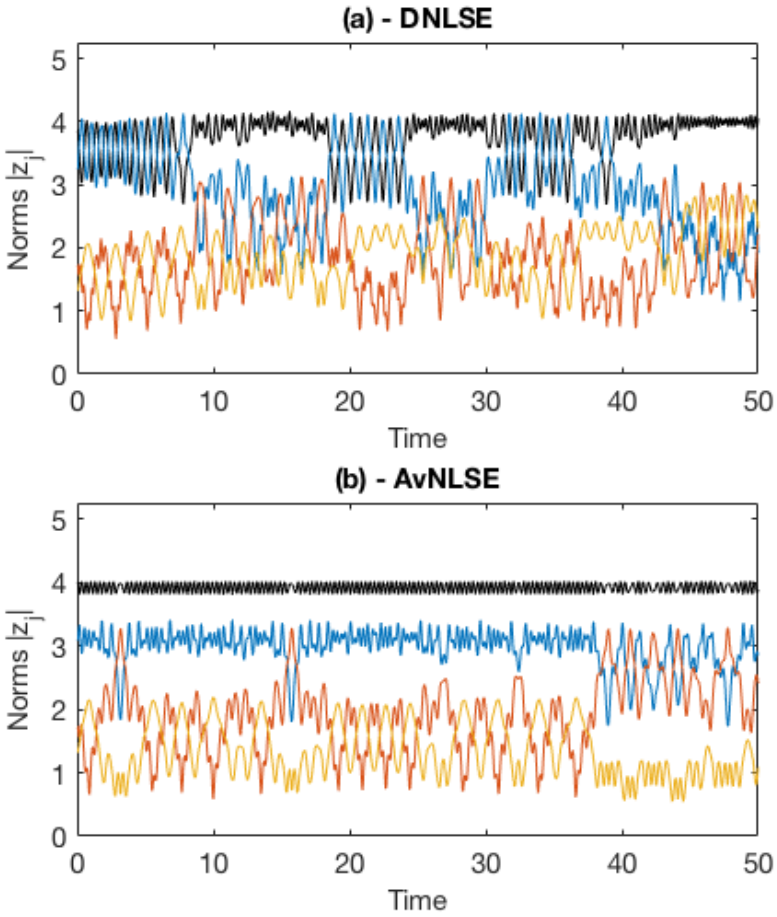

Figure 5.2: Time evolution of a 2^{nd} four-mer system. The colours have the same meaning as in Figure 5.1. Here, however the interactions are strong enough to break the assumptions required to derive an averaged equation.

have been done in such a way to minimise diffusion while still keeping a reduced amount of terms in the differential equations, so that the numerical integration of the averaged model is faster than that of the full DNLSE.

Diffusion here means a drift in the breather intensity. The system starts with a breather of height $|z_0(0)|$, which will evolve in time according to the numerics given by the effective Hamiltonian (5.27). The breather will interact weakly with its surroundings and this will cause fluctuations in the breather height. We can measure numerically how these fluctuations accumulate over time, by looking at how the variance of the drifts evolves. This means that we evaluate

$$C(\tau) \equiv \langle (|z_0(t+\tau)| - |z_0(t)|)^2 \rangle \tag{5.38}$$

where τ is a time separation which can only range from one single time step (the resolution available from the numerics) up to the whole time-span of the simulation. In reality, due to the very long times used in the simulations, of order $\mathcal{O}(1)$, we only sample the data at each $\Delta\tau = 1$ units. From this, we get enough data to generate the function at (5.38). A more dense sampling would slow down the simulation considerably, while taking a lot of disk space. In addition to this, it would not give more information on the diffusion process. Therefore τ will practically range between 1 and the whole time-span of the simulation. At the same time, it is important to notice, that while for $\tau = 1$ we have a lot of data to calculate the average $C(\tau) \equiv \langle (|z_0(t+1)| - |z_0(t)|)^2 \rangle$, when τ is equal to the full time-span of the simulation there is only one pair which can be used in the average. We can deduce from this that as τ is increased, the value of $C(\tau)$ generated from the numerics becomes less trustworthy. The cut-off for τ was usually taken at $T_{span}/80$, because up to that value, there is enough data to generate very reliable results. However, this requires very long integration times, of the order $\mathcal{O}(10^7)$. Therefore evaluating the dependency of $C(\tau)$ is quite computationally expensive, but important in studying diffusions.

If we assume all correlations to be short ranged, which here means that after $\Delta\tau = 1$ all values are not correlated, we have the identity

$$\langle |z_0(t+\tau)| - |z_0(t)| \rangle = 0. \tag{5.39}$$

This property, together with the definition from (5.38) allows us to make the equivalence between the growth of variance with time and the value of $C(\tau)$, from the very definition of variance $\sigma^2 \equiv \langle X^2 \rangle - \langle X \rangle^2$.

In order to evaluate the diffusion of the breather norm induced by the effective Hamiltonian, one has let the system evolve for times of the order 10^6 and beyond for different values of the initial breather norm. The system studied here was in a symmetrical configuration, with Langevin heat baths [50] at $T = 10$ and $\mu = -6.4$. At this stage, the effective Hamiltonian has been extended to breathers with backgrounds on both sides, by adding two contributions of the type (5.27). The effective Hamiltonian has this additive property, which can be checked analytically by performing the same exact averaging procedures described at the beginning of this chapter, but for systems with symmetric configurations (with at least three background sites on each side od the breather). Using the same `Mathematica` spreadsheets, one can arrive to similar averaged equations and to an equivalent effective Hamiltonian. The symmetric Hamiltonian is the addition of left/right contributions of the sort seen in (5.27). The only additional term is a tunnelling from left to right, which only appears between sites $j = 1$ and $j = -1$. Like in the case of the Multiple Time Scale Analysis (MTSA) algorithm, this term appears at order $\mathcal{O}(\varepsilon)$, and will be neglected for simplicity reasons. One has already seen that the MTSA offers a very good approximation of the slow manifold, even if all tunnelling from one side to the other of the soliton is omitted. Similarly, the symmetric AvNLSE can be employed successfully in Heterogeneous Multiscale Numerical Methods without the need to add tunnelling terms between the two backgrounds.

For different initial heights of the breather, one has calculated the variance $C(\tau) \equiv \langle(|z_0(t+\tau)| - |z_0(t)|)^2\rangle$ and looked at the slope with which this variance increases with τ. The value of this slope will be the diffusion coefficient D.

The diffusive process is generated by a flow of probability density (denoted by Φ) given by the heat equation

$$\frac{d}{dt}\Phi = D\frac{d^2}{dN^2}\Phi \tag{5.40}$$

where $N = |z|$ is the norm of the breather. In the simplest modelling, D is just a number and there is no dependency on N or t. In that case, the solution will be given by the Ansatz

$$\Phi(N,t) = \frac{1}{\sqrt{4\pi Dt}}\exp\Big[-\frac{(N-N_0)^2}{4Dt}\Big], \tag{5.41}$$

where N_0 is just the initial amplitude of the breather.

This means that as time passes, we have less information about the breather height, which diffuses under a stochastic process. Initially, the probability density is $\delta(N - |z(0)|)$, therefore we know the height exactly from the initial condition. As time passes the variance increases linearly, but still the average height is

$$\langle|z(t)|\rangle = \langle N\rangle = \int_{-\infty}^{+\infty} dN \;\; N \;\; \Phi(N,t) = N_0, \tag{5.42}$$

which is time independent. Therefore, the average height does not change in time through this diffusive process. This observation is important, since usually by diffusion in the physics community we refer to the spread of atoms in the lattice, and therefore the decay of the central peak. This clarification is introduced to make sure that the terminology is properly defined.

The results for the measurements of the diffusion coefficients are summarised in Figure 5.3 showing that the diffusion produced by the effective Hamiltonian decreases with $|z_0|^2$ (the mass of the breather) by a power law with an exponent of approximately

-6. Therefore, in our model, the diffusion is not characterised by a constant diffusion D, but by a more complex equation than the normal diffusion equation (5.40). However, over very long periods of time, the diffusion coefficient is relatively unchanged (since the breather norm is frozen, and the diffusion coefficient is a function of the norm) and the breather norm undergoes a random walk below and above the initial value, with a zero average drift.

Even if the DNLSE generates diffusion which scales exponentially (as one can see in Figure 5.3), and not as power law like in the case of the newly obtained equation, one can still successfully employ the effective Hamiltonian in hybrid integration schemes, as will be shown in Chapter 6. The larger diffusions generated by the effective Hamiltonian lead to higher standard deviations in the breather lifetimes, but not to different average life-times. This comes from the fact that diffusion here does not mean a decay, but a slow random drift in height. As a matter of fact, due to the fact that the average height does not change in time, any decay time from diffusion would be infinite. In addition to this, as the diffusive process continues for very long times, the Gaussian solution from (5.41) flattens so much that the probability density becomes almost constant, and the variance diverges. This means that the average is no longer defined for long times, and that the central limit theorem is violated. This simplistic Ansatz, however, assumes a Gaussian distribution of the probability density function. Part of the tail of the Gaussian sits in the domain $N < 0$ at all times, and the values associated with this domain are not physical. Even if we cannot necessarily extrapolate the Gaussian model to infinite times, it is still enlightening to use it for short to medium times, and to deduce that overall there seems to be no drift in the breather amplitude. This simplified theoretical model is confirmed by the simulations, which do not seem to show a clear drift which is purely caused by diffusion.

Note 1: The diffusion can also be evaluated by calculating $C(\tau) \equiv \langle (Q(t+\tau) - Q(t))^2 \rangle$, where Q is the less oscillating component of $z_0(t)$, which was defined at (4.73).

This would not change however, the results for the diffusion law, but it would only lead to cleaner slopes when measuring the growth of the variance, since all oscillating terms would have been eliminated.

Note 2: Here, instead of calculating the algebraically complex value of Q at every sampling point, we simply average the breather norm over every 500 time units, to get rid of the fast fluctuations on top of the signal. The effect is the same as calculating Q, but the algorithm is much faster, since the number of operations is reduced. Alternatively, one could save all the wave-functions at sites $j \in \{-1, 0, 1\}$ (6 variables) and calculate Q when the diffusion data is analysed, but this would increase the size of the output files considerably. Therefore, the preferred method is to save $A_0(t)$ at every sampling point, and ultimately perform averages over 500 time units when looking at diffusions.

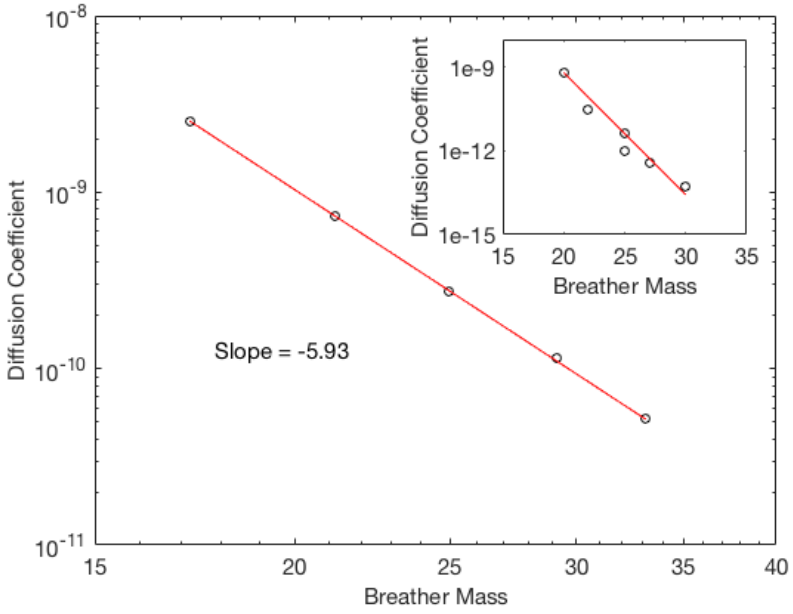

Figure 5.3: Diffusion of the breather norm ($\arctan(C(\tau)/\tau)$) vs initial mass ($|z_0(0)|^2$). The diffusion scales down according to a power law with with exponent ≈ -5.9. The inset shows the diffusions of the full DNLSE model (data provided by Antonio Politi).

5.5 Adiabatic Invariants and strong interactions with the background

It is now important to understand the mechanisms through which excitations from the background strongly interact with the breather.

During the laminar periods, the background is basically at equilibrium with a temperature and a chemical potential set by the external reservoir. Accordingly, the background itself can be interpreted as an effective thermal bath, which interacts directly with the breather. Fluctuation-dissipation considerations then suggest that the interaction should be characterized by a diffusion coefficient that can be identified with D, and a drift v, responsible for the eventual absorption of the breather. In fact, for $T > 0$ the equilibrium state of the DNLS is statistically homogeneous, with no breathers. According to the same fluctuation-dissipation considerations, v is expected to be proportional to D/T, as also confirmed by explicit calculations for a simple model [53].

Where does the slowness of the relaxation process come from? One cannot, strictly speaking, invoke a gap in the spectrum between the frequency of the breather and the surrounding waves, because the nonlinear nature of the background implies a broadband spectrum. One might still naively trace back the slowness to the small amplitude of the background power spectrum at the breather frequency. However, this is not the case; we have tested that a pure and simple interaction of the breather with a stochastic process characterized by the same power spectrum of the background gives a far faster relaxation, so that it is necessary to account for the effects of the breather on the background itself.

Mathematically speaking, one reason for the non perfect invariance of an adiabatic invariant is the lack of convergence of perturbative expansions, which occasionally happens whenever the amplitude in the breather neighbouring sites is very large.

In order to quantify this phenomenon, we have computed $\Delta E = \overline{|\Delta|z_0|^4|}$, where $|z_0|^4(t)$ is the breather energy, while ΔE indicates its variation after 50 time units.

The breather, of initial mass $|z(0)|^2 = 36$, is set on the left boundary of the chain (no coupling with the left neighbour), while the rightmost 8th site is thermalised at $T = 10, \mu = -6.4$. Finally, the mass of site 1 is set equal to $|z_1(0)|^2 = r|z(0)|^2$. A plot of ΔE as a function of r shows a clear peak (see Figure 5.4 at $r_d = (|z(0)| - \sqrt{2})^2/|z(0)|^2$ (see the vertical line); it corresponds to the activation threshold for the formation of a symmetric, two-site, localized structure. Analogously to the breather, the localized-structure is weakly coupled with the background when the amplitude of both sites is large enough. Therefore, it can be approximately treated as a dimer configuration with open boundary conditions and, from now on, we refer to it simply as to a *dimer*.

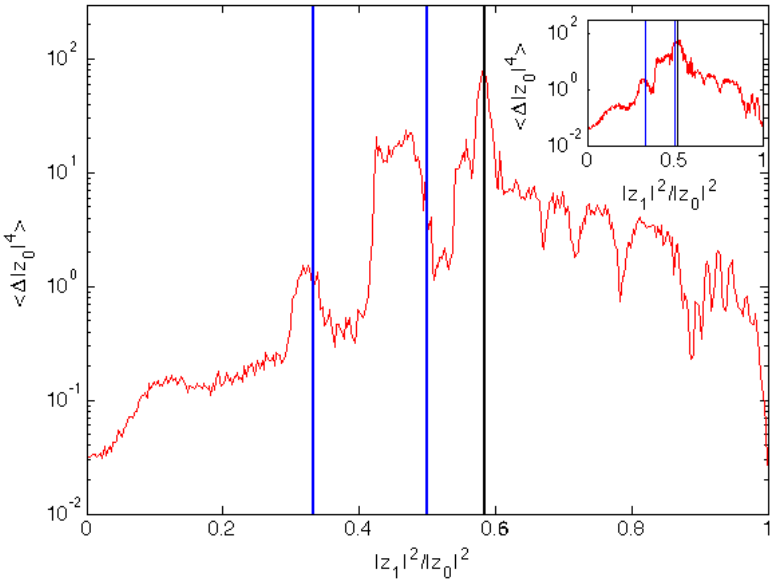

Figure 5.4: Interactions between a breather of size $|z_0(0)| = 6$ and its three nearest neighbours. The horizontal axis displays the ratio between the frequencies $|z_j|^2/|z_0|^2$, while the vertical axis displays the average change in Hamiltonian for the breather rotation $\langle\Delta|z_0|^4\rangle$. The inset shows the same interactions for breathers of height $|z_0(0)| = 5$.

Symmetric dimers are characterized by periodic oscillations of the mass between $min(|z_0|^2)$ and $max(|z_0|^2)$ [44]. Additionally, for a given $m_{tot} = min(|z_0|^2) + max(|z_0|^2)$, there exists a minimal $min(|z_0|^2)$ for the oscillations to self-sustain. This is the origin of the above mentioned threshold r_d for the ratio r.

The onset of symmetric dimers is not the only means to transfer mass out of a breather. By looking at Figure 5.4, one can see additional peaks, which approximately coincide with resonances, where the frequency on site 1 is equal to $1/3$ (r_3) or $1/2$ (r_2) of the breather frequency. Although the single resonance events are not so effective, they are much more frequent than dimer-formation events and might be relevant for "killing" the adiabatic invariant [61]. The relative weight of the two relaxation mechanisms (dimers and resonances) with varying $|z(0)|^2$ is still unclear.

All of our studies in [69] consistently give evidence of an exponentially slow relaxational dynamics. The origin of such freezing process is very different from the arrest mechanisms typically encountered in statistical mechanics: it has a purely dynamical origin, being enforced by the existence of an adiabatic invariant (AI). For $T > 0$, the AI neutralizes entropic forces, preventing *de facto* a macroscopic relaxation as soon as one tall breather is contained in the initial configuration. Indeed, in the presence of an exponentially weak effective breather-background interaction, breather condensation proceeds through a practically unobservable logarithmic coarsening [53]. In the negative-temperature region, the same mechanism prevents breather growth, thereby "stabilizing" a fairly homogeneous chaotic non-ergodic dynamics, as suggested by recent direct numerical simulations [49, 54].

The findings arising from our Multiple Time Scale Analysis (MTSA) (presented in detail in Chapter 4 and in our paper from Ref. [77]) suggest that the breather norm is an adiabatic invariant, which is defined as a quantity that changes no more than $\mathcal{O}(\varepsilon)$ over time-spans of $\mathcal{O}(1/\varepsilon)$ [78]. We have shown that the derivative over one full rotation is of order $\mathcal{O}(\varepsilon^2)$ in equation (4.62). Integrating this over a time of $1/\varepsilon$ will lead to a drift no larger than $\mathcal{O}(\varepsilon)$. According to the simplistic definition given by Ref. [78], this indicates that we are in the presence of an adiabatic invariant. We already know from our simulations that the breather norm barely changes over very long integration times, acting as 'effectively' invariant.

The literature [60, 61] suggests that even if adiabatic variants remain unchanged

for very long times, they can suddenly be destroyed by a passage through resonance. During our research on the nature of extreme events in Chapter 3, we have seen that resonances do play a crucial role in the sudden change of the breather shape. In Chapter 3, we used the fact that the breather frequency is given by $\omega \approx 2|z_0|^2$, and we defined resonant hyper-surfaces as pairs of two interacting oscillators which satisfy the equation $k_1\omega_1 + k_2\omega_2 = 0$ (where k_1 and k_2 are integers). Resonances are encountered therefore when one of the breather's nearest neighbours reaches any value in the set $\{|z_0|/\sqrt{2}, |z_0|/\sqrt{3}, |z_0|/\sqrt{4}, ...\}$. This hypothesis is confirmed by the findings presented Figure 5.4.

When the breather neighbour reaches the intensity $|z_0|^2/2$, it will rotate with a frequency $\omega_1 \approx \omega/2$. This allows us to write a differential equation for the breather amplitude in the vicinity of the resonance, just as was done in Chapter 3.2

$$d_t A_0 = \frac{\sqrt{\omega}}{2} \sin\left(\frac{\omega}{2}t + \xi_0\right) \tag{5.43}$$

where ξ_0 is the initial breather phase. Applying the partial averaging near resonance algorithm developed at 3.24, we obtain the drift in the presence of a resonant hyper-surface

$$\delta A_0^{(1)}|_{t=2\pi/\omega} \approx 2\sqrt{\varepsilon}\cos(\tilde{\xi}_0). \tag{5.44}$$

This is in perfect agreement with the theory from [61], which predicts jumps of order $\mathcal{O}(\varepsilon^{1/2})$ in the proximity of a resonant hyper-surface. It also offers a theoretical explanation for the massive peak observed for the ratio $|z_1|^2/|z_0|^2 \approx 0.5$ in Figure 5.4. We now know from the MTSA, that the same drift in the absence of a resonance is of a height which cannot exceed $\mathcal{O}(\varepsilon^3)$ (since the derivative over one rotation is of order $\mathcal{O}(\varepsilon^2)$ and it has to be multiplied with $2\pi\varepsilon$ to estimate the size of the drift in the laminar regime).

When performing averaging, there seems to be domains where the adiabatic invari-

ant assumption breaks down. Upon further investigation, it appears that the breakdown coincides with the spontaneous emergence of resonances with sites in the background. This is compatible with the theory presented in the literature [61], where it is stated that adiabatic invariants can strongly change when the state of the system is in the vicinity of a resonant hyper-surface. Even if some of the changes we see are not related to resonances at all (such as it is the case with the emergence of bound states), all focus will now be shifted towards the dominant resonance present in the system, at $m \equiv \frac{A_0^2}{A_1^2} = 2$.

This main resonance will be used extensively throughout the next chapters to define numerical transitions between the Bose-Hubbard Hamiltonian (5.15) and the effective Hamiltonian (5.27) obtained in this chapter. These transitions will be used to create fast, reliable numerical algorithms which perform much faster than what is currently available in the literature.

Note: One can determine higher order terms of the adiabatic invariant from the equation

$$\{H, Q\} = 0 \tag{5.45}$$

where H is the Bose-Hubbard Hamiltonian and $Q \equiv Q_0 + \varepsilon Q_1 + \varepsilon^2 Q_2 + ...$ is the asymptotic expansion of the adiabatic invariant. This equation ensures that Q is exactly conserved up to a certain order (depending on the number of terms kept in the truncation) of the smallness parameter when the system evolves according to the DNLSE. The first term will be the breather mass, i.e. $Q_0 \equiv A_0 = |z_0|$, and the rest will be determined from setting the Poisson bracket from (5.45) to zero. We are not interested however, in the higher order terms of the invariant, just in the fact that it can be destroyed by a passage through resonance. This property will be used repeatedly in Chapter 6, where a Hybrid Integration technique will be developed.

Chapter 6

Heterogeneous Multiple Time Scale Methods - Hybrid Integration Schemes and Multiple Breather Systems

6.1 Single Breather systems

6.1.1 Building a Hybrid Integration Scheme

It is now possible to build a hybrid integration scheme like the ones introduced in Ref. [62] where the Effective Hamiltonian derived in (5.27) is used whenever the three nearest neighbours of the breather are oscillating with frequencies below the first resonance frequency given by $|z_0|^2/2$. Since the breather amplitude is much larger than the average amplitudes of the background, the breather will remain unchanged for the largest part of the integration time. In Chapter 3 we have seen that interactions with neighbours further than three sites away are effectively negligible. We have also seen that the averaged integrator does a very good job at generating fast trajectories, which

are very similar to those produced by the full model (see a sample of the detailed numerical analysis in Figure 5.1). Due to this property, we can define the AvNLSE (5.28)-(5.35) model as a macro-integrator of the DNLSE. The AvNLSE will project the state very fast, using time steps which are much larger than those normally used in the classical integrator (the micro-integrator). As a matter of fact, these time steps would only depend on the size of the background, and would be completely independent of the breather size. The AvNLSE on its own cannot generate a reliable trajectory of the breather evolution, due to the fact that it artificially enhances soliton stability in the vicinity of a resonance. One must therefore identify the trigger of a rare event and make the transition to the full DNLSE whenever the state is in the vicinity of a resonant surface. However, when this transition is made, one will make use of very small time steps, which will depend on the size of the breather. The Bose-Hubbard Hamiltonian (5.15) is able to generate the full trajectory, and requires very small time steps in the presence of large breathers. In this context, it can also be referred to as a micro-integrator.

The Effective Hamiltonian (5.27) was expanded to accommodate lattices with symmetrical configurations; therefore one must track six neighbours when transitioning from one Hamiltonian to the another ($j \in \{-3, -2, -1, 1, 2, 3\}$). The Effective Hamiltonian will therefore be used until any of these six sites reaches the occupation number $|z_j| = |z_0|/\sqrt{2}$. During the evolution given by the Effective Hamiltonian, the location of the breather is fixed, only its size changes very slowly, due to the weak coupling between the background and the breather that was included into the truncation of the averaged equations. However, during parts of the algorithm, the DNLSE will be used as an integrator, so that the breather will be allowed to change location, and to dramatically alter its height when the trajectory is in the proximity of a resonant hypersurface. If we were to use the DNLSE by itself (the classical numerical approach), the breather might also encounter the separatrix of bound states, and might suddenly jump to a neighbouring site, but this is not a phenomenon which is considered relevant in

the hybrid model, since adiabatic invariants are usually destroyed by passage through resonance [61]. One will see, that even if we ignore bound states (peak locations dependent on the breather height), and only focus on resonances (peak locations completely independent of the breather height), we will obtain very realistic trajectories for the breathers, throughout their entire lifetimes.

The DNLSE is employed until all the six nearest neighbours (three on the left, and three on the right) decay under the value $\mathcal{O}(1)$ and the program never exits the DNLSE unless the breather oscillates for an integer number of periods (i.e. its phase is as the initial value modulo 2π within a tolerance level of 10^{-4}). This very strict condition was imposed to make sure that no rare events were artificially missed, and all the slow variables had been allowed to fluctuate for an integer amount of periods to avoid artificial jumps which come from large fluctuations from the breather harmonics. These fluctuations are avoided by making sure that the breather is allowed to close the orbit before exiting the DNLSE and returning to the AvNLSE. The third neighbour was also included when testing for potentially destructive events, even though the transition peaks from Figure 5.4 do not extend this far. This was done, once again to make sure that no potential rare events were artificially missed. With all these considerations, the Hybrid Integration scheme performs on average five times faster than the full model. If one would spend less time in the DNLSE scheme (the slow part of the system), this speeding up factor could be enhanced even more. This could be done by removing some of the strictest constraints such as: not requiring all six neighbouring sites to decay under the value of 1 simultaneously and not having the breather oscillate for an integer number of times simultaneously, since all these events at once are very rare. However, if one were to relax the conditions, all the calibrations and tests would need to be repeated. The average running time for these tests was four months. The main purpose of the tests is to make sure that the trajectories given by the Hybrid Integrator are realistic, and that the decay times have the same order of magnitude as in the case of the DNLSE. In addition, one also wants the decay times to scale in the same way

as for the Bose-Hubbard Hamiltonian, i.e. one is looking for an exponential increase of life-times with the breather mass.

If we define the transitions from one integrator to the other as is done in this chapter, we will prove that we can build a very reliable Hybrid Integration Scheme. In order to confirm this, we must first go through the numerical tests, and to analyse their physical meanings and their similarity to the original model. Just as in the case of choosing and effective Hamiltonian, the choice of these conditions is not unique, and one can define other transition conditions from one integrator to the other. However, one must ensure first that any Hybrid Integration Scheme obeys similar trajectories to those of the full DNLSE.

When using the Hybrid Integration scheme one must use a lattice which is long enough to avoid limited size effects which occur when generating Langevin heat baths. The choice made in this thesis was to investigate lattices with $N = 15$, where the breather was initialised at the middle of the lattice. When the breather transitions from one Hamiltonian to the other, it will not return on the same hyper-surface as it started. This is not an issue however, when the system is put into contact with Langevin heat baths, since in this set-up, the Hamiltonian is not conserved during the evolution, and the distances in the hyper-surfaces in between two consecutive shifts are much smaller than the characteristic fluctuations induced by the heat baths.

The literature [62] shows multiple ways of building Hybrid Integration Schemes.

- One could employ predictor-corrector methods, which significantly decrease the time step in the vicinity of an extreme event, and use consecutive shifts between the macro-integrator and the micro-integrator at each time step [79,80]. When the micro-integrator solution leads to very large fluctuations, the macro-integrator is abandoned, and a transition to the initial system is used. The advantage of this approach is that one does not need to define beforehand what an extreme event is, it would just be detected ad-hoc by the velocity of the micro-integrator. This approach would be slower however than what is currently employed.

- One could also run the micro-integrator for a fixed number of steps and then shift to the macro integrator for one single step [62–64]. This approach has failed though for this system, since it seems to be more appropriate with systems where there are no topological aberrations, such as resonances. Any attempt to use this method (which is the canonical approach for HMM in literature) has been abandoned in favour of the algorithm described in this chapter.

6.1.2 Results produced by the Hybrid Integration Scheme

The advantage of the Hybrid Integration scheme is that, during the time which it uses the Effective Hamiltonian (which is during most of the trajectory) it employs a large time step, which is independent of the breather size. This means that the integrator works equally fast for large breathers as it does for small ones. This is starkly different from what happens when one uses the DNLSE, where the time step must decrease proportionally with the inverse square of the breather norm. The life-times of breathers scale exponentially with their initial norm, making large breathers to be astronomically long-lived. The exponential increase of life-times, combined with the need to use very small time steps, makes the simulation of full life-times close to impossible for large breathers. This is where the need for a more rapid hybrid integration scheme arises from. At this stage, it is important to test whether the newly built integrator can generate trajectories which are close to the physics dictated by the DNLSE.

In order to compare the two integrators, breathers of different sizes have been allowed to evolve in contact with backgrounds at temperature $T = 10$ and chemical potential $\mu = -6.4$. Breathers of initial mass $|z_0(0)| \in \{12, 13, 14, 15, 16, 17, 18\}$ have been tracked until their full decay for both algorithms. The results are summarised in Figure 6.1. The plot in the upper part (a) shows the same evolutions as recorded in Figure 2.7, where the breathers were allowed to evolve according to the full DNLSE. Unlike in Figure 2.7, we are now plotting the norms of the breathers (i.e. $|z_0(t)|^2$), and

not their Hamiltonians (i.e. $|z_0(t)|^4$), but the diagram is based on the same data. It is useful to remember here that larger breathers live exponentially longer than smaller ones, which was one of the earliest findings of this work, obtained using numerical methods.

We now focus on sub-plot (b) of Figure 6.1, where we observe remarkably similar trajectories to those generated by the full model. In both cases, we are tracking the maximum norm in the lattice and the location of the maximum changes several times throughout the simulations. The most important finding is that the Hybrid Integrator, built as described in detail in Section 6.1.1 produces exactly the same exponential scaling of life-times as the full system. We have used the threshold value of $A_0^2/2$ for the transition between the two integrators. This value of the threshold appears to be the optimum for a good agreement between the Hybrid Integrator and the original DNLSE. This does not mean that one could not build a hybrid integration scheme with different transitions, but one would have to build a different algorithm (like the ones described in the final notes of Section 6.1.1).

The data in Figure 6.1 might be hard to visualise, due to the large fluctuations on top of the breather norm. These fluctuations are of order $\mathcal{O}(\varepsilon)$, as we have seen from the first non-trivial terms in the MTSA. One way to eliminate them is to shift to the quantity Q, which has been defined at (4.73), or to perform averaging over times of ≈ 500 units (the time-scale of the thermalisation of the background). For reasons which have been described in detail in **Note 2** of Chapter 5.3, averaging over 500 time units is preferred. The same data can therefore be filtered as presented in Figure 6.2. The new figure allows a clean visualisation for seven separate trajectories for both algorithms. We now see that both algorithms produce relatively laminar dynamics, with very few oscillations, until the spontaneous emergence of an extreme event, where a sudden change in height occurs.

What is absolutely remarkable is the excellent agreement between the hybrid integration scheme (b) and the DNLSE (a). Breathers decouple from their surroundings for

very long times as their mass is increased for both integrators. Even more remarkably, the life times have very similar orders of magnitude. This proves that the derivation of the Effective Hamiltonian and the identification of the domains where this Hamiltonian breaks down were done successfully. A poor approximation for the averaged equation or an erroneous identification of the break-down domains would have made this agreement impossible. However, before assuming that the new algorithm is fully efficient, one must look at more detailed statistics.

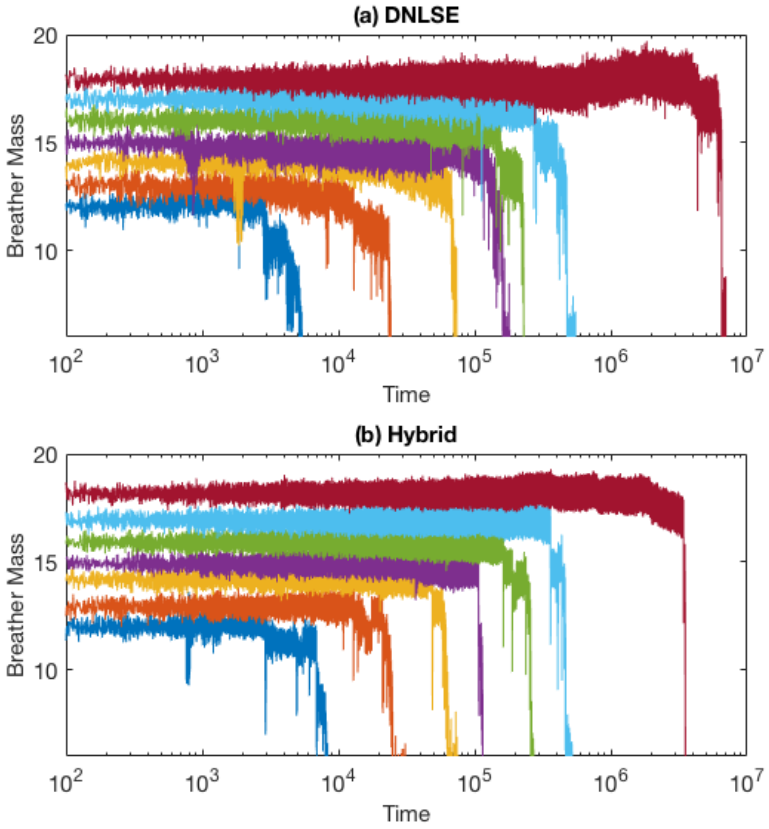

Figure 6.1: The time evolution of seven different breathers according to the DNLSE (a) and according to the Hybrid Integration Scheme (b). For both algorithms, one can observe an exponential increase of the breather life-time as the initial mass goes up.

In order to perform a more detailed analysis, we will initialise a breather at the middle of a lattice with $N = 15$ sites. The initial amplitude will have any of the

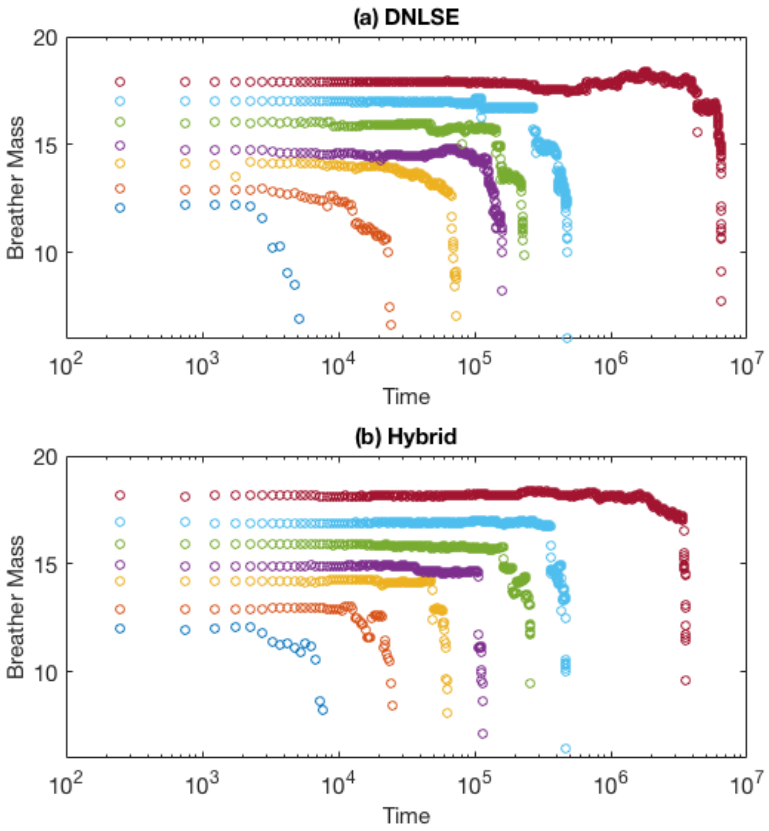

Figure 6.2: The filtered data for Figure 6.1. This allows a clearer comparison between the DNLSE (a) and the Hybrid Integration Scheme (b).

six values in the set $|z_0(0)| \in \{3.5, 3.6, 3.7, 3.8, 3.9, 4.0\}$. Once again, the heat baths will be in a symmetrical configurations and will have $T = 10$ and $\mu = -6.4$. During months of computations, it was possible to gather data for 123 collapses using the DNLSE, and 122 collapses using the hybrid integration scheme. As one would expect, the hybrid integrator was faster, and reaching a collapse requires shorter running times. The dependence of the decay times on the initial mass of the breather is presented in Figure 6.3. The initial mass of the breather here was not $|z_0(0)|$ but $\langle|z_0(0)|\rangle$, where the average was performed over 400 units. This was done in an attempt to filter out the large fluctuations on top of the breather, which starts at a random phase when the code starts to run. In a way, the values plotted there are the effective initial mass, without any component that comes from the large fluctuations (of order $\mathcal{O}(\varepsilon)$).

What is remarkable to notice in Figure 6.3 is that the data generated by the Hybrid Integrator is more spread (there is a larger standard deviation). This is due to the fact that the DNLSE produces diffusions which scale exponentially with the breather height, while the hybrid integrator is characterised by larger, power-law diffusions. This, however, does not seem to affect the average life-time when looking at multiple realisations (this will be further clarified in the next paragraphs). What the larger diffusion does is to grow the size of the breather fluctuations (drift slowly from the initial size) and

- if the breather goes up, it will take exponentially longer to find a resonance of size $A_0^2/2$ in the background;
- if the breather goes down, it will take exponentially shorter to find a resonance of size $A_0^2/2$ in the background.

We note, however, that the average height of the breather is unchanged and therefore these events will not affect the average life-time, but only the standard deviations associated with it.

Since it is impossible to initialise a breather at a certain height without having a

random displacement from the value around which the breather norm fluctuates, it is better to organise the data from Figure 6.3 differently. We now cluster all trajectories which started from the same initial condition and perform averages over 20 realisations for each initial condition. The average life-times are summarised in the data in Figure 6.4. It is now clear that exponential growth of the life-times with the initial breather mass is exceptionally clean in both cases, since both regression lines are very accurate. In addition to this, the actual equations of the two regression lines are almost identical. At this stage, one can safely state that the Hybrid Integration scheme developed in this thesis is a fast algorithm which approximates very well the evolution of the full Discrete Nonlinear Schrödinger Equation.

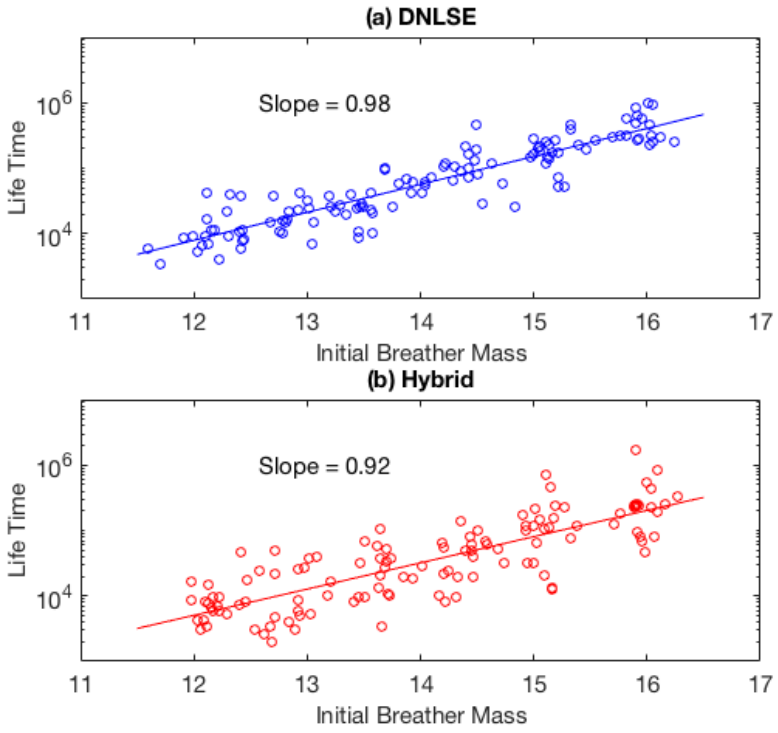

Figure 6.3: The life times of breathers according to the DNLSE (blue) and to the newly developed Hybrid Integration Scheme (red).

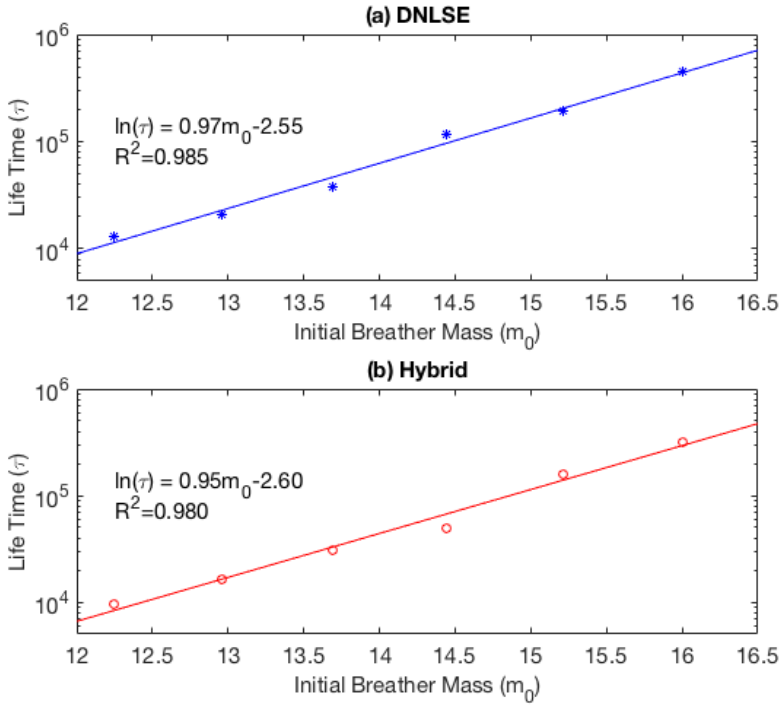

Figure 6.4: The life times of breathers according to the DNLSE (blue) and to the newly developed Hybrid Integration Scheme (red).

6.1.3 Conclusions

The work here explains how to average the DNLSE in a hybrid polar-Cartesian system of coordinates. The averaging procedure is developed for a lattice of a generic length with only one breather present at site $j = 0$. This can afterwards be extended to single breathers in contact with backgrounds on both sides, by adding two symmetrical contributions of the shape (5.27). The averaging techniques are developed under the assumption that the breather changes amplitude very little under one rotation, in agreement with the results from the Multiple Time Scale Analysis (Chapter 4).

The averaged equations are then used to build an Effective Hamiltonian, which is not unique. The Effective Hamiltonian can have arbitrary many terms, depending on the choice of the truncation. It is important to make sure that the newly chosen Effective Hamiltonian also conserves norm in the case of micro-canonical simulations. Ultimately, the Hamiltonian has to be picked in such a way to ensure a small artificial diffusion of the breather norm, while still simplifying the numerics in a significant way.

Once the Hamiltonian had been built, one can see how this 'effective Hamiltonian' relates to the Bose-Hubbard Hamiltonian, from which it originates. The Hamiltonian built here (5.27) separates by an order of $\mathcal{O}(\varepsilon^{3/2})$ over one full oscillation of the breather. The diffusion induced by the Hamiltonian on the breather norm decays as a power law with an exponent approximately equal to -6, while the original diffusion of the Bose-Hubbard model was scaling in an exponential way (this was shown by Figure 5.3). The diffusion process here is set to characterise the random walk in the breather height, and does not imply any sort of drift or decay of the soliton. In other words, it shows how much the soliton fluctuates in size, without giving any information on its life-time. We have shown here that the diffusion does not affect the average life-time of the breather, but only the standard deviations associated with this quantity.

In order to build a Heterogeneous Multiscale Method (a Hybrid Integrator) one must identify the domains within which the macro-integrator cannot be employed. These are

given by the resonances presented in Figure 5.4. From this, it follows that one cannot use the averaged equation whenever the background creates an excitation larger than $|z_0|/\sqrt{2}$ in the proximity of the breather. These are topological aberrations which were essential for defining transitions between the AvNLSE and the DNLSE when building the Hybrid Integration Scheme.

It has therefore been possible to build a Heterogeneous Multiscale Integration Algorithm for the DNLSE which performs remarkably well, as one can see in Figure 6.2 and 6.4, and which can take down the running times by a factor of at least ≈ 5. Defining the transitions between the two integrators in a more liberal way would allow even faster integrations, but when changing the Hybrid Integrator one must still make sure that the overall statistics are obeyed, and that no extreme events are artificially missed.

6.2 Multi-Breather Systems

6.2.1 Writing a Heterogeneous Multiscale Method Algorithm for Lattices with Multiple Breathers

The construction of the Hybrid Integration scheme was presented in detail in Chapter 6.1.1. We will now focus on the architecture of a similar algorithm which can work for an arbitrary large number of breathers, or even no breathers at all. The algorithm is presented in the flow chart from Figure 6.5. There are some differences from the previous Hybrid Integrator, which will be explored more thoroughly in the next schematic description of the expanded integrator.

1. The algorithm starts by identifying all locations with breathers (i.e. sites with $|z_j| \geq 3.5$). It then creates an array with all these locations and transitions towards a state vector which will have polar coordinates for the breathers (at the locations described in the array) and Cartesian coordinates everywhere else (for the background sites).

- If there are no breathers in the lattice, one will simply leave the breather coordinates array blank, and whenever this happens, the full DNLSE is employed.
- If any of the breathers is too close to the heat baths (at most three sites away from them), we once again leave the locations array blank to force the use of the DNLSE. We know from the averaged differential equations at (5.28)-(5.35) that the three nearest neighbours will have additional terms from the classical DNLSE derivatives. We therefore impose the condition that we have at least three sites in the background so we can employ the effective Hamiltonian that was developed.

2. At this stage, one must test that all breathers are at least three sites away from each other. We have shown previously that interactions for excitations more than three sites away are effectively negligible for the Bose-Hubbard model. As a lucky coincidence, the number of sites in the background which are coupled to the breather in the averaged equation is also three. Therefore a buffer zone of three sites was a natural choice.

   - If any two breathers sit too close to each other, we simply leave the breather locations array empty and pursue with the DNLSE integrator
   - If the distances between all consecutive breathers are at least equal to three sites, we start building the effective Hamiltonian, by using the DNLSE for all the isolated puddles between breathers (the breather sites are treated as reflective boundaries), and adding on top of that the terms (the non-DNLSE terms) in the averaged equations from (5.28)-(5.35). If there is a breather to the left and a breather to the right of a puddle of three sites there will be three terms from the left breather and three terms from the right breather (first neighbour for B1 and third neighbour for B2, second neighbour for both B1 and B2, third neighbour for B1 and first neighbour for B2).

3. Here we also test that all three nearest neighbours have masses which are smaller than the $A_k^2/2$ (k corresponds to the k^{th} breather in the lattice). The moment we find at least one exception to this rule, we make the breather location array blank and we force the algorithm to use the DNLSE, since we do not want to artificially miss a rare event.

4. The time step is determined by the largest excitation in the background (inversely proportional to its mass). Making the time step time-dependent on the size of spontaneous excitations is crucial, especially since for the Hybrid Hamiltonian the time step is given by the background, and not the breather, therefore using a time step that is kept too large when spontaneous excitations emerge can be highly problematic when trying to conserve Hamiltonian (the effective Hamiltonian in this case). We therefore identify the largest excitation that is not a breather (we exclude all sites in the breather locations array) and from that we adapt our time step.

    - If the breather locations array is left empty, the largest excitation would simply be given by the largest amplitude in the lattice. For example, if the breather was too close to the edge, and the location array was left empty, the time step would simply be inversely proportional to the breather height.
    - If the breather array is not empty, we will make use of an Effective Hamiltonian with arbitrary many breathers, and the time step will only be given by the tallest excitation in-between these breathers.

5. At this stage of the algorithm, the breather coordinates are clearly defined, and so is the effective Hamiltonian (with multiple breathers at random sites). In addition to this the time step is also calculated. The algorithm will proceed on one of three paths:

    - If the array was left empty because no breathers were found, the algorithm

will effectively be equivalent to the DNLSE with a large time step

- If the array was left empty because the breathers were in the vicinity of a large excitation or too close to each other (the second case is a subset of the first one), we will use the DNLSE with a small time step. Up to here, both these scenarios are already included in a simple use of an adaptive step DNLSE. Here we keep integrating using the DNLSE until all the neighbours of the breathers decay under the value of 1, to make sure that the extreme event was allowed to develop fully.
- If the array is not empty, it means we can safely use the Effective Hamiltonian with Multiple Breathers. We now use a large time step, which is given by the backgrounds and not the breathers themselves. This scenario is the most likely one by far, and due to this the Hybrid Integrator performs faster then the DNLSE.

6. After integrating for one time-step, we repeat procedure 1.

Note: All the data in Chapter 6 was generated using the algorithm above, which encompasses the case of systems with one breather. At the beginning the algorithm was developed for one breather only, but it was ultimately extended to what is described above and in the flow chart from Figure 6.5

6.2.2 An example of a Strong Interaction with a Large Excitation

When a breather interacts with a strong excitation, it basically interacts with a smaller breather, which can either be pinned to a lattice site, or can be mobile and move towards the breather from the background. It was already shown that extreme events can only be encompassed by the DNLSE, since any averaging would artificially enhance breather stability.

The interactions with the nearest neighbour have been thoroughly covered throughout this work, be they resonances or the spontaneous emergence of bound states. It

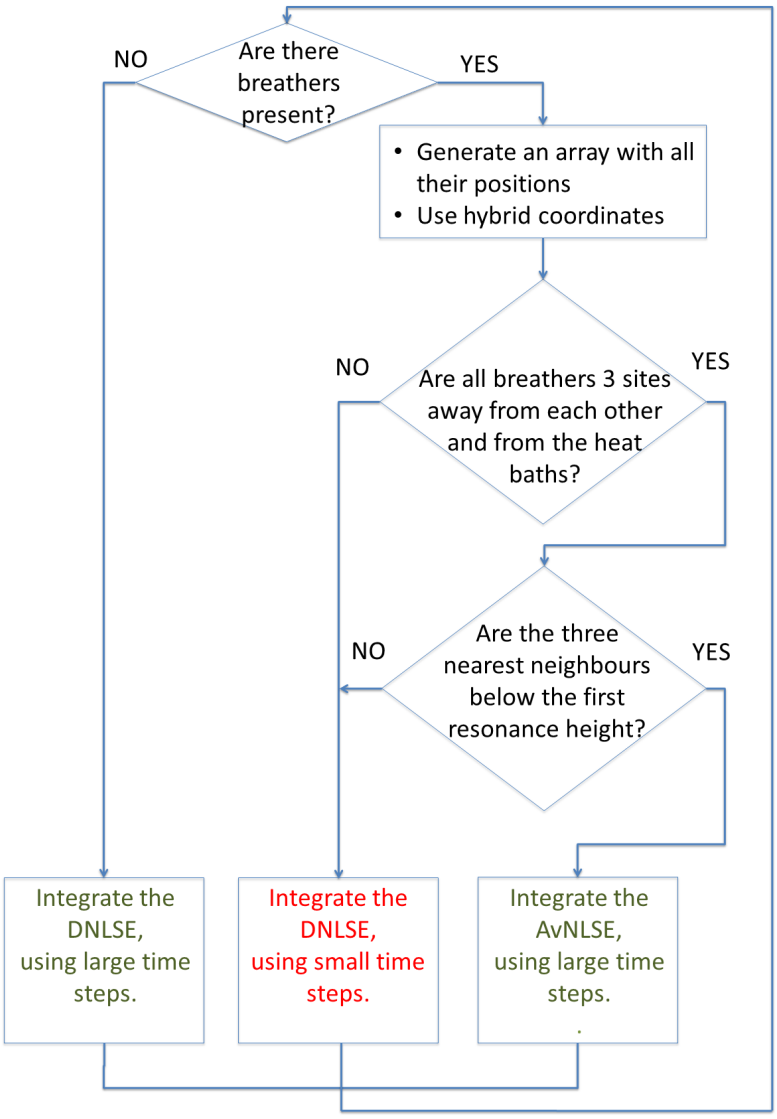

Figure 6.5: The life times of breathers according to the DNLSE (blue) and to the newly developed Hybrid Integration Scheme (red).

was also presented that we can get resonances between breathers which are two sites away (i.e. there is a buffer area of one single site between them).

It is interesting to observe the spontaneous emergence of a strong interaction with a breather which was three sites away from another. This was the maximum size of the buffer zone we defined when building the Hybrid Integrators. In the diagram from Figure 6.6 we see that the breather from site $j = 4$ gets destabilised suddenly and triggers a strong interaction with the large breather at site $j = 1$. In the Hybrid Integrator, the algorithm would see that this site has exceeded the critical value of $A_1^2/2$ and would shift to the DNLSE, allowing this kind of strong interaction to happen.

It is also interesting to see how the amplitude of the large breather at site $j = 1$ changes with time. This is done in Figure 6.7. We have filtered out the fast harmonics using the low pass filters defined at the beginning of this work in Chapter 2.3.1. Averaging over 500 units would be highly ineffective during an extreme event, since the whole duration of the event was ≈ 1000 units, and we would only have two data points. The low pass filters, even if they are computationally expensive due to the large number of Fourier transforms required for their implementation, offer a much clearer picture of the interaction.

What we see in the filtered data from Figure 6.7 is that the breather mass is highly stable, and suddenly interacts strongly with the nearest neighbour. After the extreme event is over, the breather mass becomes stable once again, but this time it will stabilise around a different value (in this event higher than what we initially started with, but it could as well have decayed). The dynamics is split between laminar regimes (like before and after the extreme event) and extreme events. During laminar flows, the slow drifts are contained by the envelope given by the MTSA in Chapter 4. This means that inequality (4.60)

$$-2\pi\frac{13}{2}\varepsilon^3\Pi_f(A_1) \leq \Pi_f(A_0) \leq 2\pi\frac{13}{2}\varepsilon^3\Pi_f(A_1) \tag{6.1}$$

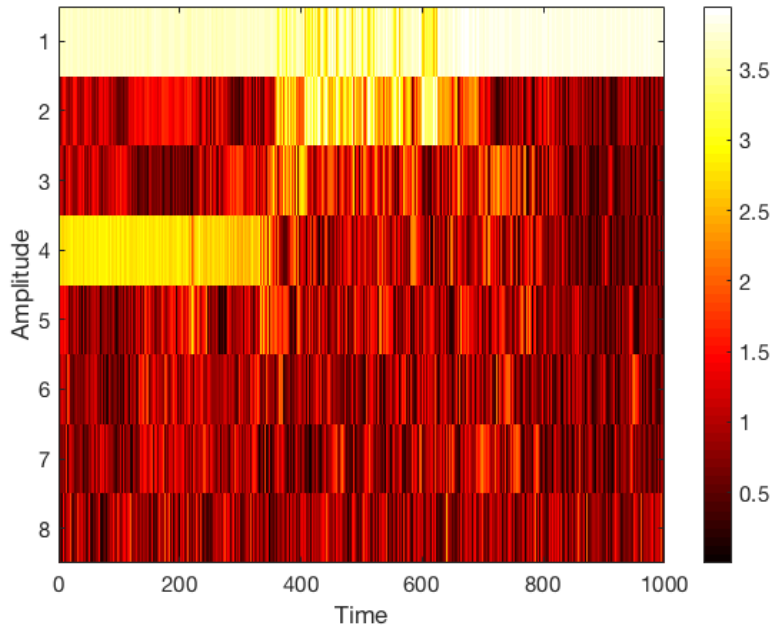

Figure 6.6: The collision between two breathers which were initially three sites apart.

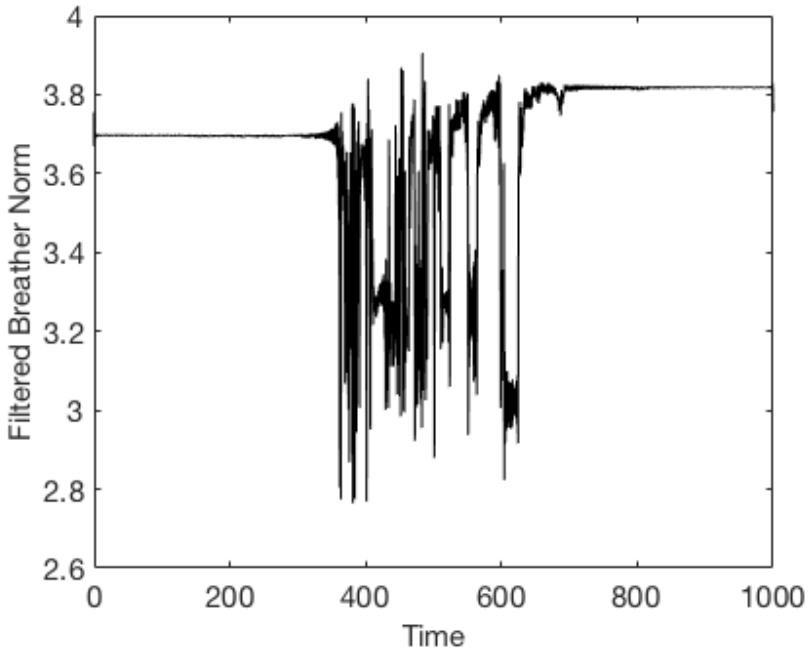

Figure 6.7: The low pass filtered breather mass during a strong interaction with an excitation in the background.

is satisfied.

During the extreme event, we are in the regime of the turbulent flow, and the inequality above is violated.

The event which was recorded in Figures 6.6 and 6.7 is peculiar also because it showed regions when the phases of the sites between the breathers were monotonously decreasing. This is highly unusual for a non-linear system like the DNLSE, where we expect the whole lattice to oscillate with a positive frequency (on average). This shows that the interactions between the breathers actually involve the sites between them as well, and when the breathers get close enough the analogy 'Breather' - 'Background' - 'Breather' to 'Reflective Boundary' - 'Background' - 'Reflective Boundary' breaks down, therefore the very first assumptions used to develop an Effective Hamiltonian lose validity.

Even if this event is very interesting due to its peculiar nature, it is important to mention that it is very rare. The statistics for the interaction with the third neighbour of a breather are recorded in Figure 3.6, where it was shown that, on average all interactions between the breather and its third neighbour are basically negligible. For most of the neighbour values, the changes of energy were minute staying at $\mathcal{O}(10^{-2})$. Even when the neighbour was getting to the same height as the breather, the interaction energy was barely reaching $\mathcal{O}(1)$, while for the first neighbour one could get interaction energies up to four orders of magnitude larger. When the tests were done for the fourth neighbour, the interactions were basically non-existent. We now have a full justification for the choice of the size of the buffer zone at three sites for each side of the breather. We can now also see the type of event which might be missed if the buffer zone would have been reduced to two sites only (the only sites which do interact with the breather due to a resonance).

6.2.3 The Applicability Domain of the Multi-Breather Algorithm

Just as in the case of the original Heterogeneous Multiscale Algorithm from 6.1.1, the system consists of two characteristic Hamiltonians

1. The Bose - Hubbard Hamiltonian - the main focus of this work
2. The Effective Hamiltonian - no longer the 'simple' equation from (5.27), since there is (usually) more than one breather present in the system. The effective Hamiltonian will change at every time step depending on
    - How the number of the breathers in the system evolves with time
    - How the location of the breathers changes in time

Note: A change in the number of breathers or in their locations can only occur during the DNLSE integration, which is triggered once any of the close neighbours exceeds the first resonance threshold.

Even if the effective Hamiltonian and the Bose-Hubbard Hamiltonian work perfectly in micro-canonical configurations, the hybrid was not designed for micro-canonical systems but for lattices in contact with heat baths, which over astronomical life-times would thermalise to the heat bath parameters. More details on these thermalisations will be given in the next section. After going through a transition of the sort AvNLSE - DNLSE - AvNLSE we do not return to the same hyper-surface of the effective Hamiltonian. What is important to mention though is that

1. The norm is exactly the same for the two Hamiltonians - therefore after no matter how many transitions from one integrator to the other occur, mass is never artificially created or annihilated
2. The drifts which occur in consecutive passes from one AvNLSE hyper-surface to the another are much smaller than the characteristic changes introduced by the stochastic heat baths. Since the heat baths introduce fluctuations of the order

$\mathcal{O}(\sqrt{\Delta t})$, and the time step is very large for the averaged equations (since this is the whole point of building a macro-integrator).

Therefore this algorithm becomes ideal to study thermalisations, since the large backgrounds are replaced by Langevin heat baths and the need to use a small time step due to the presence of the breather is eliminated. We can now work with low-dimensional systems that can be integrated with a large time step, which is an ideal set-up for any numerical investigation.

The current algorithm is not only powerful in reproducing the decays of single breathers immersed in large backgrounds, but also in sketching multi-breather interactions and describing thermalisation phenomena, as demonstrated in the next sections.

6.2.4 Results: Hybrid Integrator for Multi Breather Lattices

Let us now do a similar test to what was already shown in Section 6.1.2, but for a lattice with two breathers, with a total length of $N = 20$ sites. The breathers are initially set six sides apart from each other, so that the Hybrid Integrator can be successfully used. The breathers were set at initial heights of $|z| = 3.90$ and $|z| = 4.04$, since we know that the Effective Hamiltonian is highly reliable for these values from the calibration curves in Figure 6.4. What is now new compared to the previous system is that the two breathers will have different frequencies, and therefore there will be two separate smallness parameters.

These relatively small values of the breather heights have also been chosen so that a decay is very likely. Large breathers still decay in astronomically long time-scales and the simulations can still take weeks (as opposed to months for the DNLSE) when the Hybrid Integration Scheme is used. Just as before, the ends of the lattice have been set at $T = 10$ and $\mu = -6.4$. Without using heat baths, we would never see the decay of a breather in such a short lattice, because the enormous energy stored in the breather would have nowhere to dissipate. In addition to this, the Hybrid Integrator was only designed for systems with heat baths, therefore this configuration is almost compulsory

when extended to the Hybrid Integration Scheme.

When the two breathers are set to evolve according to the DNLSE, we see several migrations of the breathers and decays over lifetimes of the order $\mathcal{O}(10^6)$. The exact trajectories are depicted in Figure 6.8. After a very long waiting time, the two breathers are completely absorbed by the background, and the system becomes fully thermalised. Before this happens, the breathers break the lattice into three distinct regions, which are locally thermalised. This is due to ergodicity breaking. When the pinned breathers are suddenly destabilised due to the spontaneous emergence of a rare event, they might abruptly move to a neighbouring lattice site. During the rare event, the left and right sections on either side of the breather are allowed to interact, and atoms can travel freely from one side of the destabilised breather to the other. As the soliton re-stabilises, the sections on the left and the right will reach thermal states which will be different from those present before the rare event (T_{left}, μ_{left}, T_{right}, μ_{right} will all change). This type of transition from a laminar flow to turbulent dynamics and back to laminar evolution will be examined more thoroughly in Section 6.3.

The system is then allowed to evolve from the same exact initial condition, but this time according to the Hybrid Integration scheme. The result is presented by Figure 6.9. Remarkably enough, the two breathers will also get absorbed by the background in a timespan of $\mathcal{O}(10^6)$, just as it was initially shown by the full DNLSE. Not only that, but the spontaneous tunnelling of breathers is also observed. Naturally, after both breathers disappeared, the Hybrid Integrator is equivalent to the DNLSE and the background will be thermalised at $T = 10$ and $\mu = -6.4$.

Even if the two trajectories are not identical, the power of the Hybrid Integration Scheme is still impressive. The main reason why the trajectories separate is chaos. Simply the fact that the AvNLSE uses a larger time step than the DNLSE, and that the stochastic noise from the baths will be different (since the sampling is more dense for the DNLSE) is enough to separate the two trajectories quite early. This separation will happen even if one uses the same seeds for the noise. Nevertheless, the thermodynamic

properties given by the two algorithms are equivalent.

There is therefore more room for investigation when it comes to systems with more than one breather. This scheme would also be efficient for studying coarsening, since it would only activate the DNLSE when a trigger is detected and it would not spend astronomically long times to integrate the laminar regime where breathers sit at a fixed distance from each other, with very little interaction.

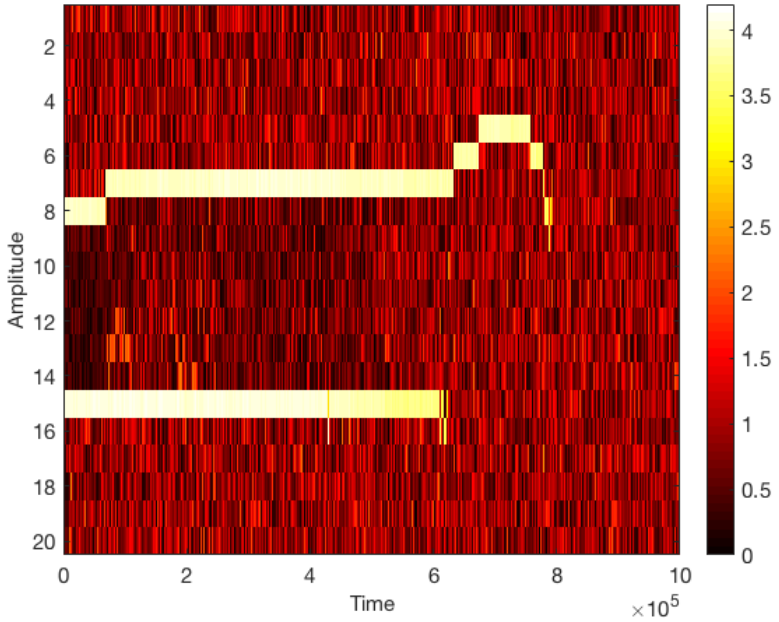

Figure 6.8: The evolution of two breathers in lattice with 20 sites put in contact with positive temperature heat baths. The system is allowed to evolve according to the dynamics given by the Bose-Hubbard Hamiltonian.

6.3 Thermodynamics and the DNLSE. Uses of the Hybrid Integration Scheme

6.3.1 Thermalisation of the background

The thermalisation times for a one-dimensional Bose-Hubbard chain of length ~ 100 are of the order $\mathcal{O}(10^3)$, as one could see from the numerical investigations presented

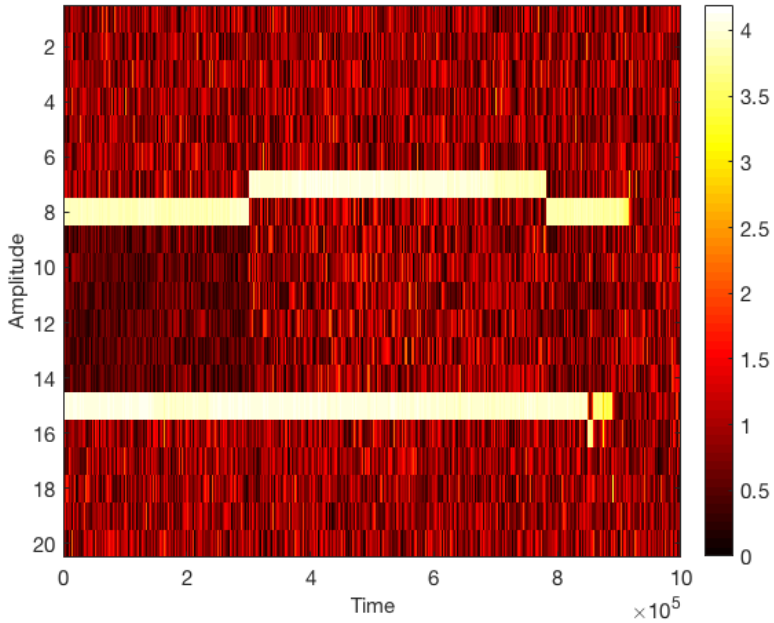

Figure 6.9: The evolution of two breathers in lattice with 20 sites put in contact with positive temperature heat baths. This time, the system is integrated using the Hybrid Integrator.

in the early stages of this work in Figures **??** and **??**. When the condensate thermalises with the Langevin heat baths, its temperature and its chemical potential fluctuate around the values of the thermal parameters given by the thermostats (this should always happen if the system is calibrated properly and if the numerical temperature and chemical potential are defined correctly). For lattices of size ~ 10, which are the usual lengths employed for single breather systems, the thermalisations times go down to $\mathcal{O}(10^2)$, making the background reach an equilibrium state almost instantaneously when compared with the time-spans of the breather lifetimes ($\mathcal{O}(10^7)$ and beyond).

When the background thermalises, all sites which are part of it will follow similar statistics, for their amplitudes and phases. This was shown during the numerical tests employed when the MTSA was developed, back in Chapter 4. This stabilisation suffices to establish that the thermalisation is complete. The explicit calculation of the numerical temperature and of the numerical chemical potential is very expensive com-

putationally, and it is only very useful at the starting stages of code development, when one must test that the heat baths are properly calibrated, both for infinite temperature configurations, but also for finite temperature states. This is to make sure that the Langevin heat baths defined in Chapter 2.1.2 generate the types of backgrounds we want.

Another equilibrium condition is that the flux of energy and mass through a certain site is zero. As a matter of fact, this constituted the solvability condition for closing the MTSA. This type of equilibrium condition works in the following conditions:

1. When both ends of the chain are at the same temperature and chemical potential.
2. When the chain is in a micro-canonical set-up (including the case when the chain is in a Periodic Boundary Condition (PBC) set-up).
3. When one of the ends of the chain is in contact with a Langevin heat bath and the other is in contact with a reflective boundary. This scenario, by analogy, is equivalent to the case when a breather sits at one end and a heat bath is generated at the other.

The flux equilibrium condition DOES NOT work when

- The two ends of the lattice are in contact with heat baths at different temperatures and chemical potentials.

In this case, a Non Equilibrium Stationary State (NESS) is created, where each site will have its own histogram for amplitude and phase, and only the ends of the chain will thermalise with the bath they are in contact with. This kind of set-up is more thoroughly studied in [51]. What is interesting though, is that because of the ergodicity breaking induced by breathers in a one-dimensional lattice, a system with one breather can be replaced by two analogous systems of the type 4 (from the list above). We have used this property extensively when adding symmetric contributions for the averaged differential equation. This means that a pinned breather in a lattice which is put into

contact with heat baths at different temperatures will act as a thermal insulator, and the left and right hand sides will thermalise independently, while still obeying flux conservation laws, unlike in a NESS regime.

But before making this statement, let us look at the thermalisation properties of backgrounds in the presence of breathers. Since breathers are very stable (life times of the order $\sim 10^6$ time units), they are effectively infinitely long-lived when compared to the thermalisation times. Figure 6.10 shows how the buffer background consisting of seven sites thermalises when put into contact with a Langevin heat bath at positive temperature. We can observe that all sites have equivalent statistics, with the exception of site $j = 1$ which is in direct contact with the breather and site $j = 7$ which is in direct contact with the bath. Remarkably enough the two sites obey similar dynamics to the ends of the chain. The error bars were set to depict the standard deviation for each amplitude. Sub-plot (a) shows the evolution as it is given by the DNLSE, and the findings are in perfect agreement with:

1. the numerical findings from Figure 2.5, which showed that all background sites obey equivalent statistics. However, while that diagram was for infinite temperature backgrounds, this one covers positive temperatures. The fundamental message is the same, the breather acts as a reflective boundary for the two adjacent backgrounds (on its left and on its right);

2. the first neighbour of the breather obeys different statistics, since it has a different type of asymptotic expansion, as it was shown in the early stages of the MTSA algorithm, in Eq. 4.7.

Figure 6.10 shows the amplitude statics for the evolution of the same background (same initial condition), according to the DNLSE (b), and according to the Hybrid Integration scheme developed in this chapter (a). We can see that the new plot is basically indistinguishable from that obtained using the DNLSE. This means that, even if the Hybrid Integrator will lead to a different trajectory, the overall statistics of

the background will be the same. This means that the extreme events will have the same frequency as in the case of the full system, since they are generated by peaks over a certain threshold, and the histograms are identical. The main reason for the separation in trajectories between the Hybrid and the DNLSE is the use of a larger time step, which creates a different stochastic noise. The different noise, in conjuncture with the chaotic nature of the system, creates a very fast separation between trajectories. These histograms offer a more detailed explanation why we see the same statistics for the life-times, even if the background trajectories separate very early during the simulations.

6.3.2 Thermalisation of the whole system - Breather decay

All the statistics presented in this chapter were gathered for $T = 10$ and $\mu = -6.4$ (micro-canonical definitions). It would be very interesting to see what happens when these parameters are varied. Before doing so, it is important to mention that $T = 10$ and $\mu = -6.4$ is a pair of parameters which was chosen because it generated backgrounds with an average occupancy number of $\langle |z_j| \rangle = 1$. Varying T and μ randomly would be very problematic, since there would be two parameters which are changed for each realisation, and it would be close to impossible to find the physical interpretation of any change in breather behaviour.

It is always more elegant to work with a problem when only one parameter is varied, the only issue was to identify what this parameter should be. The way to tackle the problem was to find pairs of $\{T, \mu\}$ which generate backgrounds of order 1. The pair $\{T = 10, \mu = -6.4\}$ has been kept, since the Hybrid Integration scheme was calibrated for these values and it would offer a good reference for any other values one would decide to use later.

We now multiply $T = 10$ with seven different powers of 2 to obtain the temperature samples $T \in \{2.5, 5, 10, 20, 40, 80, 160\}$. When the temperature is very low, the background amplitudes will obey similar statistics to a Kronecker delta centred around

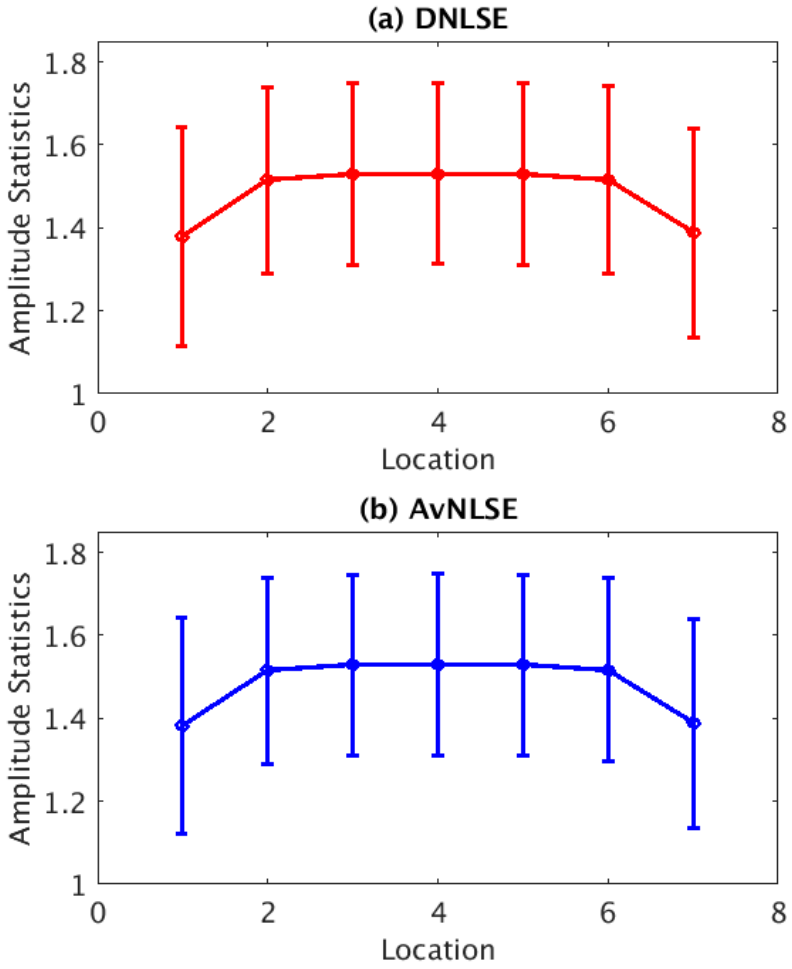

Figure 6.10: The statistics of the buffer background (Sites between the breather and the breather at $j = 0$ and the Langevin heat bath at $j = 8$), as given by the DNLSE (a) and by the Hybrid Integration Scheme (b). The averages are performed over 5000 time units. The very small lattice usually thermalises over 10 units, therefore the averaging time is roughly 500 larger than the time it takes for the buffer to get into equilibrium with the heat bath.

a mean value defined by μ. As the temperature is increased, the background starts to obey Poissonian statistics [34]. If one decides to use infinite temperature Langevin heat baths, the behaviour is very similar to most positive temperature heat baths with $T > 50$. Now that we know which values of T we will be sampling, it is important to choose the values of the chemical potential as well.

The strategy which was used here is to vary μ for each value of T until one would find a pair that generates backgrounds with averages as close to 1 as possible. This would ensure that all seven histograms would have the same average, but different shapes. Therefore, even if the average size of the background is the same, the overall chance of an extreme event occurring would vary with the histogram shape [34]. The search process was similar to Newton's method of looking for zeros. For each value of T:

1. Start at a guess value of μ (always negative) and calculate the average amplitude of the background.

2. If the average value is larger than 1, have μ, otherwise double it. Then re-evaluate the average amplitude of the background.

3. Depending on where the new value lies, build segments of $\langle|z|\rangle_{min}$ and $\langle|z|\rangle_{max}$ and memorise the values of μ associated with them.

4. Always use for the guess value the average value of μ for the segment defined at 3.

5. Repeat until the average is accurate within an accuracy which is specified by the user. Here 10^{-2} was deemed more than sufficient.

The pairs $\{T, \mu\}$ which generate backgrounds of size $\langle|z|\rangle \approx 1$ have been identified to be

T	μ
2.5	-0.82
5	-2.3
10	-6.4
20	-16.3
40	-35.9
80	-72.8
160	-145.6

The next step was to run simulations for all these values of the thermal parameters, for at least five realisations. At the middle of the lattice there was always a breather of size $|z_0(0)| = 3.85$, which was allowed to evolve until complete decay. The results of the integrations are summarised by Figure 6.11. We can see that for small values of the temperature, the breather is extremely long-lived, up to 10^5 more stable than when the temperature is increased to $T = 40$ degrees. This happens because of the fact that when the background has a low temperature, it behaves very linearly, and the amplitude histogram is close to a Kronecker delta. Therefore high excitations which can destabilise the breather are astronomically unlikely. We were able to record seven decays using the Hybrid Integration Scheme (each over a running time of 10^7). Needless to say, most of the running time was spent on integrating the low temperature system, where the life-times of the breather are $\sim 10^5$ larger than everywhere else. The Hybrid Integrator proved to be a very potent tool in this case.

6.3.3 Hybrid Integration for Different Background Temperatures

We have seen that when the temperature is very small, breathers are extremely long-lived. This is because the amplitudes in the background obey a histogram which looks like a Kronecker delta centred around $|z| = 1$. For a breather of size $|z(0)| = 3.85$, any of the three nearest neighbours (either on the left or on the right) must exceed the

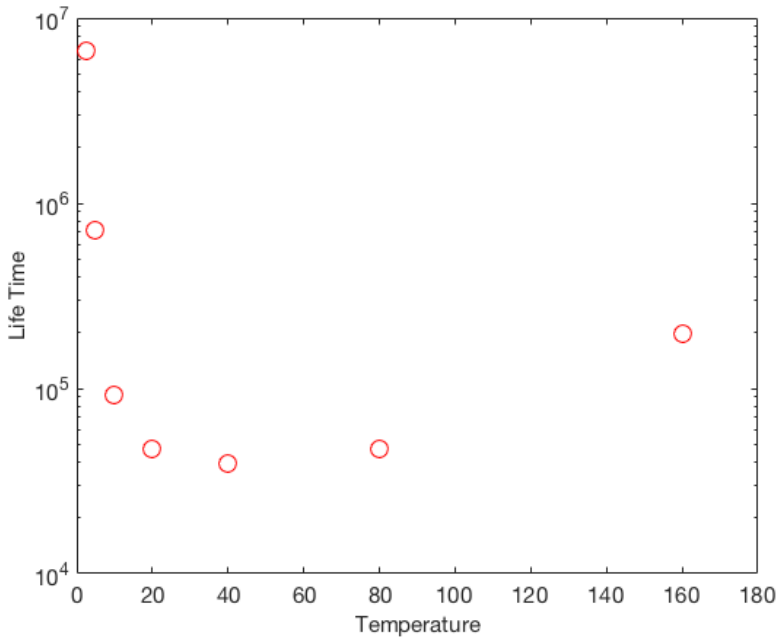

Figure 6.11: The life-time of a breather of initial height $|z(0)| = 3.85$ for different temperatures and chemical potentials which give rise to backgrounds of size 1. Low temperature backgrounds take very long to absorb the breather, while high temperature backgrounds do not differ much in the dynamics they produce.

threshold value $|z_{neighbour}| = \frac{3.85}{\sqrt{2}} \approx 2.7$, to trigger a shift to the DNLSE, and ultimately a potential decay. As we can see in Figure 6.11, the average running time for a decay to happen in this case is of order $\mathcal{O}(10^7)$. This happens for a very small breather, of mass $3.85^2 \approx 14.8$. One can imagine that for breathers of size 36, like those studied in the resonance experiment in Figure 3.6, the lifetimes would be astronomical. The advantage of the low temperature regime is that the algorithm almost never enters the DNLSE regime, because the first resonance threshold is very rarely reached, therefore for most of the time the AvNLSE is used to project the state.

A general trend is observed as - rather intuitively - backgrounds of higher temperatures spend more time in the DNLSE regime, since they are more likely to produce an excitation that is larger than the transition threshold $A_0^2/2$. This means that as the temperature is increased, the gain obtained from using the Hybrid Integrator is reduced. The system will spend a long time integrating the equation using the DNLSE, until all the neighbours (six neighbours in total) have decayed under the value of 1, and the breather has rotated for an integer amount of times. It usually takes a long amount of time for all these seven conditions to be satisfied simultaneously (order of $\mathcal{O}(10^3)$).

Even if the computational advantage of the Hybrid Integrator diminishes for large temperatures, the life-times go down as well, as one can easily deduce from Figure 6.11. This implies that the largest gains occur exactly during the simulations that are exceedingly slow, which is the ideal scenario. Once again, the Hybrid Integrator seems to pass a sturdiness test, since its applicability is more suited exactly in those regimes where the simulations would be too slow if the pure DNLSE would be used.

Now we must also take into account the shape of the stochastic noise generated by the Langevin heat baths. As we have seen in Chapter 2.1.2, the positive temperature heat bath will contain terms of the sort $i\gamma\mu z_n + \sqrt{\gamma T}\xi_n(t)$. This means that as we increase μ and T we generate larger and larger fluctuations at the end of the chain. Given the fact that the time step (δt) is inversely proportional to the highest excita-

tion in the background, we can see why the simulation slows down significantly as we increase T and μ. After a while, the white Gaussian noise at the lattice end will have a variance that is so great, that it becomes basically not physical. A temperature of $T = 160$ is already pushing into this regime. We know this because, when evaluating the temperature for a system in contact with infinite temperature heat baths we get temperatures of T (calculated using the numerical method from Chapter 2.1.3) ranging between 50 and 5000. This is because the computer cannot evaluate a quantity which diverges, and it will give it a very large value. It is important to notice that, for the numerics, a temperature of $T = 50$ is indistinguishable from an infinite temperature.

This can be used to replace all heat baths with temperatures above ~ 50 with infinite temperature heat baths where the average occupancy number is set at $a = 1$, so that we make sure that the average value of the background amplitude is still 1. This will generate purely Poissonian histograms for the amplitudes (the limit case when $T \to \infty$ and $\mu \to \infty$). The advantage of employing infinite temperature heat baths is that now the white Gaussian noise has a small variance, and the system will be much better behaved, generating more stable numerics. In addition to this, the infinite temperature heat baths would also give a clear advantage of the Hybrid Integrator over the DNLSE, since the largest excitation in the background would be small enough to generate a large time step. The DNLSE would not perform faster, however, since the time step would (almost) always be given by the breather amplitude, which will exceed the white Gaussian noise at the end of the lattice.

It now becomes apparent that the Hybrid Integration scheme will drastically speed up simulations for situations when the background temperature is small. It can also be employed for infinite temperature backgrounds, to generate faster realisations for the breathers decay. This, however, can be covered in future projects. The same type of analysis could once again be extended to multiple breather lattices, and the evolution of coarsening could be simulated faster than what the DNLSE could allow. One could see how coarsening is either accelerated or inhibited by temperature and chemical potential.

An interesting finding presented in Figure 6.11 is that the breather life-time does not diverge as the temperature is increased. This means that the ergodicity breaking induced by breathers is always temporary, even if 'temporary' might mean for an astronomically long amount of time.

Chapter 7

Conclusions

This thesis has looked at the properties of the Discrete Nonlinear Schrödinger Equation and at the behaviour of its localised modes (breathers). Differently from what is already abundant in literature, most work was carried for breathers in the presence of very large perturbations, described by backgrounds which are thermalised at a certain temperature and chemical potential. This implies that the smallness parameter of the system is not given by an infinitesimal perturbation, but by the inverse of the breather frequency ($\varepsilon = 1/\omega$).

Breathers oscillate very rapidly, due to the non-linear component of the DNLSE. This allows them to adiabatically decouple from their surroundings and act as isolated oscillators for astronomically long times. During this evolution, the system is characterised by three time scales - that given by one full breather oscillation, that given by the slow evolution of the background, and the very slow time scale given by the breather lifetime.

The localisation of breathers is extremely strong, most of them occupying one single site in a one-dimensional lattice. The sites adjacent to the breather thermalise locally, forming a reservoir of phonons which cannot interact with the atoms on the other side of the breather. The spectra generated by these backgrounds is completely decoupled from the large frequency of the breather, which looks like a Kronecker delta peak,

clearly separated from the overall spectrum of the background.

The lifetimes of breathers are astronomically long, since their interactions with neighbouring sites are minimal. As the initial breather mass is increased, its life time goes up exponentially. This makes the numerical study of breathers very challenging. The time step must be scaled proportionally to the inverse of the breather mass. Additionally the life-time of a breather grows exponentially with its mass. Combined, these two dependencies make the numerical integration of large breathers highly challenging.

In an attempt to study what makes breathers connect with their surroundings, we performed numerical experiments which showed that even in extended lattices, bound states do form and, as a separatrix is crossed, the breather is allowed to move to an adjacent site or to suddenly change size.

In addition to this, it was possible to identify clear resonances between pinned breathers and the phonon backgrounds that surround them. These resonances induce sudden changes in the breather size. The laminar evolution is interrupted when the system reaches a resonant hyper-surface, as the breather norm stops being an adiabatic invariant, suffering an abrupt change in size. During these rare events, it is impossible to perform averaging, since they are non-perturbative.

The Multiple Time Scale Analysis (MTSA) has shown that during the laminar regime, the breather derivative is bounded by a term of the order $\mathcal{O}(\varepsilon^2)$. This suggests that the breather norm is indeed an adiabatic invariant, since over times of order ε, it cannot change more than $\mathcal{O}(\varepsilon)$. This is one of the fundamental definitions of an adiabatic invariant. The MTSA was concluded by using the equilibrium conditions that all fluxes in the background must cancel. This constituted the solvability conditions of the asymptotic expansion.

In the laminar regime, we were able to perform averaging, and to build an effective Hamiltonian which models the weak interaction between the breather and its surroundings. This effective Hamiltonian acts as a macro-integrator for the Bose-Hubbard chain, which together with the DNLSE can be used to build a Heterogeneous Multiscale

Method - a numerical algorithm which allows the fast integration of the DNLSE with an adaptive time step.

The Hybrid Integrator was able to produce similar dynamics to the DNLSE, leading to breather life-times which scale exponentially with their mass. This algorithm can be extended to multi-breather lattices and can also be used to study how the decays of breathers is influenced by the thermodynamics of the phonon bath.

The Hybrid Integration Scheme constructed in this thesis is remarkable for the fact that it is applicable to lattices of any length and to systems with multiple breathers (of different frequencies). The fact that the perturbations hold their validity in the presence of positive and infinite temperature Langevin heat baths extends the range of possible investigations greatly, offering the opportunity to study thermalisation phenomena for systems with weak ergodicity breaking.

Ultimately, such algorithms could be extended to other nonlinear chains, such as Fermi-Pasta-Ulam-Tsingou and Toda lattices, or even to other Discrete Nonlinear Schrödinger Equations (ring shaped BECs).

The behaviour of breathers when in contact with positive temperature heat baths shows that regions that were expected to be characterised by unstable localised solutions actually conserve breathers for very long times, in meta-stable states. These extended regions of stability offer a higher manoeuvrability for BECs in optical lattices and arrays of optical wave-guides, allowing controlled switching on and switched off of pinned breathers in these extended regions.

Bibliography

[1] W. Cropper. *Great Physicists: The life and times of leading physicists from Galileo to Hawking*. Oxford University Press, 2001.

[2] S.N. Bose. Plancks Gesetz und Lichtquantenhypothese. *Zeitschrift fur Physik*, 26:178–181, 1924.

[3] E. Cornell and C. Wieman. *Bose-Einstein Condensation in a Dilute Gas; The First 70 Years and Some Recent Experiment*. Nobel Lecture, 2002.

[4] E. P. Gross. Structure of a quantized vortex in boson systems. *Il Nuovo Cimento*, 20:454–477, 1961.

[5] L. P. Pitaevskii. Vortex lines in an imperfect Bose gas. *Journal of Experimental And Theoretical Physics*, 13:451–454, 1961.

[6] L. Pitaevskii and S. Stringari. *Bose-Einstein Condensation*. Oxford University Press, 2003.

[7] N. Efremidis and D. Christodoulides. Lattice solitons in Bose-Einstein condensates. *Physical Review A*, 67:063608, 2003.

[8] R. Franzosi, R. Livi, G.-L. Oppo, and A. Politi. Discrete breathers in Bose-Einstein condensates. *Nonlinearity*, 24:R89–R122, 2011.

[9] F. Lederer, G. Stegeman, D Christodoulides, G. Assanto, M. Segev, and Y. Silberberg. Discrete solitons in optics. *Physics Reports*, 463:1–126, 2008.

[10] M. Peyrard, S. Cuesta-Lopez, and G. James. Nonlinear analysis of the dynamics of DNA breathing. *Journal of Biological Physics*, 35:73–89, 2009.

[11] M.I. Fakhretdinov and F.K. Zakir'yanov. Discrete breathers in the Peyrard-Bishop model of DNA. *Technical Physics*, 58-7:931–935, 2013.

[12] F. Piazza and Y.H. Sanejouand. Discrete breathers in protein structures. *Physical Biology*, 5:026001, 2008.

[13] M. Ibanes, J.M. Sancho, and G.P. Tsironis. Dynamical properties of discrete breathers in curved chains with first and second neighbor interactions. *Physical Review E*, 65:041902, 2002.

[14] S. Dmitriev, A. Chetverikov, and M. Velarde. Discrete breathers in 2d and 3d crystals. *Phys. Status Solidi B*, 252:1682–1686, 2015.

[15] A.V. Savin, E.A. Zubova, and L.I. Manevitch. Survival condition for low-frequency quasi-one-dimensional breathers in a two-dimensional strongly anisotropic crystal. *Physical Review B*, 71:224303, 2005.

[16] S. Iubini, O. Boada, Y. Omar, and F. Piazza. Transport of quantum excitations coupled to spatially extended nonlinear many-body systems. *New Journal of Physics*, 17:113030, 2015.

[17] D. Mogilevtsev, G. Ya Slepyan, E. Garusov, S. Ya Kilin, and N. Korolkova. Quantum tight-binding chains with dissipative coupling. *New Journal of Physics*, 17:043065, 2015.

[18] A. Nahum, J. Ruhman, and D. Huse. Dynamics of entanglement and transport in one-dimensional systems with quenched randmness. *Physical Review B*, 98:035118, 2018.

[19] N. Murray, M. Krygier, M. Edwards, K. Wright, G. Campbell, and C. Clark. Probing the circulation of ring-shaped Bose-Einstein condensates. *Phys. Rev. A*, 88:053615, 2013.

[20] K. Strecker, G. Partridge, A. Truscott, and R. Hulet. Formation and propagation of matter-wave soliton trains. *Nature*, 417:150–153, 2002.

[21] C. Chin, R. Grimm, P. Tiesinga, and E. Tiesinga. Feshbach resonances in ultracold gases. *Rev. of Modern Physics*, 82:1225, 2010.

[22] A.J. Moerdijk, H.M.J.M. Boesten, and B.J. Verhaar. Decay of trapped utracold alkali atoms by recombination. *Physical Review A*, 53-2:916–920, 1996.

[23] C.C. Bradley, C.A. Sackett, J.J. Tollett, and R.G. Hulet. Evidence of Bose-Einstein condensation in an atomic gas with attractive interactions. *Physical Review Letters*, 75-9:1687, 1995.

[24] M.D. Barrett, J.A. Sauer, and M.S. Chapman. All-optical formation of an atomic Bose-Einstein condensate. *Physical Review Letters*, 81-1:010404, 2001.

[25] L. Salsnich, A. Parola, and L. Reatto. Effective wave equations for the dynamics of a cigar-shaped and disk-shaped Bose condensates. *Phys. Rev. A*, 65:043614, 2002.

[26] C. Kittel, editor. *Introduction to solid state physics (7th Edition)*. Wiley, New York, 1996.

[27] R. Livi, R. Franzosi, and G.-L. Oppo. Self-localization of Bose-Einstein condensates in optical lattices via boundary dissipation. *Physical Review Letters*, 97:060401, 2006.

[28] H. Yoshida. Construction of higher order symplectic integrators. *Physical Review A*, 5-7:262–268, 1990.

[29] J. Cuevas, G. James, P. Kevrekidis, B. Malomed, and B. Sancez-Rey. Approximation of solitons in the discrete NLS equation. *Journal of Nonlinear Mathematical Physics*, 15-3:124–136, 2013.

[30] S. Takeno, K. Kisoda, and A. J. Sievers. Intrinsic localized vibrational modes in anharmonic crystals: Stationary modes. *Progress of Theoretical Physics Supplement*, 94:242–269, 1988.

[31] J. B. Page. Asymptotic solutions for localized vibrational modes in strongly anharmonic periodic systems. *Physical Review B*, 41:7835, 1990.

[32] J.P. Eckmann and C.E. Wayne. Breathers as metastable states for the discrete NLS equation. *arXiv preprint*, arXiv:1710.10999, 2017.

[33] S. Darmanyan and A. Kobyakov. Stability of strongly localized excitations in discrete media with cubic nonlinearity. *Journal of Experimental and Theoretical Physics*, 86-4:682, 1998.

[34] B. Rumpf. Transition behavior of the discrete nonlinear Schrödinger equation. *Physical Review E*, 77:063306, 2008.

[35] M. Johansson and S. Aubry. Growth and decay of discrete nonlinear Schrödinger breathers interacting with internal modes or standing-wave phonons. *Physical Review E*, 61-5:5864, 2000.

[36] M. Johansson. Decay of discrete nonlinear Schrödinger breathers through inelastic multiphoton scattering. *Physical Review E*, 63:037601, 2001.

[37] M. Johansson and S. Aubry. Existence and stability of quasiperiodic breathers in the discrete nonlinear Schrödinger equation. *Nonlinearity*, 10:1151, 1997.

[38] B. Rumpf. Intermittent movement of localized excitations of a nonlinear lattice. *Physical Review E*, 70:016609, 2004.

[39] B. Rumpf. Growth and erosion of a discrete breather interacting with Rayleigh-Jeans distributed phonons. *EPL*, 78:26001, 2007.

[40] H. Hennig, J. Dorignac, and D. K. Campbell. Transfer of Bose-Einstein condensates through discrete breathers in an optical lattice. *Physical Review A*, 82:053604, 2010.

[41] P. Jason and M. Johansson. Charge flipping vortices in the discrete nonlinear schrondinger trimer and hexamer. *Physical Review E*, 91:022910, 2015.

[42] S. Flach and V. Fleurov. Tunnelling in the noninegrable trimer - a step towards quantum breathers. *Journal of Physics: Condensed Matter*, 9:7039–7061, 1997.

[43] M.I. Molina and G.P. Tsironis. Dynamics of self-trapping in the discrete nonlinear Schrödinger equation. *Physics D*, 65:267–273, 1993.

[44] V.M. Kenkre and D.K. Campbell. Self-trapping on a dimer: Time-dependent solutions of a discrete nonlinear Schrödinger equation. *Physical Review B*, 34:4959, 1986.

[45] E. Weinan, B. Engquist, and Z. Huang. Heterogeneous multiscale method: A general methodology for multiscale modeling. *Physical Review B*, 67:092101, 2003.

[46] G. Ariel, B. Engquist, and R. Tsai. A reversible multiscale integration method. *Communications in Mathematical Sciences*, 7-3:595–310, 2009.

[47] R. Franzosi. Microcanonical entropy and dynamical measure of temperature for systems with two first integrals. *Journal of Statistical Physics*, 143:824–830, 2011.

[48] K. Rasmussen, T. Cretegny, P.G. Kevrekidis, and N. Grobech-Jenses. Statistical mechanics of a discrete nonlinear system. *Physical Review Letters*, 84:3740, 2000.

[49] S. Iubini, R. Franzosi, R. Livi, G.-L. Oppo, and A. Politi. Discrete breathers and negative-temperature states. *New Journal of Physics*, 15:023032, 2013.

[50] S. Iubini, S. Lepri, R. Livi, and A. Politi. Off-equilibrium Langevin dynamics of the discrete nonlinear Schrödinger chain. *Journal of Statistical Mechanics: Theory and Experiment*, page 08017, 2013.

[51] S. Iubini, S. Lepri, and A. Politi. Nonequilibrium discrete nonlinear Schrödinger equation. *Physical Review E*, 86:011108, 2012.

[52] B. Derrida. Non-equilibrium steady states: fluctuations and large deviations of the density and of the current. *Journal of Statistical Mechanics*, page 07023, 2009.

[53] S. Iubini, S. Lepri, R. Livi, G.-L. Oppo, and A. Politi. A chain, a bath, a sink, and a wall. *Entropy*, 19:445, 2017.

[54] T. Mithun, Y. Kati, C. Danieli, and S. Flach. Weakly nonergodic dynamics in the Gross-Pitaevskii lattice. *Physical Review Letters*, 120:184101, 2018.

[55] J. Schachenmayer, A. Pikovski, and A.M. Rey. Many-body quantum spin dynamics with Monte Carlo trajectories on a discrete phase space. *Physical Review X*, 5:011022, 2015.

[56] A.M. Morgante, M. Johansson, S. Aubry, and G. Kopidakis. Breather-phonon resonances in finite-size lattices: phantom breathers? *Journal of Physics A: Mathematical and General*, 35:4999–5021, 2002.

[57] R. Franzosi, R. Livi, and G.-L. Oppo. Probing the dynamics of Bose-Einstein condensates via boundary dissipation. *Journal of Physics B*, 40:1195–1210, 2007.

[58] P.J. Message. The stability of our solar system. *Celestial mechanics*, 34:155–163, 1984.

[59] R. Johnson. *Singular Perturbation Theory*. Springer Science, 2005.

[60] A.I. Neishtadt and A.A. Vasiliev. Phase change between separatrix crossing in slow-fast Hamiltonian systems. *Nonlinearity*, 18:1393, 2005.

[61] A.I. Neishtadt and A.A. Vasiliev. Destruction of adiabatic invariances at resonances in slow-fast Hamiltonian systems. *Nuclear Instruments and Methods in Physics Research A*, 561:158–165, 2006.

[62] E. Weinan, B. Engquist, L. Xiantao, R. Weiqing, and E. Vanden-Eijnden. Heterogeneous multiscale mehods: A review. *Communications in Computational Physics*, 2:367–450, 2007.

[63] B. Engquist, P. Lötstedt, and O. Runborg. *Multiscale Modeling and Simulation in Science*. Springer Science, 2009.

[64] E. Weinan. *Principles of Multiscale Modelling*. Cambridge University Press, 2011.

[65] S. Flach and A.V. Gorbach. Discrete breathers – advances in theory and applications. *Physics Reports*, 467:1–116, 2008.

[66] J. Kruse and R. Fleischmann. Self-localization of Bose-Einstein condensates in optical lattices. *Journal of Physics B: Atomic, Molecular and Optical Physics*, 50:055002, 2017.

[67] A. Smerzi, S. Fantoni, S. Giovanazzi, and S. R. Shenoy. Quantum coherent atomic tunneling between two trapped Bose-Einstein condensates. *Physical Review Letters*, 79:4950, 1997.

[68] H. Hennig, T. Neff, and R. Fleischmann. Dynamical phase diagram of Gaussian wave packets in optical lattices. *Physical Review E*, 93:032219, 2016.

[69] S. Iubini, L. Chirondojan, G.-L. Oppo, A. Politi, and P. Politi. Dynamical freezing of relaxation to equilibrium. *Physical Review Letters*, 122:084102, 2019.

[70] T. Mithun, Y Kati, C. Danieli, and S. Flach. Weakly nonergodic dynamics in the Gross-Pitaevskii lattice. *Physical Review Letters*, 120:148101, 2018.

[71] Y. Capdeville and J. Marigo. A non-periodic two scale asymptotic method to take account of rough topographies for 2-d elastic wave propagation. *Geophysics Journal International*, 192:163–189, 2013.

[72] D. Hennig, H. Gabriel, M. F. Jørgensen, P. L. Christiansen, and C. B. Clausen. Homoclinic chaos in the discrete self-trapping trimer. *Physical Review E*, 51:2870, 1995.

[73] K. Nemoto, C. A. Holmes, G. J. Milburn, and W. J. Munro. Quantum dynamics of three coupled atomic Bose-Einstein condensates. *Physical Review A*, 63:013604, 2000.

[74] R. Franzosi and V. Penna. Chaotic behavior, collective modes, and self-trapping in the dynamics of three coupled Bose-Einstein condensates. *Physical Review E*, 67:046227, 2003.

[75] P. Jason, M. Johansson, and K. Kirr. Quantum signatures of an oscillatory instability in the Bose-Hubbard trimer. *Physical Review E*, 86:016214, 2012.

[76] A. H. Nayfeh. *Perturbation Methods*. Wiley Vch, Weinheim, 2004.

[77] L. Chirondojan and G.-L. Oppo. Multiple-time-scale analysis for pinned breathers in Bose-Hubbard chains. *Physical Review E*, 99:022212, 2019.

[78] M. Levi. Adiabatic invariants of the linear Hamiltonian systems with periodic coefficients. *Journal of Differential Equations*, 42:47–71, 1981.

[79] M.P. Calvo, P. Chartier, A. Murua, and J.M. Sanz-Serna. A stroboscopic numerical method for highly oscillatory problems. *Engquist B., Runborg O., Tsai YH. (eds) Numerical Analysis of Multiscale Computations. Lecture Notes in Computational Science and Engineering*, 87:71–87, 2012.

[80] O. Lloberas-Valls, D. J. Rixen, A. Simone, and L. J. Sluys. On micro-to-macro connections in domain decomposition multiscale methods. *Computer methods in applied mechanics and engineering*, 225-228:177–196, 2012.